Hydrodynamics and Thermodynamics of Ice Particle Accretion

Vom Fachbereich Maschinenbau
an der Technischen Universität Darmstadt
zur
Erlangung des Grades eines Doktor-Ingenieurs (Dr.-Ing.)
genehmigte

D i s s e r t a t i o n

vorgelegt von

Daniel Martin Kintea, M.Sc.

aus Groß-Umstadt

Berichterstatter:	Prof. Dr.-Ing. C. Tropea
Mitberichterstatter:	Prof. Dr.-Ing. P. Stephan
	PD Dr.-habil. I. Roisman
Tag der Einreichung:	25.01.2016
Tag der mündlichen Prüfung:	27.04.2016

Darmstadt 2016
D17 (Diss. Darmstadt)

Dedicated to the memory of Anton Kintea. By inspiration and with commitment, he has brought me on the way eventually leading to this work. You were the best father one could ever wish for.

I wish I could have told you.

Abstract

Icing in warm environments, e.g. in aircraft engines or heated measurement probes, occurs if airplanes fly through areas with high amounts of atmospheric ice crystals. Ingested into the warm engine, they start to melt, resulting in an airflow laden with mixed-phase particles consisting of water and ice. Liquid water deposits on component surfaces, which enables ice particles to adhere to them, forming ice accretion of considerable thickness. Such an accretion reduces reliability, power and efficiency of the engine and impedes the function of probes. While light icing reduces the aircraft's economic viability and environmental-friendliness by increasing fuel consumption, it may lead to engine failure and damage as well as probe malfunction in severe cases, which threatens aircraft safety significantly. The aviation industry is highly interested in eliminating this problem and in developing accurate ice accretion models. As the comprehension of the underlying physics is still rudimentary, the accuracy of current prediction tools is rather limited. The goal of this work is to investigate the physical mechanisms leading to ice accretion by developing theoretical models and the implementation of them in numerical codes.

Within the scope of this work, three main phenomena related to the process of ice crystal accretion are studied: the melting of non-spherical particles, the impact of small particles on a liquid surface and the accretion and shedding of ice layers.

In order to investigate the particle melting, a theoretical model is developed based on an approximation of the particle shape as a spheroid. Due to capillary forces, the arising meltwater is presumed to accumulate in the particle mid-section, where the curvature is minimal. Numerically realized with a Level-Set approach, the model is able to predict the evolution of the shape of the melting particle and the time of its melting with high accuracy. It yields results which confirm the model's superiority over currently employed melting models.

The particle impact onto a liquid surface is studied numerically. In

addition to pressure and viscous forces acting on the particle, capillary forces arising in the three phase contact line are taken into account by the Finite-Volume algorithm. An appropriate mesh motion allows for the movement of the particle which constitutes a boundary on the domain while the liquid-gaseous interface is accounted for by a Volume-of-Fluid method. The code accurately predicts the impact behavior of high Weber number processes as well as of low Weber impacts in which surface tension and the contact line force resulting from it prevails. By means of data obtained with the algorithm and a dimensional analysis, a simple correlation is found which is able to predict whether particles stick or rebound.

Investigation of the behavior of accreted ice layers is carried out using two approaches. In the first approach, a detailed three-dimensional thermal model which resolves ice particles and liquid droplets is developed. It demonstrates that a porous ice/water layer behaves differently than solid ice. Theoretical modeling of the effective thermal properties and accounting for the transport of heat and mass in the ice layer is the basis of the second approach. It yields a numerical algorithm which efficiently predicts the composition of the accretion, which is then utilized to anticipate the instant of ice plate shedding. The obtained results agree very well with experimental data.

Kurzfassung

Vereisung in warmen Umgebungen, bspw. in Flugtriebwerken oder beheizten Messsonden, tritt auf, wenn Flugzeuge durch Gebiete mit hoher Konzentration von atmosphärischen Eiskristallen fliegen. Beim Eintreten in das warme Triebwerk beginnen diese zu schmelzen; es entsteht eine Luftströmung beladen mit Wasser und Eispartikeln. Das flüssige Wasser sammelt sich auf Bauteiloberflächen und erlaubt es den Eispartikeln, an diesen anzuhaften. Dieser Prozess führt zur Bildung von Eisschichten signifikanter Dicke. Solche Partikelansammlungen reduzieren die Zuverlässigkeit, Leistung und Effizienz des Triebwerks und behindern die Funktion von Messsonden. Während leichte Vereisung die Wirtschaftlichkeit und Umweltfreundlichkeit durch Erhöhung des Brennstoffverbrauchs reduziert, führt schwere Vereisung zum Triebwerksausfall und -beschädigung und zum Versagen von Sonden, was die Flugsicherheit signifikant beeinträchtigt. Daher ist die Luftfahrtindustrie sehr daran interessiert, dieses Problem zu eliminieren und präzise Modelle für die Vereisung zu entwickeln. Da das Verständnis der zu Grunde liegenden Physik nur rudimentär ist, ist die Genauigkeit heutiger Vorhersagen durch theoretische Modelle oder Simulationen stark beschränkt. Ziel dieser Arbeit ist die Untersuchung der physikalischen Mechanismen, die zur Vereisung führen durch die Entwicklung theoretischer Modelle und deren Implementierung in numerische Algorithmen.

Drei wesentliche Phänomene, die zur Bildung von Eispartikelansammlungen führen, sind im Rahmen dieser Arbeit untersucht worden: das Schmelzen nicht-kugelförmiger Partikel, der Aufprall von kleinen Partikeln auf eine Flüssigkeitsoberfläche und das Verhalten von Eiskristallansammlungen und deren Abbrechen von Oberflächen.

Zur Untersuchung des Partikelschmelzens erfolgt eine theoretische Modellierung des Vorgangs, beruhend auf der Annahme, dass das Partikel vor Beginn des Schmelzvorgangs eine rotationsellipsoide Form hat. Aufgrund von kapillarem Druck sammelt sich das entstehende Schmelzwasser in der Mitte des Partikels, wo dessen

Oberflächenkrümmung minimal ist. Der mittels Level-Set Methode umgesetzte Algorithmus ist in der Lage die Entwicklung der Form des schmelzenden Partikels und die Dauer des Schmelzvorgangs mit großer Genauigkeit vorherzusagen. Es liefert Ergebnisse, die die Überlegenheit des Modells gegenüber heutigen Schmelzmodellen demonstrieren.

Die Untersuchung des Aufpralls eines Partikels auf eine flüssige Oberfläche erfolgt numerisch. Zusätzlich zu den viskosen- und Druckkräften die auf das Partikel wirken, wird die kapillare Kraft, die in der Dreiphasenkontaktlinie entsteht, von dem Finite-Volumen Algorithmus berücksichtigt. Eine geeignete Gitterbewegung erlaubt die Bewegung des Partikels, dessen Oberfläche eine Berandung der Domäne darstellt. Die Grenzfläche zwischen flüssiger und gasförmiger Phase ist mit Hilfe einer Volume-of-Fluid Methode berücksichtigt. Der Code liefert eine präzise Vorhersage des Aufprallvorgangs bei hohen Weberzahlen sowie bei niedrigen, bei denen die Oberflächenspannung und die Kontaktlinienkraft, die daraus resultiert, dominieren. Anhand der gesammelten Daten und einer Dimensionsanalyse wurde eine einfache Korrelation gefunden, mit der es möglich ist vorherzusagen ob ein Partikel anhaftet oder abprallt.

Die Analyse des Eisschichtverhaltens erfolgt anhand zweier Vorgehensweisen. Eine Entwicklung eines detaillierten, dreidimensionalen, thermischen Modells, in dem die Eispartikel und Flüssigkeitstropfen numerisch aufgelöst sind, stellt die erste Herangehensweise dar. Es zeigt, dass eine poröse Eis-Wasser-Schicht sich deutlich verschieden von einer massiven Eisschicht verhält. Theoretisches Modellieren des effektiven thermischen Verhaltens und die Berücksichtigung von Transportprozessen von Wärme und Stoff in der Eisschicht stellt die Grundlage der zweiten Vorgehensweise dar. Es liefert einen numerischen Algorithmus, der die Zusammensetzung der Schicht und damit deren Ablösung effizient beschreibt. Die erzielten Ergebnisse stimmen sehr gut mit experimentellen Beobachtungen überein.

Acknowledgements

During my PhD candidature I had the pleasure to be supported by numerous friends, colleagues, students and my family. At this point I would like to thank these people for making this work possible.

At first, I would like to express my greatest gratitude to PD Dr. habil. **Ilia V. Roisman** for his outstanding supervision and excellent support during this work, both on a professional level as well as personally. With his ingenuity, none of the problems I ran into during my research seemed unsolvable. Technical discussions were not just fruitful, but inspiring. Ilia, I really enjoyed working under your supervision and tried to absorb as much of your knowledge as possible. Stay just as you are!

I would like to thank the head of the Institute for Fluid Mechanics and Aerodynamics of the Technische Universität Darmstadt, Prof. Dr. **Cameron Tropea**. He gave me the chance to be part of the international research project HAIC, to write this thesis and to gain professional experience on conferences and meetings all over the world. It was a great time working at a well-organized institute together with highly talented people. Thank you for giving me this exceptional opportunity!

It was a great honor being part of the European research project HAIC, meeting and working together with people from all over the continent. For the great collaboration and the fact that I was always looking forward to the regular meetings we had, I would like to thank **every HAIC member**, which are just too many to list them at this point.

For the outstanding and fruitful collaboration I want to thank **Tobias Hauk** working as a doctoral student at Airbus Group Innovations. I really enjoyed working together with you and the time we shared on several business trips!

A considerable part of the work leading to the results presented in this thesis has been carried out by several students as research assistants or in the scope of their Bachelor or Master thesis. In particular the projects of **Jens-Michael Löwe**, **Dario Klingenberg**, **Markus Schremb**, **Jan Breitenbach** and **Maximilian von der Grün** were of such high quality

that parts of their work are already published or constitute significant content of this thesis. For this support I am extremely grateful. Thank you!

For many fruitful discussions, help on various topics and making the working hours most enjoyable I would like to thank my colleagues and friends at the institute. My particular thanks go to **Vignesh Thammanna Gurumurthy**, **Markus Schremb**, **Rüdiger Röhrig**, **Jan Breitenbach**, **Lars Opfer** and **Herr Marschall**.

Last, but not least, I would like to thank my family for supporting me during the candidature. In particular I want to thank my mother **Monika Kintea** and my girlfriend **Hanna Faust** for patiently accompanying every step and having to listen to me complaining about non-converging computer simulations which they certainly were highly interested in. I love the both of you.

In all formality, I want to thank the European tax payer: This project has received funding from the European Union's Seventh Framework Programme for research, technological development and demonstration under grant agreement n°ACP2-GA-2012-314314.

Nomenclature

Latin letters, upper case

Symbol	SI-Unit	Description
A	m^2	Area
AOA	-	Angle of attack
Bi	-	Biot number
Bo	-	Bond number
C	-	Drag and lift coefficient
Ca	-	Capillary number
D	$\mathrm{m}^2\,\mathrm{s}^{-1}$	Diffusivity
E	-	Aspect ratio
$\vec{F}$	$\mathrm{kg\,m\,s}^{-2}$	Force
G	-	Geometry parameter
H	m	Thickness
IWC	$\mathrm{kg\,m}^{-3}$	Ice water content
K	-	Shedding criterion
L	$\mathrm{m}^2\,\mathrm{s}^{-2}$	Latent heat of phase change
Le	-	Lewis number
LWC	$\mathrm{kg\,m}^{-3}$	Liquid water content
M	$\mathrm{kg\,kmol}^{-1}$	Molar mass
Ma	-	Mach number
Nu	-	Nusselt number
P	-	Probability
Pr	-	Prandtl number
R	$\mathrm{m}^2\,\mathrm{s}^{-2}\,\mathrm{K}^{-1}$	Gas constant
Re	-	Reynolds number
S	* $\mathrm{kg\ s}^{-1}\,\mathrm{m}^{-3}$	Source
Sc	-	Schmidt number
Sh	-	Sherwood number
St	-	Stefan number

* is a placeholder for an arbitrary unit, depending on the context.

T	K	Temperature
TWC	$\mathrm{kg\,m^{-3}}$	Total water content
$\vec{U}$	$\mathrm{m\,s^{-1}}$	Particle velocity
V	$\mathrm{m^3}$	Volume
We	-	Weber number

Latin Letters, lower case

Symbol	SI-Unit	Description
a	$\mathrm{m^2\,s^{-1}}$	Moisture transfer coefficient
$\vec{a}$	-	Unit axis of rotation
$\vec{b}$	-	Unit vector (normal to CL, tangential to wall)
c_p	$\mathrm{m^2\,s^{-2}\,K^{-1}}$	Specific heat at constant pressure
d	m	Diameter
$\vec{f}$	$\mathrm{m\,s^{-2}}$	Force per mass
$\vec{g}$	$\mathrm{m\,s^{-2}}$	Gravitational acceleration
h	$\mathrm{m^2\,s^{-2}}$	Specific enthalpy
j	$\mathrm{kg\,m^{-2}\,s^{-1}}$	Specific mass flux
k	$\mathrm{kg\,m\,s^{-3}\,K^{-1}}$	Thermal conductivity
l	m	Length
m	kg	Mass
n	-	Counting variable
$\vec{n}$	-	Unit normal vector
p	$\mathrm{kg\,m^{-1}\,s^{-2}}$	Pressure
$\dot{q}$	$\mathrm{kg\,s^{-3}}$	Heat flux density
r	m	Radius
s	m	Distance
t	s	Time
$\vec{u}$	$\mathrm{m\,s^{-1}}$	Fluid velocity
$\vec{v}$	$\mathrm{m\,s^{-1}}$	Velocity of solids
$\vec{x}$	m	Position
y^+	-	Dimensionless wall distance

Greek letters, upper case

Symbol	SI-Unit	Description
Γ_H	$\mathrm{kg\,s^{-3}\,K^{-1}}$	Heat transfer coefficient
Γ_M	$\mathrm{m\,s^{-1}}$	Mass transfer coefficient
Θ	-	Interpolation factor
Λ	-	Volumetric water content
Ξ	-	Impact angle
Φ	*	Arbitrary scalar
Ω	$\mathrm{kg\,m^2}$	Mass moment of inertia

Greek letters, lower case

Symbol	SI-Unit	Description
α	-	Volume fraction
β	*	Arbitrary property
γ	-	Collection efficiency
ϵ	-	Unit vector in direction of interface
ε	-	Porosity
ζ	-	Moisture content
η	-	Extinction function
θ	-	Contact angle
ϑ	$^\circ\mathrm{C}$	Temperature, Celsius scale
κ	$\mathrm{m^{-1}}$	Curvature
λ	$\mathrm{m^3}$	Cumulative volume
μ	$\mathrm{kg\,m^{-1}\,s^{-1}}$	Dynamic viscosity
ν	$\mathrm{m^2\,s^{-1}}$	Kinematic viscosity
$\tilde{\nu}$	$\mathrm{m^2\,s^{-1}}$	Working variable of turbulence model
ξ	-	Enhancement factor
ρ	$\mathrm{kg\,m^{-3}}$	Density
σ	$\mathrm{kg\,s^{-2}}$	Surface tension
$\vec{\tau}$	$\mathrm{kg\,m^2\,s^{-2}}$	Torque
ϕ	*	Constant
φ	-	Relative humidity
χ	$\mathrm{kmol\,m^{-3}}$	Molar concentration
ψ	m	Level-Set function
ω	$\mathrm{s^{-1}}$	Angular velocity

Subscripts

Subscript	Description
0	Initial
1D	One-dimensional
A	Air/Area
adv	Advancing
BL	Boundary layer
c	Capillary
C	Convection
ch	Chord
Cond	Conduction
conv	Converging
D	Drag
DNS	Detailed numerical simulation
div	Diverging
dyn	Dynamic
e/E	Eastern face/cell
ev	Evaporation
eq	Volume equivalent
expt	Experimental
f	Face/film/reference
g	Gaseous
H2O	Water molecule
i	Placeholder/imbibition
I	Ice
in	Input
inl	Inlet
l	Liquid
L	Lift
lam	laminar
m	Melting
max	Maximum
mc	Melting complete
mo	Melting onset
mod	Model
n/N	Northern face/cell
oc	Occupied
P	Particle/Considered cell

proj	Projected
R	Rotational
rec	Receding
rel	Relative
s/S	Southern face/cell
s	Solid
sat	Saturation
Sp	Sphere
st	Static
sub	Substrate
t	total
T	Translational/Thickness
turb	Turbulent
w/W	Western face/cell
w	Wall
W	Water
wb	Wet-bulb
∞	Ambient
σ	Surface tension
λ	Decay

Abbreviations

Abbreviation	**Description**
1D	One-dimensional
2D	Two-dimensional
3D	Three-dimensional
CDS	Central differencing scheme
CFD	Computational Fluid Dynamics
CL	Contact line
CO_2	Carbon dioxide
Comp.	Computation
DNS	Detailed numerical simulation
Expt.	Experimental
FDM	Finite-Difference method
FEM	Finite-Element method
FVM	Finite-Volume method
HAIC	High Altitude Ice Crystals

PA	Polyamide
PP	Polypropylene
PTFE	Polytetrafluoroethylene
RTD	Resistance temperature detector
SI	Système international d'unités
UDS	Upwind differencing schemes
VOF	Volume-of-Fluid

Contents

1 Introduction

Ice accretion on the surface of arbitrary objects leads to a change of the outer shape of the object, increasing weight, an alteration of its surface properties, a modified aerodynamic behavior and the shielding of the object's surface. These changes can influence the functionality of components exposed to icing conditions significantly. Probably the best known problem related to ice accretion is the icing of automotive wind-shields (Brewster et al., 1997) which hinders the driver's perception of his environment making de-icing necessary before driving. Ice accretion on solar panels or satellite dishes and antennae (Fillion et al., 2014) shield their surfaces from incoming sunrays or electromagnetic radiation, impeding their functionality until they eventually malfunction. Iced airfoils of wind turbines (Jasinski et al., 1998, Parent and Ilinca, 2011) or aircraft wings (Gent et al., 2000) change their shape and surface roughness leading to increased drag and reduced lift. As a result, the power output of wind turbines is reduced up to 20 % and the efficiency and safety of airplanes is decreased, leading to crashes in severe cases of icing. The additional mass due to ice accumulation on overhead power lines (Laforte et al., 1998) can cause them or the supporting pylons to collapse while icing of ships provokes imbalances ultimately sinking them (Zakrzewski, 1987). Ice accumulation in-between the fins of heat exchangers (Yan et al., 2003, Yao et al., 2004), in particular of heat pumps as employed in electric cars, shields them from the airflow, which reduces their efficiency. Transportation safety is lowered by ice on roads and bridges (Ferrara and Yenetchi, 1975) by altering the roadway's surface properties in terms of grip and wear and tear of the road, causing numerous accidents every winter. Reduced aircraft engine power due to compressor icing and icing of heated measurement probes (Mason et al., 2006, 2011) prove that the problem is not exclusively associated with cold environments but also occurs on warm components. The engine's power, efficiency and reliability are significantly reduced in icing conditions. Moreover, shedding ice can damage the engine severely and extinguish the combustion, while iced probes malfunction which can also be the reason for serious accidents.

Thus, the phenomenon of ice accretion affects manifold aspects of numerous industries and various areas of life, not only during winter or in cold regions. It significantly influences the efficiency of power generation and transportation and therefore affects CO_2 emissions and economic viability. Moreover, numerous icing related accidents causing economic losses, injuries and fatalities were recorded, either on land, sea or in the air rendering icing an extremely serious problem. Many different physical mechanisms can lead to ice accretion: re-sublimation, impingement and freezing of liquid water which might be supercooled and accretion of solid ice particles. The present study focuses on the ice accretion in warm environments, which typically forms due to the accumulation of a mixture of solid ice and liquid water, e.g. in aircraft engines or on heated measurement probes.

1.1 Motivation

Accretion of ice in the compressor of aeronautical engines reduces the engine's power and efficiency and therefore its reliability by blocking the cross-section for the airflow and deteriorating the airfoils of the blades. This can lead to compressor stall and surge, potentially damaging the engine. Figure 1.1 shows ice accretion on the inlet guide vanes of the low pressure compressor, as observed by Oliver (2014) in an ALF502-R5 engine. In severe icing cases, the combustion is extinguished resulting in total loss of thrust; re-ignition is only possible after leaving the icing conditions or descending into warmer air layers. Shedding of accreted ice layers which impact on downstream blades increases wear and tear and can damage them severely. Figure 1.2 shows a compressor rotor blade which has been damaged by the impact of shed ice, making a shutdown of the engine necessary. Furthermore, engine rotors can become out of balance due to ice accumulation, resulting in strong vibrations. Compressor icing threatens the engine operation as well as its structural integrity. Thus, it is not only critical for the aircraft operation in terms of economics, but also with regard to safety.

Measurement probes, either inside of the engine or attached to the airframe, provide the engine control, auto-pilot and pilots with crucial operating data. This information is essential for the safe operation of an airplane as they influence the decisions made by the flight computers or the pilots. Icing of such sensors hinders the measurement until malfunction

and is therefore also a significant safety issue.

Figure 1.1: Ice accretion on the inlet guide vane of the low pressure compressor of an ALF502-R5 (Oliver, 2014).

Figure 1.2: Damaged compressor rotor blade due to impact of shed ice (Oliver, 2014).

In order to better evaluate potential dangers, improve the economic

viability of aircraft and to support the certification process of new airplanes, the aviation industry needs predictive tools for ice accretion. Reliable tools require a substantiated understanding of the underlying physical mechanisms which is currently lacking. In the past, ice particles have been considered as benign to aircraft icing because solid particles bounce off the cold airframe and do not accumulate. More recent investigations (Currie et al., 2012, 2013, MacLeod, 2007, Mason et al., 2006, 2011, Struk et al., 2011) have shown that such ice particles accrete on surfaces in environments with a temperature above the melting point. This is due to a partial melting of the ice crystals, resulting in the formation of a thin liquid film to which the particles adhere to. Such hot surfaces can be found in the engine or on heated probes.

Despite experimental studies, the current understanding of the underlying physics is still very poor and therefore the possibilities of predicting ice particle accretion in terms of analytical models or numerical tools are very restricted. Present algorithms for the computation of icing usually employ the Messinger model (Messinger, 1953) for the accretion, which is based on a heat and mass balance and was designed to compute the icing due to impinging supercooled droplets. This model does not account for solid particles, therefore its applicability to ice particle accretion is limited. Moreover, the model requires information about mass fluxes of accreting liquid water and ice. This is obtained by particle tracking and melting computations in which the particles usually are considered spherical. Since typical atmospheric ice crystals are highly non-spherical, this assumption yields imprecise particle impingement locations and melt ratios. The impact itself is usually accounted for by means of an empirically determined sticking efficiency. Since there are no clearly defined models for crystal accretion, this approach exhibits potential for improvements and constitutes the starting point of this work.

1.2 Phenomena related to ice crystal accretion

Icing in warm environments, i.e. either warm surrounding air or warm surfaces, is typically caused by ice crystals which accrete on the relevant component surfaces. Solid ice particles are only able to accrete if water is present, i.e. mixed-phase conditions prevail. Experimental studies (Currie et al., 2012, 2013, 2014, Struk et al., 2011) indicate that the ratio of the liquid water content LWC to the total water content TWC of the flow has a

great influence on the ice accretion severity. Currie et al. (2013) proposed a dependency of the relative icing severity on LWC/TWC as sketched schematically in Fig. 1.3. The ratio at which the icing is severest ranges from approximately 10 to 25 %. Too little water prohibits the sticking of solid particles to the surface, while the upper limit is a result of too few ice particles to cool the surface sufficiently, which are then quickly washed away by the liquid water. Therefore, the lower limit for LWC/TWC arises from the particle impact dynamics, while its upper limit is governed by the heat fluxes affecting the accretion and the substrate underneath it which also influences the shedding behavior of the ice.

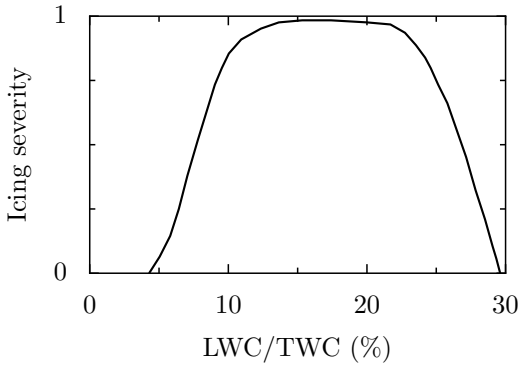

Figure 1.3: Icing limits according to Currie et al. (2013)

Engine icing events typically occur at cruise altitude, which is well above the theoretical limit for the presence of liquid water. Hence, the liquid water necessary for significant accretion arises by melting of the particles during their movement through the warm air within the engine or upon impact on hot surfaces. It deposits on the relevant surfaces in the form of droplets, rivulets and films. While solid particles bounce off dry surfaces, small particles are able to adhere to a liquid film. Melting of these particles cools the surface down until it reaches the melting point allowing ice particle accumulation. If the liquid at the surface freezes, mechanical interlocking between the ice and the surface roughness emerges, yielding a well-adhered connection of the accretion to the wall. Shedding of the ice occurs if the connecting ice at the accretion bottom is either broken or melted.

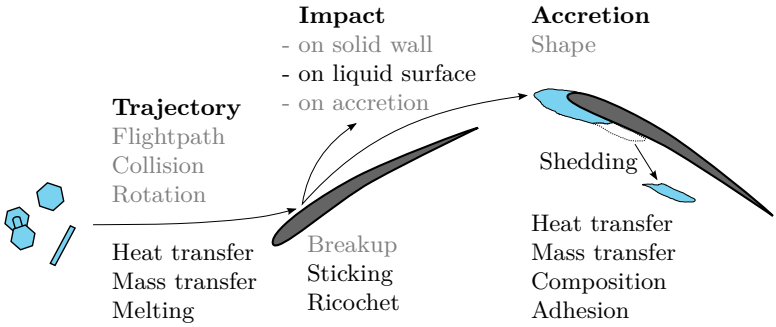

Figure 1.4: Physical mechanisms influencing ice particle accretion in an aero-engine. Processes addressed in this thesis are labeled in black.

Figure 1.4 gives an overview of the physical processes which typically are involved in the process of ice particle accretion in aircraft engines. Melting of the non-spherical particles on their trajectories determines the melt ratio of the impinging particles while their drag, rotation and particle collisions dictate the location of impact which might occur on a solid wall, a liquid surface or on the porous ice/water accretion. Upon impact, the particles can either stick to the surface, ricochet or a mixture of both after particle breakup. This impact behavior determines the local growth rate of the ice accretion of certain shape. Heat and mass transfer processes within the accretion and at its boundaries affect its composition and therefore its adhesion to the surface on which it accretes. If the adhesion is lost, shedding of ice layers occurs. Processes which are explicitly addressed in this work are labeled in black while other mechanisms are labeled in gray.

Three major aspects leading to ice particle accretion are considered in this thesis and are depicted in Fig. 1.5. These are, in chronological order when following an ice particle from ingestion to accretion and possibly shedding:

1. melting of the ingested irregular ice particles,
2. impact of solid particles on a liquid surface and
3. accretion and shedding of the ice layer.

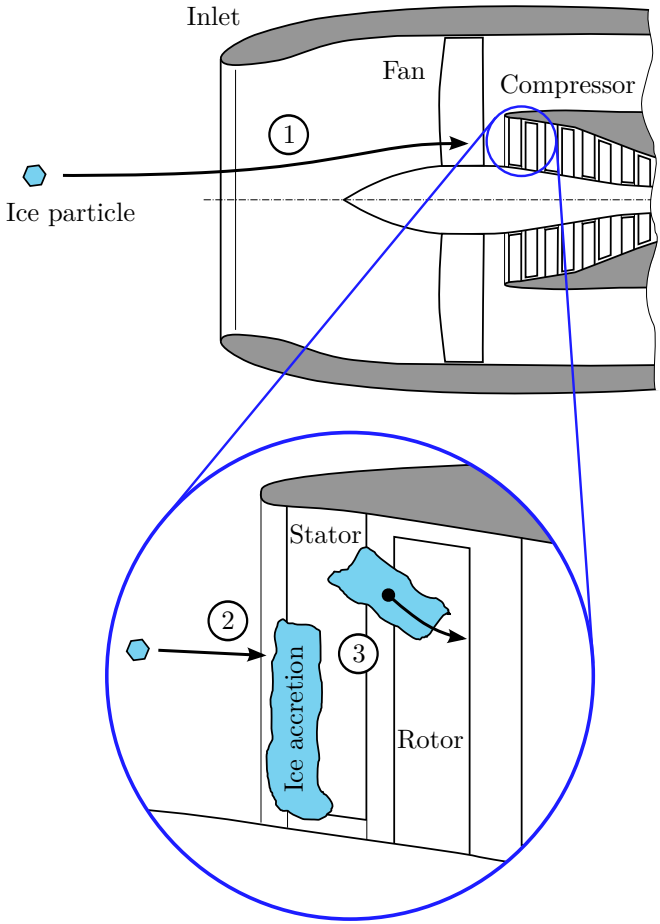

Figure 1.5: Sketch of the ice particle accretion process: (1) Melting of the ice crystal on its way through the engine, (2) particle impact and (3) accretion and shedding of the ice layer.

These three subprocesses are discussed in detail in the following and their state-of-the-art is presented. Moreover, they form the structure of this thesis: A theoretical model for the melting process of non-spherical

particles is presented and numerically realized in chapter 2. Chapter 3 is devoted to the particle impact on a liquid surface while chapter 4 and 5 correspond to the detailed numerical simulation and theoretical modeling of the accretion and shedding process.

1.2.1 Melting of ingested particles

This section, as well as chapter 2, is based on the paper *Shape evolution of a melting nonspherical particle* by Kintea et al. (2015b).

Phase change processes of solid particles have always been of fundamental interest. First investigations were based on the assumption that the particle is spherical which allows a one-dimensional consideration of the problem. Typical examples include the well-known Stefan and Neumann problems (Carslaw et al., 1959). One of the simplest cases of Stefan problem is melting of a solid sphere. Such one-dimensional problem includes a solution for the heat conduction in the solid and liquid regions of the sphere and matching using the Stefan condition at the solid-liquid boundary. For a sphere heated by an external gas flow also the thermal boundary conditions on the liquid surface have to be considered, which account for the convection in the outer gas region. Despite its "simplicity" this problem still does not have an exact analytical solution. The problem becomes especially complicated if the initial temperature of the solid particle is not uniform or even if it is not equal to the fusion temperature.

Among theoretical models, the problem of phase change of a sphere at various asymptotic conditions are models developed for small Stefan numbers (McCue et al., 2008, Pedroso and Domoto, 1973, Riley et al., 1974, Soward, 1980, Stewartson and Waechter, 1976, Tabakova et al., 2010), short time asymptotic solutions (Davis and Hill, 1982, Hill and Kucera, 1983, McCue et al., 2008), and remote asymptotic solutions for long times (Herrero and Velázquez, 1997, Soward, 1980). Results valid for general Stefan numbers are obtained numerically (McCue et al., 2008) and analytically (McCue et al., 2005).

Simplified models allowing a rough estimation of the typical melting times and rates of melting are also very useful for various engineering applications, mainly if the heat conduction in the solid particle and thermal transient effects are negligibly small (Kreith and Romie, 1955, London and Seban, 1943). A simplified one-dimensional model has been proposed by Mason (1956). Such a model, which assumes the melting

particle to be spherical and isothermal, is widely used (Konrad et al., 2007, Tseng and Viskanta, 2006, Wang et al., 2015b); also in applications involving the melting of non-spherical particles (Gan et al., 2003, Gu and Kamnis, 2009, Richter and Nikrityuk, 2013).

A description of a phase change, melting or condensation, at a surface of solid bodies of irregular shape is even a more challenging problem. This problem is associated with melting of clusters of particles (Berry et al., 1984), melting or condensation in porous media (Melrose, 1966, Molz et al., 1993), in suspensions (Larsen and Grier, 1996) or in granular media (Olafsen and Urbach, 2005, Pacheco-Vázquez et al., 2009, Turnbull, 2011), and melting of snow flakes (Fukuta et al., 1982, Mitra et al., 1990) or other dendritic structures (Oraltay and Hallett, 1989). Melting of solid particles is a key element in thermal spraying technology (He et al., 2001, Pawlowski, 2008) or in the production of spherical particles. This problem is also associated with phase-change materials for energy storage components (Dutil et al., 2011).

Melting of particles in the submicron size range has also attracted much interest, including studies on the dependence of the melting temperature on the particle size (Pawlow, 1909, Wang et al., 2010, Zhou and Sheng, 1991), or even on the size dispersity as presented by Watanabe et al. (2005). Melting of particles, in particular irregular particles (Attar et al., 2014), is an important element of the technology of selective laser sintering, which is a rapid prototyping technique for fabrication of components with complex geometries and from complex materials, for example sintered metallic parts (Kruth et al., 2004) or artificial bones (Williams et al., 2005).

Some experimental studies on particle melting have been undertaken in the past, for example investigations of snow flakes by Fukuta et al. (1982), Mitra et al. (1990) or other dendritic structures by Oraltay and Hallett (1989). Wind tunnel experiments are often used to investigate the melting of ice spheres (Rasmussen and Pruppacher, 1982, Rasmussen et al., 1984a,b) under conditions similar to real flight conditions.

Atmospheric ice crystals can adhere and accrete at the internal surfaces of jet engines or aircraft instrumentation, as shown by Mason et al. (2011), if they partially melt. Ice accretion reduces the engine's reliability, power and efficiency. Atmospheric ice crystals usually form due to condensation and desublimation, leading to various geometries such as needles, plates, prisms or dendrites (Furukawa and Wettlaufer, 2007, Heymsfield et al.,

2002). The melting behavior of such particles differs significantly from spherical ones resulting in different particle melt ratios determining the LWC/TWC of the flow. Since this ratio has a crucial influence on the icing severity as shown in Fig. 1.3, the melting process of irregular particles affects the icing considerably which explains the necessity for its further investigation and modeling performed in the scope of this work.

1.2.2 Impact of ice particles

This section is based on the introduction of the paper *On the influence of surface tension during the impact of particles on a liquid-gaseous interface* by Kintea et al. (2016a).

The process of water entry has attracted the attention of scientists and engineers for over a century and is still a field of current research. Particularly the loads acting on the impacted object are of special interest, for instance when designing naval projectiles or seaplanes. They govern the safety of dropped objects or airplanes during emergency landings on a water surface. Also, the behavior of ice crystals during their impingement onto liquid film covered surfaces determines whether they stick to the surface, shatter or ricochet. Therefore, the process of water entry also has a crucial influence on mixed phase ice accretion, e.g. in aircraft engines, as described by Mason et al. (2006) or Struk et al. (2011). Of particular interest for this process is the impingement of particles at low Weber numbers. Such impacts can also be found during the agglomeration of wetted particles during spray drying or multiphase combustion.

First investigations of the water entry phenomena date back to Worthington (1908), which is an experimental study of splashes. The first analytical considerations have been performed by von Kármán for the impact of a blunt wedge, followed by Shiffman and Spencer (1945), who focused on the analytical description of the impact of spheres. They found, that the water entry can be subdivided into three stages: the initial slamming stage, the motion through the water with a trailing cavity, and the sinking of the particle after the cavity collapses. The maximum force acting on the sphere occurs during the first stage, which begins when the object touches the free surface of the liquid and ends when the center of the sphere passes the initial free surface level. During the second stage, the sphere is followed by a cavity, whose behavior governs the drag of the sphere during this phase. This stage of water entry comes to an

end when the cavity collapses; the so-called pinch-off. The duration of the second stage depends on the impact velocity and material properties of the liquid and the impacting object. Under certain circumstances the duration of this phase becomes zero, i.e. no cavity emerges. This happens for low impact velocities or hydrophobic particle surfaces as observed and reported by Duez et al. (2007). The sinking of the sphere after the cavity collapses, which forms the third phase, is mainly governed by buoyancy and single phase drag.

A comprehensive review of the literature concerning water entry until 2004 has been carried out by Seddon and Moatamedi (2006). More recent research on the water entry of spherical particles has been performed for non-rotating (Aristoff and Bush, 2009, Aristoff et al., 2010, Truscott et al., 2012) and rotating spheres (Dupeux et al., 2010, Techet and Truscott, 2011, Truscott and Techet, 2009a,b) at high Weber numbers larger than 1000. A review which also covers these newer investigations has been performed by Truscott et al. (2014). Numerical approaches are only available for the non-spinning experiments by Aristoff et al. (2010), described by Mirzaii and Passandideh-Fard (2012) and Ahmadzadeh et al. (2014). Moreover, particles at low Weber numbers have been investigated by Lee and Kim (2008), Do-Quang and Amberg (2009) and Wang et al. (2015a). For the case of normal impact of a non-rotating sphere a theoretical model has been developed by Aristoff et al. (2010). This model is capable of predicting the particle trajectory until the cavity pinch-off with high accuracy.

The motion of a rotating particle is determined not only by a drag force, but also a lift force and a torque acting on the spherical body. Drag and lift force coefficients have been measured for rotating spheres in a stationary single phase flow (Barkla and Auchterlonie, 1971, Kray et al., 2012, Muto et al., 2012, Tsuji et al., 1985), to mention a few. It is doubtful that existing correlations for the drag and lift forces in a single phase flow are applicable to the description of multiphase situations, like water entry. Fig. 1.6 shows the trajectory of a billiard ball entering a liquid pool with the formation of a cavity; Fig. 1.7 shows the water entry without any cavity formation. The circles denote values, which were measured in the experiments by Techet and Truscott (2011). The solid lines correspond to computations based on the most applicable drag and lift coefficients for single phase flows as presented by Kray et al. (2012). The observed deviation is excessive, presumably due to the fact that the model does not account for effects related to the emergence of a cavity. Also, transient

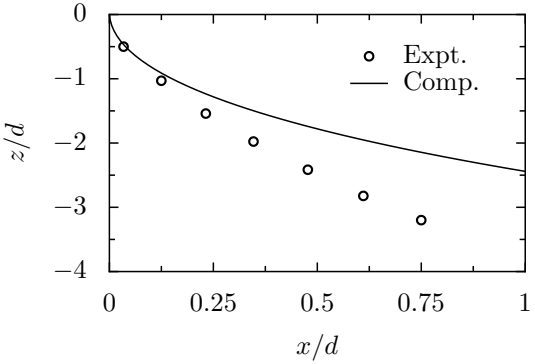

Figure 1.6: Comparison of experimental (Techet and Truscott, 2011) and computed trajectories of a rotating hydrophilic billiard ball entering a free liquid surface using measured drag coefficients in single phase flow (Kray et al., 2012), the distances are non-dimensionalized with the sphere diameter d. The sphere is followed by a cavity during the impact process.

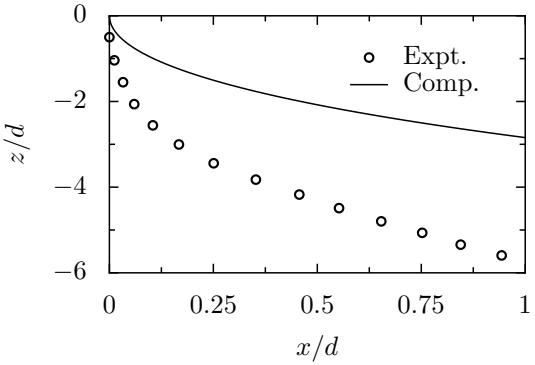

Figure 1.7: Comparison between results obtained by means of the single phase drag model and experimental data: Motion of a rotating hydrophilic sphere without cavity formation.

effects linked with the penetration of the liquid surface are not covered by these correlations.

When considering the impact of small particles the influence of the surface tension rises. Several experimental and analytical investigations (Aristoff and Bush, 2009, Lee and Kim, 2008, Vella and Metcalfe, 2007, Vella et al., 2006) concerning this topic were performed in the last decade. Yet, no simple models or correlations are available which describe the impact process of a small particle which could be employed to predict the sticking efficiency of ice crystals. A development of such a model constitutes one of the goals of this work.

1.2.3 Accretion of ice crystals

This section is based on the introduction of the article *Transport processes in a wet granular ice layer: model for ice accretion and shedding* by Kintea et al. (2016b).

An overview over ice crystal icing related incidents has been presented by Mason et al. (2006). Following up, many experimental investigations have been performed. An ice crystal capability has been implemented in a wind tunnel and the icing of a heated flat plate has been investigated by MacLeod (2007) while ice particle accretion on an airfoil in an S-duct has been looked at by Mason et al. (2011). Icing of a wedge shaped airfoil has been examined by Struk et al. (2011, 2015) and Currie et al. (2012), while the ice accretion on axisymmetric components has been analyzed by Currie et al. (2013, 2014) and Currie and Fuleki (2015). An overview of a facility with the capability of testing entire engines in icing conditions is presented by Griffin et al. (2014). Ice accretion on a NACA0012 and the leading edge heater power required for anti-icing has been investigated in mixed phase conditions by Al-Khalil et al. (2003), Miller et al. (1997).

Most of current models for the computation of ice particle accretion are based on the model presented by Messinger (1953), which was originally developed for icing due to the impact of liquid water. Its main assumption is that a continuous liquid film covers the surface of the solid ice layer, but neither its height nor its dynamics are computed directly. Moreover, it is a steady-state approach and neglects heat conduction. The foundation of the model is given by two balance equations, one for mass and one for energy.

Several improvements of the original model have been proposed, such as accounting for the dissipative heating (Cansdale and Gent, 1983, Ruff and Berkowitz), incorporation of additional heat fluxes, e.g. from anti-icing

systems (Thomas et al., 1996) or taking heat conduction (Bourgault et al., 2000) into account.

While in Messinger's original icing model the dynamics and thickness of the water film are not computed, so-called film models account for the behavior of the film as firstly proposed by Bourgault et al. (2000). In his model, the film is solely driven by shear forces while Myers (2001) also includes the effects of surface curvature, gravity and pressure forces. This approach has been further developed and presented by Myers and Charpin (2004), Myers et al. (2002a,b) and Brakel et al. (2007).

First extensions to the Messinger model in order to account for impinging ice particles were made by Wright et al. (2010), Habashi and Nilamdeen (2011), Ríos Pabón (2012) and Oliver (2013) by including ice crystals and their melting in the balance equations. The capability to compute ice crystal accretion has been implemented in a film model by Villedieu et al. and Wright et al. (2015).

Anyhow, the Messinger model and all models based upon it are founded on balance equations and many simplifying assumptions. The accretion is considered as a black box without looking in detail at the physical mechanisms occurring within. Porosity of the accreted ice and effects associated with it, such as capillary flow of liquid water in the pores or a deviant melting behavior are not considered, which limits its applicability to ice crystal accretion. Furthermore, shedding of ice layers, which is rather common in warm icing conditions, is typically not predicted by Messinger based models.

Melting of porous structures or melting of material bound by a solid matrix occurs in a multitude of processes in nature and industrial applications. Fallen snow usually consists of ice crystals, entrapped air and, depending on the weather conditions, more or less liquid water. Natural melting of the snow influences its liquid water content, which affects the snow's behavior significantly, in particular with regard to avalanches (Jomelli and Bertran, 2001). Often fallen snow is melted to clear roads, airport runways or helipads to increase transportation safety (Aoki et al., 1988, Liu et al., 2007). Atmospheric ice crystals which are ingested into aero-engines start to melt as they are exposed to the warm environment of the engine. At a certain melt ratio, they accumulate on stator blades forming a granular (or porous) ice/water accretion, which reduces the engine's power, reliability and efficiency (Currie et al., 2012, Mason et al., 2011, Struk et al., 2011). The melting behavior of such

ice-pack accretion determines its adhesion to the surface, moment of shedding (Kintea et al., 2014b) and therefore the icing severity.

Ice slurries, comprising ice particles suspended in liquid water, are an alternative solution for secondary refrigerants (Ayel et al., 2003), exhibiting many advantages over single-phase fluids. Yet, their handling is more complicated, especially since describing the flow behavior (Kitanovski et al., 2005) and the heat transfer characteristics (Egolf et al., 2005) are very challenging tasks. Since the ice crystals are usually irregular, even prediction of the melting behavior of a single particle is a challenging problem (Kintea et al., 2015b).

Food has been conserved by freezing for thousands of years (Persson and Löndahl, 1993), which often leads to porous structures due to the morphology of the food stuff or by outgassing of air whilst solidifying. The freezing and thawing process of the food significantly influences its quality. Air entrapment in melting solids also affect the melting behavior of ice cream (Watts et al., 1997) or the welding of sintered materials (Chandramouli et al., 2014, Correa et al., 2008, Selcuk et al., 2010). Further applications are magma liquefying porous rock beds (Iwamori, 1993, McKenzie, 1984) or a nuclear meltdown, where the porous rubble of the fuel rods melts (Dosanjh, 1989).

Phase change materials are often used for thermal control of electronics, spacecrafts or buildings. They are capable of storing energy by absorbing or releasing the latent heat of fusion. Usually, the phase changing material is contained in a porous structure of a solid, whereby the non-melting material provides structural stability at the operating temperatures (Nomura et al., 2009, Py et al., 2001, Trelles and Dufly, 2003). During the thawing of frozen ground, soil constitutes a porous structure in which the liquid and air is contained (Ling and Zhang, 2003, Morgenstern and Nixon, 1971).

Melting or solidifying is most commonly computed using the classical Stefan problem (Alexiades, 1992) in which the liquid and the solid phase are separated by an interface of zero thickness. Material properties, such as the specific heat c_p, thermal conductivity k and density ρ are assumed phase-wise constant. The latent heat of fusion L_m, which is also presumed constant, is released or absorbed at the interface during freezing or melting, respectively. It equals the net amount of heat conducted to the interface which is at the melting temperature, other heat fluxes are neglected. An energy balance for a control volume of infinitesimal

thickness containing the moving interface reads

$$[\rho L_m \vec{v}] \cdot \vec{n} = [k_s(\nabla T)_s - k_l(\nabla T)_l] \cdot \vec{n}, \tag{1.1}$$

where the indices correspond to the solid (s) and liquid (l) phase, respectively, $\vec{v}$ is the velocity at which the melting/freezing front propagates and $\vec{n}$ is the normal vector on the interface. The classical Stefan problem describes phase changes of non-porous materials rather well Alexiades (1992) as the underlying assumptions are very reasonable for most cases.

Anyhow, some of them do not apply for the melting of a porous material. The goal of this work is to overcome these limitations for heterogeneous multiphase materials by theoretically modeling the transport phenomena in granular, multiphase materials. These phenomena include heat transfer, melting and liquid phase imbibition. When heat is applied to a porous structure in which one of the phases melts, heat is conducted in the non-melting phase while it is absorbed by the melting phase. The Stefan boundary condition at the interface of melting grains is replaced by a distribution of heat sinks. Hence, the heat flux decays over a certain distance due to the energy expended on melting at the grains' boundaries. Information about thermodynamic conditions at the wall does not propagate beyond this thermal boundary layer. As a result, the interface at which the phase change takes place is not sharp as assumed in the Stefan problem, but smeared over a certain thickness. Moreover, the transport of the liquid by capillary suction into the pores of the solid material is taken into account as well as the convective heat transport associated with it. Such modeling is important for the accurate prediction of the phase change process in porous media as in the examples set out earlier in this section.

1.3 Numerical background and applied methods

With the help of numerical computation methods it is possible to find approximate solutions of equations for which a solution cannot be obtained analytically. Different solution approaches have been developed, such as the Finite-Differences method (FDM), the Finite-Volume method (FVM) or the Finite-Element method (FEM), to mention a few. All of them have in common that the computational domain has to be

divided into a finite number of subdomains, which is called the spatial discretization. For those subdomains a simplified, i.e. discretized, equation is formulated. A subsequent temporal discretization is necessary if a transient process is considered. This discretization process yields a linear set of equations, which is solved numerically.

Owing to its inherent conservative character, the Finite-Volume method is employed in the scope of this work in the framework of the CFD toolbox OpenFOAM. It is written in the language C++ and is available as open source, licensed under the GNU General Public License.

1.3.1 Finite-Volume method

In general, the Finite-Volume discretization comprises the three steps spatial discretization, equation discretization and temporal discretization. The latter is omitted if a steady-state problem is considered. All three steps are explained in the following.

1.3.1.1 Spatial discretization

A subdivision of the domain into a finite number of non-overlapping control volumes is called spatial discretization. These control volumes form a mesh of in the scope of the FVM called "cells". In a three-dimensional mesh, a cell is enclosed by a certain number of flat surrounding surfaces of each cell. Such a so-called "face" is either shared by two cells, i.e. it constitutes the boundary between the two neighboring cells, or it coincides with the boundary of the computational domain. Every face is associated with a unit normal vector $\vec{n}$. Figure 1.8 shows the cell P and its neighbors N, E, S, W according to cardinal directions of a two-dimensional mesh and dots represent cell centroids. The corresponding faces are termed n, e, s, w while the index of the normal vector indicates to which face the vector belongs.

Boundary conditions have to be applied at the bounds of the computational domain for its comprehensive depiction. The most common ones are constant value (Dirichlet boundary condition), constant flux (Neumann boundary condition) or symmetry boundary condition, i.e. zero flux. They are accounted for in the numerical algorithm during the discretization of the governing equations.

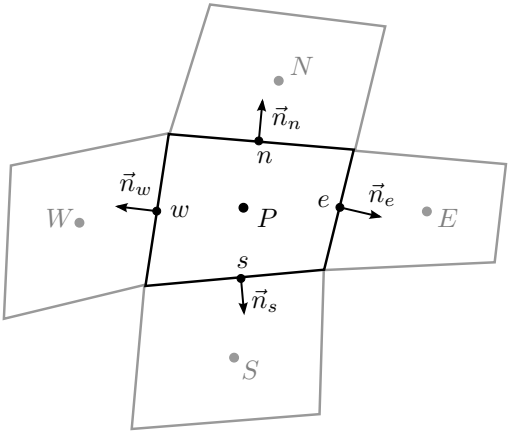

Figure 1.8: Sketch a two-dimensional control volume (black) and its neighbor cells (gray).

1.3.1.2 Equation discretization

The procedure of equation discretization in the framework of the FVM is demonstrated by means of the generic transport equation. It is a parabolic partial differential equation and constitutes the basis for the computation of transport processes of various species, e.g. temperature, mass concentration or momentum. For an arbitrary scalar quantity Φ, it reads

$$\frac{\partial(\rho\Phi)}{\partial t} + \nabla\cdot(\rho\Phi\vec{u}) = \nabla\cdot(\rho D\nabla\Phi) + S_\Phi, \tag{1.2}$$

where t corresponds to time, ρ and $\vec{u}$ are the fluid's density and velocity, respectively. The diffusivity of the quantity Φ is denoted by D and S_Φ is a source. Integrating this equation over a control volume, assuming constant material properties (ρ and D) and making use of Gauss' theorem yields

$$\rho\frac{\partial}{\partial t}\int_V \Phi\,\mathrm{d}V + \rho\int_{\partial V}\Phi\vec{u}\cdot\vec{n}\,\mathrm{d}A = \rho D\int_{\partial V}\nabla\Phi\cdot\vec{n}\,\mathrm{d}A + \int_V S_\Phi\,\mathrm{d}V, \tag{1.3}$$

where V and ∂V correspond to the cell's volume and the surface enclosing it, respectively, and A stands for area. A decomposition of the surface

integrals into the individual faces f of the cell yields

$$\rho\frac{\partial}{\partial t}\int_V \Phi \,\mathrm{d}V + \rho\sum_f \int_f \Phi\vec{u}\cdot\vec{n}\,\mathrm{d}A = \rho D\sum_f \int_f \nabla\Phi\cdot\vec{n}\,\mathrm{d}A + \int_V S_\Phi \,\mathrm{d}V. \quad (1.4)$$

In the next step, the integrals have to be evaluated. This is done by numerical integration, in the scope of this work by means of the second order accurate midpoint rule. Thus, the equation reads

$$\rho V_P \frac{\partial \Phi_P}{\partial t} + \rho\sum_f \Phi_f \vec{u}_f \cdot \vec{n}_f A_f = \rho D\sum_f (\nabla\Phi)_f \cdot \vec{n}_f A_f + S_{\Phi,P} V_P, \quad (1.5)$$

where the index P corresponds to the considered cell over which Eq. (1.2) had been integrated. The next step of the discretization is the expression of Φ_f and $(\nabla\Phi)_f$ at the faces in terms of cell values. Numerous methods for this computation, so-called discretization schemes, with different behaviors of the numerical algorithm are known. For the sake of simplicity, only the most common ones are presented here. Their usage is demonstrated by computing the values at face e of an orthogonal mesh. Other, mostly high-order or blended schemes are found in advanced literature, e.g. by Ferziger and Peric (2012) or Schäfer (2013).

Central Differencing Scheme (CDS) A linear interpolation between the two cells which share the corresponding face, i.e. the cells surrounding it, is given by

$$\Phi(x) = \frac{\Phi_E - \Phi_P}{x_E - x_P}x + \Phi_P, \quad (1.6)$$

where the indices denote the position of the indexed values and x corresponds to the coordinate in direction of $\vec{E} - \vec{P}$ with origin in P. The required value at face e is now computed by

$$\Phi_e = \Phi_E\Theta_e + \Phi_P(1 - \Theta_e), \quad (1.7)$$

where Θ_e is the interpolation factor of face e, defined as

$$\Theta_e = \frac{x_e - x_P}{x_E - x_P}. \quad (1.8)$$

This scheme exhibits second order accuracy with respect to space but can produce unbounded solutions.

Deriving Eq. (1.6) with respect to x yields

$$\left(\frac{\partial \Phi}{\partial x}\right)_e \approx \frac{\Phi_E - \Phi_P}{x_E - x_P}, \tag{1.9}$$

which is the slope of the linear interpolation. It is a common choice as discretization for $(\nabla\Phi)_f \cdot \vec{n}_f$ in Eq. (1.5). Other possibilities like forward or backward-differencing are available but not presented in this work.

Upwind Differencing Schemes (UDS) The value of the cell upstream of the face is applied as face value when using the UDS. For face e it reads

$$\begin{aligned} \Phi_e &= \Phi_P \quad \text{for} \quad \vec{u}_e \cdot \vec{n}_e > 0 \quad \text{and} \\ \Phi_e &= \Phi_E \quad \text{for} \quad \vec{u}_e \cdot \vec{n}_e < 0. \end{aligned} \tag{1.10}$$

This scheme is first order accurate and ensures boundedness. Improved accuracy is provided by the quadratic upwind scheme which utilizes two cell values upstream and one downstream of the face to define a second order polynomial. This function is evaluated at the cell face giving its value in terms of cell values. The result is an unbounded scheme with third order accuracy.

1.3.1.3 Temporal discretization

The result of the spatial discretization described in the previous section is a system of differential equations in time. For each cell, it reads

$$\frac{\partial \Phi_P}{\partial t} = \underbrace{\frac{1}{\rho V_P}\left[\rho D \sum_f (\nabla\Phi)_f \cdot \vec{n}_f A_f + S_{\Phi,P} V_P - \rho \sum_f \Phi_f \vec{u}_f \cdot \vec{n}_f A_f\right]}_{\mathcal{L}(\Phi)}, \tag{1.11}$$

where the values at the faces are known owing to the spatial discretization. If the considered problem is not time-dependent, the derivative $\partial\Phi_P/\partial t$ vanishes, resulting in a linear equation system with one equation and one unknown per cell. In that case, the equation system can be solved without

a temporal discretization. The already discretized part of the equation is abbreviated by $\mathcal{L}$, which only depends on Φ.

Just as the computational domain is discretized by subdividing it into a finite number of discrete control volumes, the time is discretized by dividing the considered time interval into a finite number of discrete time steps. Only at these discrete points in time, the unknown values are computed. At $t = 0$, initial conditions have to be defined, i.e. cell values of the first time step have to be provided. Due to the principle of causality, the values at a certain timestep n can only be influenced by previous timesteps. Similar techniques as for the spatial discretization can be used for the discretization of the transient term, such as forward, backward or central differencing. In the scope of this work, one example of each will be presented where the superscript of Φ corresponds to the time step.

Explicit Euler method This method corresponds to forward differencing in time. The derivative with respect to time is evaluated at the current timestep n. Therefore, it reads

$$\frac{\partial \Phi}{\partial t}(t_n) \approx \frac{\Phi^{n+1} - \Phi^n}{\Delta t_n} = \mathcal{L}(\Phi^n). \tag{1.12}$$

It can be solved explicitly for the next timestep $n + 1$, hence the name. It yields

$$\Phi^{n+1} = \Phi^n + \Delta t_n \mathcal{L}(\Phi^n). \tag{1.13}$$

Cell values at t_{n+1} only depend on the previous timestep n and are therefore completely decoupled from each other. This enables a direct computation of the next timestep from the previous one without having to solve the equation system, which renders the computation of a timestep very efficient. In return, this limits the velocity at which information distributes, effectively limiting the maximum size of the timestep. The Explicit Euler method exhibits first order accuracy with respect to time.

Implicit Euler method The Implicit Euler method corresponds to backward differencing, i.e. the derivative is evaluated at the next timestep t_{n+1} using this timestep and the previous one. It reads

$$\frac{\partial \Phi}{\partial t}(t_{n+1}) \approx \frac{\Phi^{n+1} - \Phi^n}{\Delta t_n} = \mathcal{L}(\Phi^{n+1}). \tag{1.14}$$

Solving explicitly for the values of the next timestep is not possible as cell values are coupled to each other. This necessitates solving a linear equation system for every timestep. The advantage of this first order accurate discretization over the explicit method is that it is unconditionally stable, i.e. no time step limit applies.

Crank-Nicolson method Forming the central differences at $t_{n+1/2}$ to obtain the derivative with respect to time is called Crank-Nicolson method. It yields

$$\frac{\partial \Phi}{\partial t}(t_{n+1/2}) \approx \frac{\Phi^{n+1} - \Phi^n}{\Delta t_n} = \frac{1}{2}\left[\mathcal{L}(\Phi^{n+1}) + \mathcal{L}(\Phi^n)\right]. \tag{1.15}$$

This discretization is of second order and numerically stable. However, under certain conditions unphysical oscillations might occur.

1.3.2 Techniques for free surface flows

Computing processes which involve free surfaces between two phases and their movement is a highly challenging task since the boundary between them is not known in advance as it is part of the problem's solution. A variety of techniques has been developed for the simulation of such flows. The three methods Interface-fitting, Volume-of-Fluid and Level-Set are used in this work and introduced in the following. Figure 1.9 (a) shows an interface I separating phase A from phase B in a two-dimensional square domain. By means of this example the function of the three interface representation methods is demonstrated. Further methods are described in relevant literature, e.g. by Jafari and Ashgriz (2008).

1.3.2.1 Interface-fitting method

If an interface is represented by the Interface-fitting method, it either coincides with a boundary (Christov and Volkov, 1985, Ryskin and Leal, 1984) or internal faces (Fyfe et al., 1988, Hirt et al., 1974) of the mesh. Conditions representing the interface are imposed at those faces, e.g.

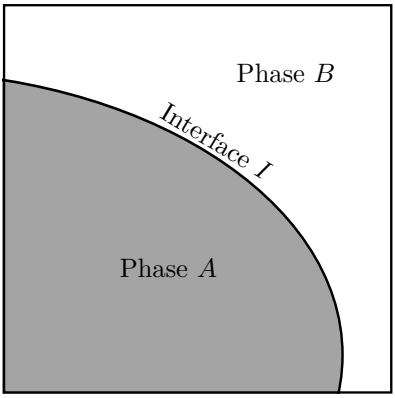

(a) Physical distribution of phases A and B in the domain.

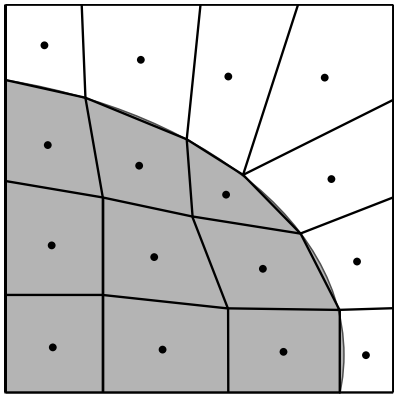

(b) Interface fitting representation of the interface.

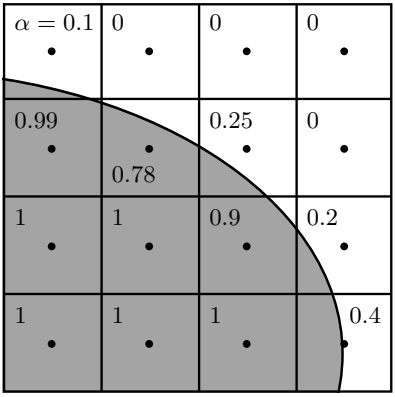

(c) Interface capturing using Volume-of-Fluid approach in a fixed grid. The color function α represents the volume fraction of the cell occupied by phase A.

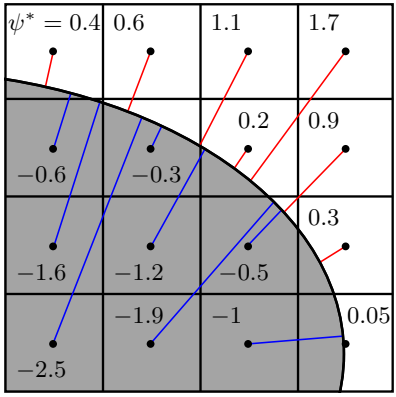

(d) Level-Set representation of the interface between A and B in a fixed grid using a signed distance function for the Level-Set field.

Figure 1.9: Sketch of different interface representation techniques used in this work.

velocity and temperature continuity. This is rather straightforward as they can either be directly applied as boundary conditions (for faces coinciding with the boundaries of the domain) or at internal faces

by taking it into account during the equation discretization. The method provides a sharp, non-diffuse interface representation and the faces representing the interface are forced to move with it. Large interface deformations can result in a heavily distorted mesh which might necessitate the generation of a new mesh. This is usually rather computational costly and therefore constitutes the major drawback of this method. Figure 1.9 (b) shows a 16 cell mesh with a set of internal faces aligned along the interface. Cell centroids are depicted as black dots and the corresponding faces as black lines. Phase A is indicated as a gray surface while phase B corresponds to the white region.

1.3.2.2 Volume-of-Fluid method

In the scope of the Volume-of-Fluid (VOF) method (Hirt and Nichols, 1981) a so-called color function α is introduced. It is a scalar representing the fraction of the corresponding cell volume occupied by the first (heavier) phase. Therefore it ranges from zero, i.e. none of the cell volume is occupied, to unity, which means that the cell is entirely filled. Cells with a volume fraction of $0 < \alpha < 1$, i.e. neither fully occupied nor totally empty, are considered to be on the interface, which is not explicitly tracked. As a result, its exact position is not known but a diffuse region in which it resides. Figure 1.9 (c) shows the VOF representation of interface I in a fixed grid. The original phase distribution is shown and the values of the color function α of each cell are given which are used to represent this composition.

The phases are advected by solving

$$\frac{\partial \alpha}{\partial t} + \vec{u} \cdot \nabla \alpha = 0, \tag{1.16}$$

which ensures mass conservation of the phases. Typically, the VOF approach is combined with interface compression methods (Deshpande et al., 2012, Weller, 2008) which minimize the smearing of the interface and methods for accounting for the surface tension between the two phases, such as the continuum surface force method presented by Brackbill et al. (1992).

1.3.2.3 Level-Set approach

A certain iso-contour of a scalar function ψ represents the interface in the framework of the Level-Set method (Osher and Fedkiw, 2006, Sethian, 1999). Typically, the Level-Set function is defined as a signed distance function to the interface, i.e. its value represents the shortest distance $s(\vec{x}, t)$ of point $\vec{x}$ to the interface while its sign indicates its position with respect to the interface. Therefore, ψ values $+s(\vec{x}, t)$ outside of the considered phase (in this case phase A) and $\psi = -s(\vec{x}, t)$ inside of it. Figure 1.9 (d) shows the Level-Set representation of the example phase distribution. Cell values of the normalized Level-Set field $\psi^* = \psi/\delta x$, where δx corresponds to the cell edge length, are given and the distances are depicted as lines from the cell centroids to the interface. Blue lines correspond to negative distances within phase A, while red lines are positive distance values outside of the considered phase. The bound between the phases is located at the iso-contour $\psi = 0$ and is therefore a sharp interface.

Advection of the phase A is achieved by solving

$$\frac{\partial \psi}{\partial t} + \vec{u} \cdot \nabla \psi = 0. \tag{1.17}$$

Since the value of ψ is not directly related to the mass of the phases, this equation does not ensure mass conservation. In fact, unphysical mass loss as reported by Chang et al. (1996), Tornberg and Engquist (2000) is a major drawback of this method. Also, the ψ-field does not necessarily retain its signed distance character throughout the computation (Berthelsen, 2002), which makes a re-initialization of the field necessary. Advantages of this method are the sharp interface representation and the possibility of using a fixed grid.

1.4 Scope of this work

The focus of this work lies on the improvement of the understanding of the physical mechanisms leading to ice particle accretion as well as the development of novel models describing them. To do so, experimental investigations, theoretical considerations and modeling and numerical investigations are performed. This is done separately for each subprocess described in section 1.2.

A theoretical model for the **melting of non-spherical particles**, what atmospheric ice crystals usually are, is presented in chapter 2. It assumes the particles to be spheroidal with an accumulation of the melt water in the region of lowest surface curvature of the particle, which is due to capillary forces. This model is implemented in a Finite-Volume algorithm with the help of the Level-Set method. Obtained results are compared with experimental data exhibiting very good agreement and superiority of the model over the 1D sphere model. Moreover, parameters which are critical for ice accretion, such as the particle melt ratio, deviate significantly from the results the 1D sphere model provides.

To investigate the **impact behavior of small particles on a liquid film**, a numerical algorithm has been developed which takes into account capillary forces, in particular forces arising at the contact line. The solid particle is represented by a moving interface fitted mesh while the interface between liquid and gaseous phase is accounted for via a Volume-of-Fluid method. The obtained results have shown that the wettability of the particle, the ratio between solid and liquid density and the Weber number are the influencing factors which decide whether a particle penetrates an interface or sticks to it. Code implementation, numerical results and the dimensional analysis leading to these results are presented in chapter 3.

If particles accrete on a surface, the accreted layer's thermal behavior, in particular its melting, determines its composition and therefore its behavior with regard to connection strength to the surface and shedding. A **detailed numerical model of the accretion** which resolves individual crystals and droplets by means of a Volume-of-Fluid method is presented in chapter 4. Melting, evaporation and heat conduction in the wall as well as in the porous accretion are accounted for in this approach. Available icing experiments were successfully reproduced by this code and thermal icing limits were computed which are in very good agreement with the experimental database.

With the help of the results of the detailed accretion model in combination with a dimensional analysis, a **model for the effective thermal properties of a porous ice/water accretion** is developed and presented in chapter 5. It accounts for heat propagation in a melting porous body as well as the imbibition of liquid water into its pores. Subsequently, this model is implemented in the framework of a Finite-Volume code which allows using a mesh significantly coarser than for the detailed model. As a result, the icing on an entire airfoil can be

computed with reasonable computational effort. Numerical results exhibit very good agreement with available accretion experiments.

PART ONE:
Single crystal behavior

The center of attention in this part is the behavior of single ice crystals. In particular the melting of ice particles and their impact onto a liquid surface is considered.
When ingested into a warm engine, particle and flow are decelerated and accelerated unequally leading to a relative velocity between particle and local flow which is heated due to compression. The convective heat and mass transfer arising herefrom heats and eventually melts the particle during its residence time in the compressor of the engine. As a result, a mixture of solid ice and liquid water emerges which is capable of accreting on engine components. The strong dependence of the icing severity on the ratio of liquid to total water content in the flow underlines the significance of an accurate prediction of the melting process. For this purpose, a theoretical model is developed in this work, presented in chapter 2. It accurately describes the melting of non-spherical particles with significantly higher accuracy than currently applied models which are based on the assumption of spherical particles.
The impact process of the (partially melted) particles on a liquid surface determines whether particles are able to penetrate the interface or are captured by it. Thus, the impact is of vital importance for the growth rate of an ice accretion. It is governed by pressure and viscous drag as well as surface tension forces; all contributions are considered in this work. The developed numerical model, presented in chapter 3, is capable of describing the impact and penetration of the interface or the capturing of the particle at the liquid surface.

2 Melting of non-spherical ice crystals

ABSTRACT Melting of irregular ice crystals was observed in an acoustic levitator. The evolution of the particle shape is captured using a high-speed video system. Several typical phenomena have been discovered: change of the particle shape, appearance of a capillary flow of the melted liquid on the particle surface leading to liquid collection at the particle mid-section (where the interface curvature is smallest), and appearance of sharp cusps at the particle tips. No such phenomena can be observed during melting of spherical particles.

An approximate theoretical model is developed which accounts for the main physical phenomena associated with melting of an irregular particle. The agreement between the theoretical predictions for the melting time, for the evolution of the particle shape and the corresponding experimental data is rather good.

This chapter is based on the article *Shape evolution of a melting nonspherical particle* by Kintea et al. (2015b), published in Physical Review E, and the conference contribution *Melting of non-spherical particles* by Kintea et al. (2015a).

Contents

2.1 Context

This chapter presents an experimental investigation and a theoretical model for the melting process of irregular, non-spherical particles. The work leading to these results has been performed in collaboration with Tobias Hauk of Airbus Group Innovations, who conducted the experiments.

Whether or not ice particles accrete on surfaces and the severity of the icing sensitively depends on the ratio of liquid to total water content as shown in Fig. 1.3. Thus, the accurate description of the melting process of ice crystals is of vital importance for predicting icing. For this purpose a theoretical model is developed and presented in this chapter.

The model accounts for the main phenomena associated with irregular particles and observed in experiments, namely the capillary flow of the melted liquid, leading to its collection at the particle mid-section, where the interface curvature is smallest, and appearance of the cusps at the particle tips. The results obtained with this model are compared with experimental data of melting of grinded irregular ice particles and agree very well with the experimental data. It is shown that the composition of the ice particles deviates significantly throughout the melting process from that of spherical particles, resulting in a significant impact on the icing behavior. Therefore, taking this into account in icing codes has the potential to increase the prediction accuracy significantly.

2.2 Experimental method

An experimental study for melting of irregular ice particles was carried out to observe the variation of their shapes and to measure the typical times, corresponding to the complete transformation into a spherical drop and to complete particle melting. In these experiments ice particles in an acoustic levitator (Yarin et al., 1997, 1998) are melted by a forced convection flow with variation of particle size and shape, temperature and humidity of the incident air flow as well as the flow velocity.

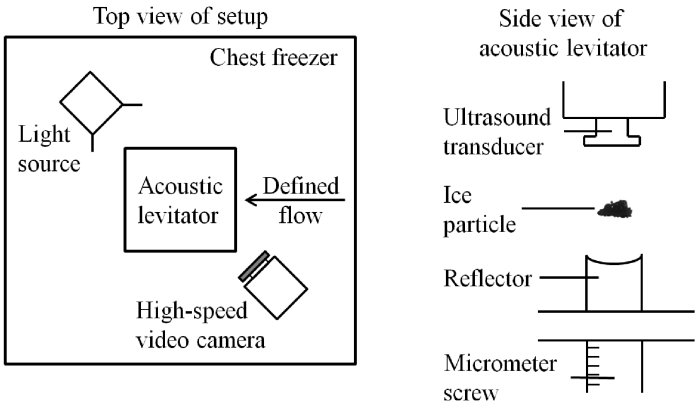

Figure 2.1: Sketch of the experimental setup and levitator.

2.2.1 Experimental setup

In Fig. 2.1 a sketch of the experimental setup is shown. The main components of the setup are an acoustic levitator used to suspend single ice particles, an optical and recording system to record the melting particle with a decent magnification, and a flow supply and control system which generates a defined air flow.

Acoustic levitator An acoustic levitator (tec5 AG, Oberursel, Germany) is used for suspension of a particle in a standing acoustic wave, generated between an ultrasound transducer and concave reflector. The working frequency of the levitator is 58 kHz.

Several equally spaced nodes and antinodes of sound particle velocity and sound pressure can be identified in the standing wave. Particles, whose density ranges from 0.5 to 2 g/cm^3, can be levitated just below the pressure nodes in the stable region due to the axial levitation force and the Bernoulli stress which stabilizes the suspended particle radially. The magnitude of the acoustic force is controlled by setting the power level of the acoustic levitator.

In our experiments the acoustic levitator is located in a chest freezer. This allows one to keep a definite initial ice particle temperature determined by the surrounding temperature. The surrounding, hence the

initial ice particle temperature, is measured by a resistive temperature detector (RTD) sensor (Pt100) attached to the levitator close to the ice particle position. A DP9602 high accuracy digital thermometer (OMEGA, Stamford, USA) is used.

Flow supply and control system The ice particle is melted by a warm, uniform, and controlled airflow. The pressurized air (at 1 bar and 20 °C) is passed through several gas washing bottles filled with water to control the relative humidity of the airflow. The humidified air is then passed through a coil of copper tube immersed in a temperature-controlled water bath to control the air temperature. The mass flow rate of the pressurized air is controlled using an FMA-2600 mass flow controller (OMEGA, Stamford, USA).

Finally, the air flows through a flow tube which contains 20 screens to generate a nearly uniform velocity profile in the experimental cell. The tube, made of aluminum, is thermally insulated.

The levitated ice particle is positioned on the extended axis of the flow tube and is located approximately 5 mm away from the tube open end.

The temperature of the airflow is measured with a RTD sensor (Pt100). A B-530 humidity sensor connected to a GL220 data logger (both from Graphtec Corporation, Yokohama, Japan) is used to measure the relative humidity. A pressure transducer system (Aerolab LLC, Laurel, USA) measures the ambient pressure.

Optical and recording system A Phantom v611 high-speed video camera (Vision Research Inc., Wayne, USA) attached to a SZX10 microscope (Olympus Corporation, Tokyo, Japan) is used for the observation of the melting process. A Dedocool cold light source (Dedo Weigert Film GmbH, Munich, Germany) illuminates the ice particle suspended in the acoustic field. Frame rates of the camera during capturing of the melting process ranged from 120 to 250 fps. Typical values of pixel resolution, exposure time, and overall resolution were approximately 156 pixels per mm, 500 µs, and 752 × 504 pixels, respectively.

Between flow and line of sight, there is an angle of approximately 50°. That means that the true dimensions of the ice particle during its melting have to be corrected accounting for the particle orientation in the levitator.

The majority of the particles is usually aligned perpendicular to the flow. Therefore, the estimation of the particle dimensions from its projection on the camera view can be based on the known angle between the flow vector and the axis of view. This angle (50°) is determined by the configuration of the levitator.

2.2.2 Test procedure and conditions

Particle generation Non-spherical ice particles are collected from the ice layer grown on the walls of a chest freezer at temperatures in the range of −15 to −25 °C. Cold tweezers are then used to place an ice particle in the acoustic levitator.

A spherical ice particle is generated by melting a non-spherical ice particle until approximately 90 % of its mass is liquid. Then, the warm airflow is stopped and a spherical particle is generated by refreezing, usually within seconds due to the residual ice core acting as a seed for crystallization.

Particle melting The power of the acoustic levitator is adjusted to ensure that the particle will not be blown out of the acoustic field by the airflow but the shape of the completely melted ice particle will not be strongly distorted by an acoustic pressure and remain nearly spherical. By adjusting the mass flow controller and the temperature of the water bath, the flow velocity and temperature are set.

When steady-state airflow conditions are reached, the flow tube, which is initially kept outside of the chest freezer, is placed in its mount next to the ice particle. A few seconds before the placement of the tube in its mount, the camera is started to record both the initial unaffected particle and the melting process.

Exemplary time sequences captured using the camera are shown in Figs. 2.2, 2.3 and 2.4. Due to the melting of the irregular particle not only the size of the solid part reduces, but also its irregularities are smoothed. The melted liquid always collects in the mid-section of the particle. After some time sharp cusps are formed at the particle tips. Such phenomena do not occur during melting of a spherical particle (Fig. 2.4) due to symmetry of its geometry. Similar phenomena have been observed by Knight (1979) during ice flakes melting.

Table 2.1: Operating conditions for the presented cases 1–3. Ambient pressure and temperature are denoted by p_∞ and T_∞, respectively, while T_0 corresponds to the initial particle temperature. The relative humidity of the flow is denoted by φ which flows at a velocity of u and the particle shape is characterized by its maximum dimension $d_{\max}$, initial mass m_0 and aspect ratio E. Measured overall melting times are denoted by $t_{m,\mathrm{expt}}$.

		Case 1	Case 2	Case 3
p_∞	(kPa)	95.30	95.87	95.33
T_∞	(K)	288.25	292.88	293.22
T_0	(K)	254.75	257.53	255.95
φ	(%)	61	4	56
u	(m/s)	0.751	0.990	1.25
$d_{\max}$	(mm)	2.43	3.49	0.837
m_0	(ng)	267.4	232.2	233.6
$t_{m,\mathrm{expt}}$	(s)	14.46	13.78	7.06
E	(-)	5.07	9.39	1.1

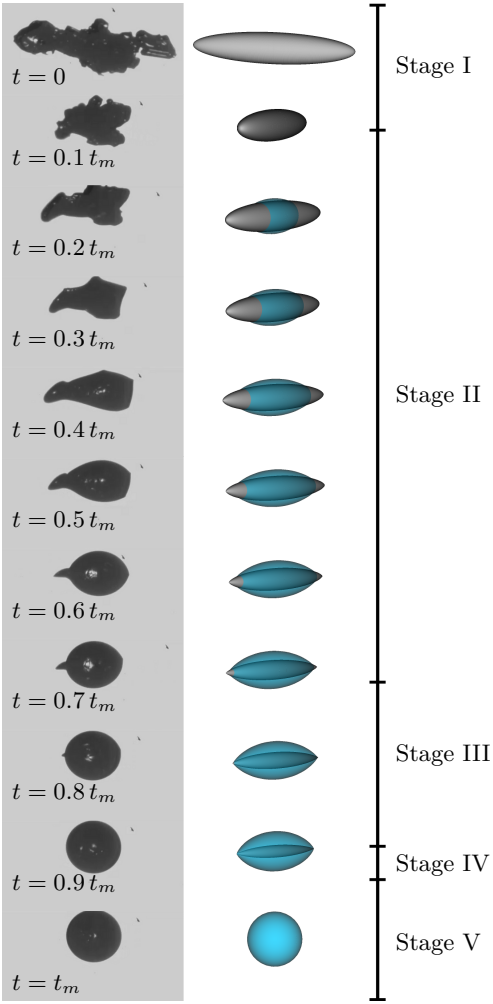

Figure 2.2: Comparison of the non-collapsing ice particle shape with the theoretical predictions for the operational conditions corresponding to case 1 from Table 2.1. Experimental results are shown on the left while the corresponding computed shape is shown on the right.

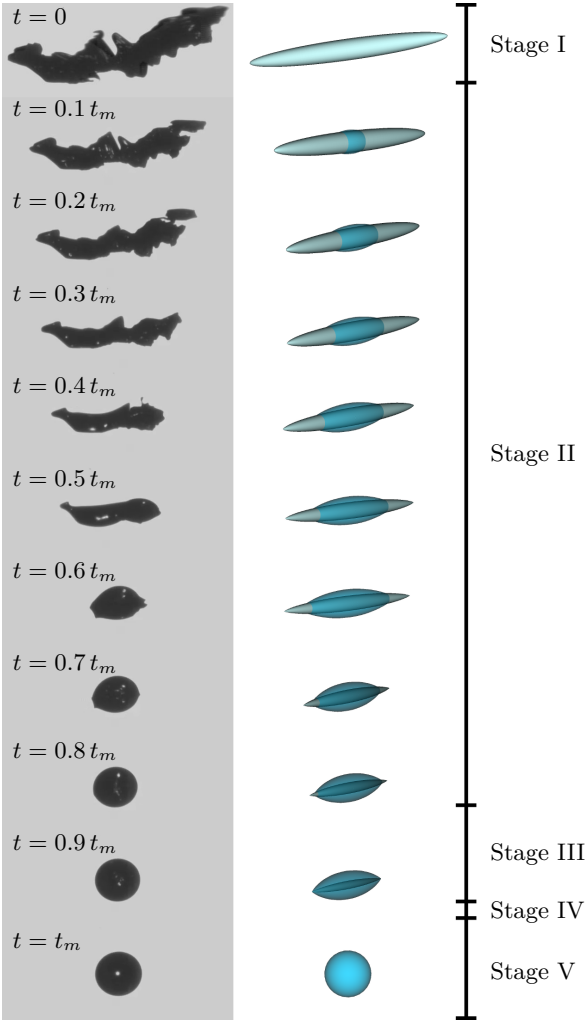

Figure 2.3: Comparison of the observed particle shape with the theoretical predictions for the operational conditions corresponding to case 2 from Table 2.1. At $t \approx 0.55 t_m$ the particle collapses due to surface tension of the accumulated melted water.

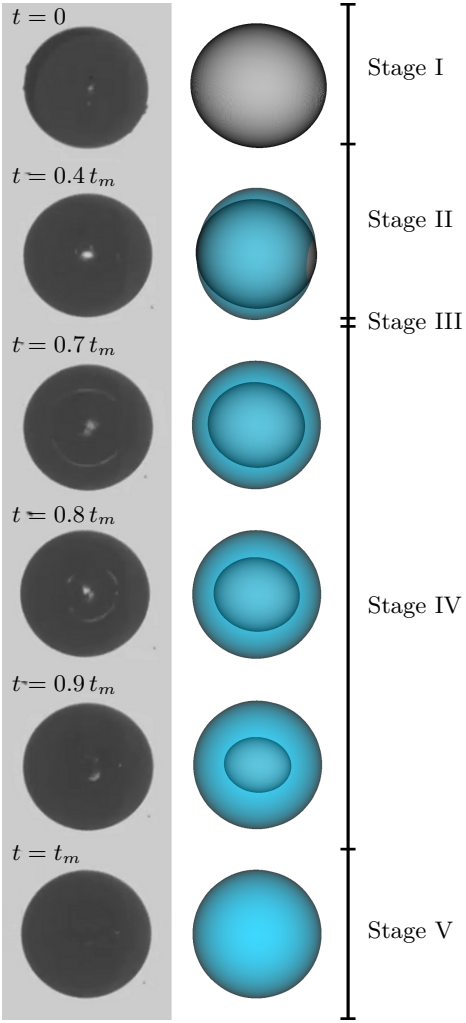

Figure 2.4: Comparison of a nearly spherical ice particle shape with the theoretical predictions for the operational conditions corresponding to case 3 from Table 2.1, and aspect ratio of $E = 1.1$. As a result of the low aspect ratio, the melting stages II and III make up only a small fraction of the entire melting time. Most of the melting takes place in stage IV, which corresponds to the 1D sphere model.

The ice particle shown in Fig. 2.3 breaks up during melting. Such a possibility has been previously mentioned for snow flakes by Gunn and Marshall (1958) and Knight (1979).

2.3 Approximate Model for the particle shape

2.3.1 Mechanisms of particle melting

Five main stages of the melting process can be identified. Stage I is characterized by the warming of a particle without phase change up to the melting temperature. In stage II the particle begins to melt, leading to water accumulation in the area of lowest curvature, as can be seen in Fig. 2.2 and 2.3. The shape of the liquid water is determined by the total volume of the melted liquid and by the contact angle, which for ice is $\theta = 12^\circ$ (Knight, 1967). The apparently dry portions of the particle surface are in fact wetted due to melting. The thickness of the liquid film in these regions is small, however, the camera does not resolve this film. During stage III the solid particle is completely covered by a non-spherical liquid droplet, pinned at the particle tips. In stage IV the length of the ice portion is smaller than the drop diameter – the particle is completely immersed in the liquid drop. In the final stage V the completely melted liquid drop is heated above the melting temperature.

During the first stage (I) the thermal effects associated with the temperature gradients in the solid, and development of the thermal boundary layer, are small. The lumped capacitance method predicts the evolution of the average particle temperature rather well since the Biot number of the particle, $\mathrm{Bi} = \mathrm{Nu}k_A/k_P$, is small. Here Nu is the Nusselt number, k_A and k_P are the thermal conductivities of the air and of the particle, respectively.

During the second stage (II) the mechanism of melting of a non-spherical particle is influenced significantly by a capillary flow of the melted liquid on the particle surface. The pressure in a liquid film covering the particle of a typical size d can be estimated using the Young-Laplace equation, $p \sim \sigma/d$, where σ is the surface tension of the liquid. The typical velocity in the film of thickness H_f is estimated from the mass balance equation as $u \sim u_m d/H_f$, where u_m is the typical melting velocity. This velocity can be estimated from experiments through $u_m \sim d/t_m$. Here

t_m is the total melting time. Finally, the film thickness can be estimated from the momentum balance equation $p/d \sim \mu u/H_f^2$ (μ being the liquid viscosity) which considers the forces related to the pressure gradient in the liquid film and the viscosity effects. The resulting estimation for the liquid film thickness is

$$H_f \sim \frac{d^{4/3}\mu^{1/3}}{\sigma^{1/3}t_m^{1/3}}. \tag{2.1}$$

In our experiments the typical melting time of a millimetric particle is approximately 10^1 seconds. Expression (2.1) yields $H_f \sim 10$ µm. The influence of the thin film on the heat transfer in the particle is rather small. It will be neglected in the further analysis.

2.3.2 Main assumption for modeling

Since the thermal conductivity of the particle is much higher than that of the surrounding gas, the temperature gradient in the particle is relatively small. The Stefan number

$$\mathrm{St} \equiv \frac{c_p \Delta T}{L_m}, \tag{2.2}$$

represents the ratio of the sensible heat to the heat spent on melting. In our case the specific heat for ice is $c_{p,I} = 2060$ and for water is $c_{p,W} = 4180$ J/(kg K), the latent heat of melting $L_m = 3.33 \cdot 10^5$ J/kg. The maximum Stefan numbers in our experiments are therefore $\mathrm{St}_I \approx 0.12$ for ice and $\mathrm{St}_W \approx 0.3$ for water. These numbers are based on $\Delta T = T_m - T_0 = 20$ K for ice and $\Delta T = T_\infty - T_m = 25$ K for water, where T_m is the melting temperature, T_0 is the initial particle temperature, T_∞ is the surrounding gas temperature.

Since the Stefan numbers are small, the particle can be considered to be isothermal throughout the melting process as has already been assumed by Mason (1956) for spherical geometry. Figure 2.5 compares melting times of spherical particles once obtained by the one-dimensional isothermal sphere model $t_{m,\mathrm{1D}}$ and once by a detailed numerical simulation which takes into account heat conduction in solid and liquid regions of the melting spherical particle $t_{m,\mathrm{DNS}}$. It compares the melting times of particles melted at three different ambient temperatures ϑ_∞ (ϑ is the temperature on the Celsius scale). The employed numerical algorithm is based on the enthalpy method and is spatially discretized

one-dimensionally using finite volumes. In this approach no liquid flow is considered and therefore only conductive heat fluxes are accounted for in the solid and the liquid phase. A heat flux, derived from suitable Nusselt correlations, is applied on the outer boundary of the initially solid particle. This heat flux heats the particle up non-uniformly until it reaches its fusion temperature, followed by the movement of the solid-liquid interface towards the particle center.

It is known that modeling of the melting of nano-particles leads to the appearance of a singularity in the solution as the particle radius goes to zero. At small particle radii the effect of the dependence of the melting temperature on the particle curvature becomes significant. Back et al. (2014) show that this singularity can be avoided by accounting for the kinetic effects. The total melting time of a nano-particle is finite and much shorter than the typical melting time considered in our experiments. Therefore, the singularity effects almost do not affect the results of the present study.

The deviation between the two models slightly increases as the flow temperature, and therefore the heat flux, rises. Also, a dependency on the particle size is observed. This dependency has nearly no influence when considering ice particles of the size of a few millimeters suspended in air. In all considered cases, the isothermal sphere model yields slightly lower melting times than the detailed numerical simulation. This is explained by the time, the heat needs to be conducted towards the ice core of the particle, which is neglected in the isothermal model. Anyhow, the deviations are rather low when considering ice particles suspended in air and moderate temperature differences. The assumption of isothermal particle will then be applied also to the description of non-spherical particle.

2.3.3 Numerical algorithm

It is known that heat transfer coefficients depend on the particle shape, and that the heat flux at the particle surface is not uniform. Nevertheless, these effects are secondary in comparison with the influence of the liquid redistribution. Therefore, as a zero approximation we assume a uniform distribution of the average heat flux on the particle surface, which is derived from the heat transfer for a volume-equivalent sphere. In this case the evolution of the particle shape is determined completely by the

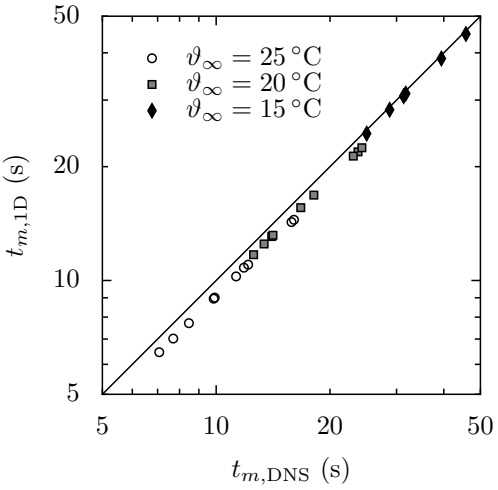

Figure 2.5: Comparison between melting times obtained by the isothermal sphere model and from a detailed numerical simulation (DNS), taking into account the temperature field in the spherically assumed ice particle. Results were generated assuming an ambient pressure of $p_\infty = 96$ kPa at ambient temperatures ϑ_∞, a flow velocity of 1 m/s, dry air and an initial particle temperature of 255 K. The size of the particles varies between 0.5 and 0.8 mm.

uniform melting velocity $\vec{u}_m$ and is described by an Eikonal equation (Whitham, 1999). In fact, the problem is reduced to the computation of the surface propagation with a uniform velocity in the normal direction. For a three-dimensional case the most convenient technique of solution of this equation is based on the Level-Set method (Sethian, 1999). This computational method allows calculation of equidistant surfaces which describe the shape of the melting particle in time assuming a uniformly distributed heat flux. The family of these surfaces is determined only by the initial body shape.

In Fig. 2.6 two examples of the surface evolutions are shown, which are analogous to a melting of a single bump on a planar surface, and to the melting of a spheroid. These simulations explain the smoothing of a surface leading to the bump elimination. Similar surface smoothing has been observed earlier during melting of artificial hailstones presented by Bailey and Macklin (1968). The example in Fig. 2.6 demonstrates also an appearance of the sharp cusps, where the local curvature radius vanishes. This situation is analogous to the mechanism of cusp formation on a rim bounding a free liquid sheet (Roisman and Tropea, 2002, Yarin and Weiss, 1995) and analyzed in the study on the emergence of singularities during melting processes (Howison et al., 1985). The cusp is formed since the local curvature radius changes linearly with the propagation distance of the interface. At some time instant the curvature vanishes, which corresponds to the appearance of the cusp.

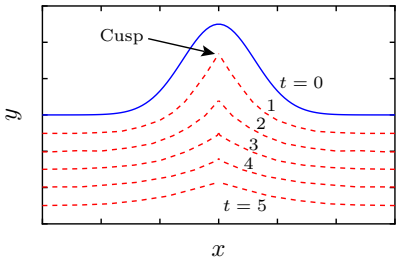

(a) Smoothing of a bump.

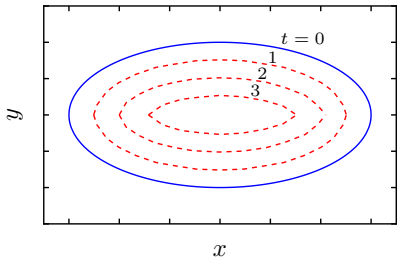

(b) Cusp formation.

Figure 2.6: Examples of the theoretically predicted evolutions of the shapes of a bump on a planar surface, and of an ellipse. The dimensionless velocity $u_m = 1$.

Stages II and III do not appear during the melting of a spherical particle. The heat transfer and particle melting during phases IV and V can be well predicted by the well-known models based on the spherical drop/particle shape presented by Carslaw et al. (1959).

2.3.4 Estimation of the heat flux and of the typical melting rate

In order to describe the melting process of a non-spherical particle we approximate its initial shape by a spheroid, keeping the volume and the maximum dimension $d_{\max}$ the same as for the particle. The melting velocity u_m is evaluated from the energy balance. The heat flux at the particle surface (VDI-Gesellschaft Verfahrenstechnik und Chemieingenierwesen (GVC), 2005) is determined by the particle and surrounding gas temperatures, particle relative velocity and the thermodynamic properties of the gas.

Applying the heat and mass transfer coefficients of a volume equivalent sphere on the surface A_A of the solid and/or liquid particle which is in direct contact with the airflow yields the heat flux

$$\dot{Q} = A_A[\Gamma_H(T_\infty - T_P) + \Gamma_M(\chi_\infty - \chi_P)L_{\mathrm{ev}}M_{\mathrm{H2O}}]. \tag{2.3}$$

Heat and mass transfer coefficients are denoted by Γ_H and Γ_M while T and χ stand for temperature and molar concentration. The indices correspond to far-field conditions (∞) and values at the particle surface (P). This heat flux is composed of a convective heat transfer component visible in Eq. (2.3) as the first term in brackets. The second term is a specific mole flux multiplied with the latent heat of evaporation L_{ev} and the molar mass of water M_{H2O} yielding the heat transfer accompanying a convective mass flux, e.g. evaporative cooling. A suitable Nusselt correlation (VDI-Gesellschaft Verfahrenstechnik und Chemieingenierwesen (GVC), 2005) for a sphere is employed to derive the heat and mass transfer coefficients. This Nusselt number $\mathrm{Nu_{Sp}}$ of a sphere comprises a laminar component

$$\mathrm{Nu_{lam}} = 0.664\sqrt{\mathrm{Re}}\,\mathrm{Pr}^{\frac{1}{3}}, \tag{2.4}$$

and a turbulent contribution

$$\mathrm{Nu_{turb}} = \frac{0.037\,\mathrm{Re}^{0.8}\,\mathrm{Pr}}{1 + 2.443\,\mathrm{Re}^{-0.1}(\mathrm{Pr}^{2/3} - 1)}, \tag{2.5}$$

where Re and Pr denote the Reynolds and Prandtl number, respectively. Blending the two components by

$$\mathrm{Nu}_{\mathrm{Sp}} = 2 + \sqrt{\mathrm{Nu}_{\mathrm{lam}}^2 + \mathrm{Nu}_{\mathrm{turb}}^2}, \tag{2.6}$$

yields the Nusselt number for a sphere. This value is used to derive the applicable heat transfer coefficient

$$\Gamma_H = \frac{\mathrm{Nu}_{\mathrm{Sp}}\, k_A}{d_{\mathrm{eq}}}, \tag{2.7}$$

where k_A is the thermal conductivity of the surrounding fluid and d_{eq} corresponds to the diameter of a volume equivalent sphere which is the characteristic length of the problem. The mass transfer coefficient is computed with the same set of equations by substituting Pr with the Schmidt number $\mathrm{Sc} = \mu_A/(\rho_A D)$ and Nu with the Sherwood number $\mathrm{Sh} = \Gamma_M\, d_{\mathrm{eq}}/D$. The diffusion coefficient of the material the particle is made of in the ambient fluid is denoted by D while μ_A denotes the surrounding fluid's dynamic viscosity. Assuming that the obtained heat flux $\dot{Q}$ is evenly spread over the surface of the solid ice A_I yields the melting velocity $\vec{u}_m$ which is constant over the surface. It reads

$$\vec{u}_m = -\frac{\dot{Q}}{L_m \rho A_I} \cdot \vec{n}, \tag{2.8}$$

where the vector $\vec{n}$ is the unit normal vector on the surface of the ice, L_m is the latent heat of fusion and ρ is the density of the ice. By integrating this velocity over the time t a new shape of the solid fraction of the particle is found which is subsequently used to obtain the melted volume V_m.

2.4 Results and discussion

In the second phase the shape of the solid part is computed using the Level-Set method, mentioned above. The volume of the liquid is estimated from the mass balance of the entire particle. Since the dynamic effects in the liquid portion are small, its quasi-static shape can be approximated by an axisymmetric constant-mean-curvature surface, whose analytical solution is known (Orr et al., 1975).

According to his solution, in the cylindrical coordinate system the shape of the liquid interface has to satisfy the following equation

$$\frac{1 + r_z^2 - r r_{zz}}{r(1 + r_z^2)^{3/2}} = \kappa, \tag{2.9}$$

where r is the radius of the local interface, and z is the axial coordinate. The local curvature κ is constant.

The solution of (2.9) yields

$$z = \pm \int \frac{\mathrm{d}r}{\sqrt{\frac{4r^2}{\kappa^2(r^2-\phi)^2} - 1}}, \tag{2.10}$$

where ϕ and κ are constants, obtained from the conditions of a given volume of the liquid part and a given local contact angle.

Examples of the theoretical predictions of the particle shape are shown in Figs. 2.2, 2.3 and 2.4. The predictions agree rather well with the observed particle shapes. Operational parameters of these three cases are given in Table 2.1. Case 1 is a typical case where irregularities are smoothed in the beginning of the melting process and sharp cusps appear at a later stage. Figure 2.7 shows the projected particle length l_{proj} non-dimensionalized with the diameter of a volume-equivalent sphere d_{eq} over time. For the computation of the projected length the particle is assumed to align with an angle of 50° to the line of sight owing to the experimental setup.

The melting process of case 2 exhibits peculiarities which could be observed in approximately 10 % of the cases. At $t \approx 0.55 t_m$ the particle collapses due to surface tension forces in the accumulated meltwater. Such a particle collapse usually results in a less precise prediction of the melting time, as the surface area evolution deviates from the idealized one. This collapse also manifests itself in the evolution of the projected particle length. Figure 2.8 shows this length over time for case 2. After the collapse, the particle is nearly spherical in the experiment.

A nearly spherical particle with an aspect ratio of $E = 1.1$ is considered in case 3. In this case, the melting in stage IV dominates the process. This stage corresponds to the one-dimensional sphere model. If the aspect ratio is further reduced, the duration of stages II and III decrease until at $E = 1$ the sphere model is recovered.

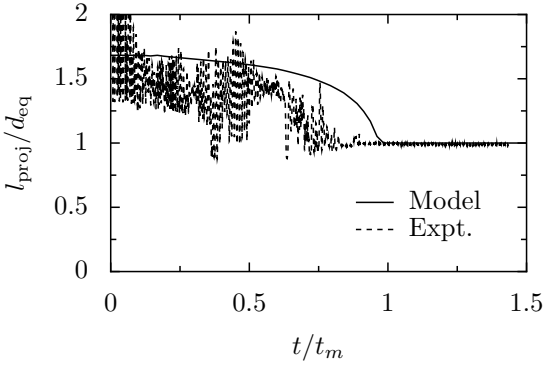

Figure 2.7: Projected length l_{proj}, non-dimensionalized with the diameter of a volume-equivalent sphere d_{eq}, of case 1, defined in Table 2.1.

Figure 2.9 shows the modeled surface area A_A non-dimensionalized with the surface of a volume equivalent sphere A_{Sp} as the particle melts. During the first stage this area remains constant as no phase change occurs. The second stage exhibits a nearly linear surface area change and makes up most of the melting time in all of the considered cases, except the spherical particle shown in Fig. 2.4. The theory predicts the end of the second stage at the time instant $t \approx 0.8t_m$, which agrees very well with the experimental observations for a wide range of parameters. It is obvious that a model based on a spherical particle shape is not able to predict such times, typical for the non-spherical shapes.

Figure 2.10 shows the predictions made by the spheroid model for the total melting times in comparison with experimental data. In the experiments the initial ice crystal temperature was between -18 and -17 °C, the air velocity ranged between 0.75 and 1.25 m/s, the relative humidity between 2.2 and 78 % and the characteristic particle size varied between 0.5 and 1.2 mm. While for the model a prolate shape was always assumed, the real particles exhibited prolate and oblate geometries, indicated by the symbol.

The standard deviation of the results obtained from the sphere-model values 22.6 % while it is only 9.4 % for the spheroid-model; an improvement of 58 %. For only few cases, the 1D sphere-model yielded superior results. In most of these cases the particle collapsed during

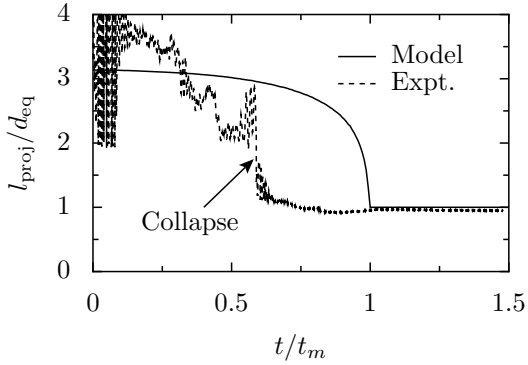

Figure 2.8: Projected length of case 2, defined in Table 2.1.

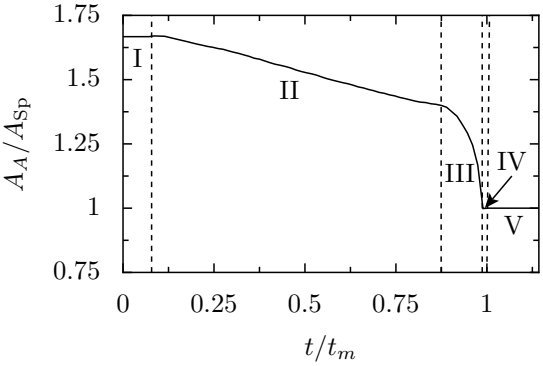

Figure 2.9: Ratio of the modeled surface area A_A to the surface area of a volume equivalent sphere A_{Sp} during the melting process. The distinct melting stages are indicated by dashed vertical lines. The operational parameters are the same as in Fig. 2.3 (Case 2 from table 2.1).

the melting process due to capillary forces of the meltwater leading to a nearly spherical shape. This explains why for those experiments the predicted melting time using the sphere-model yields better results than the spheroid-model, which does not account for geometry changes other than the melting driven change. When neglecting the collapsing cases for the computation of the standard deviation it even reduces from 24.3 % to

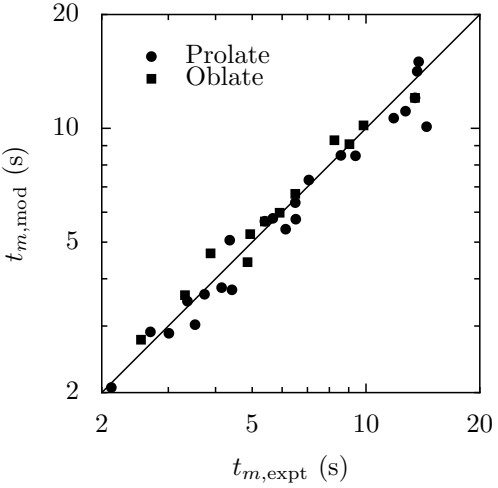

Figure 2.10: Comparison of the theoretical predictions (spheroid model) for the total particle melting time with the experimental data. The data include also the total melting times of the particles collapsed during the melting process.

8.3 % which is an improvement over the 1D sphere-model of nearly 66 %.

Comparing the results obtained by the presented model with the one-dimensional sphere model, the difference in melting time only depends on the aspect ratio and the initial temperature ϑ_0 of the particle. Figure 2.11 shows the melting time difference between the models Δt normalized with the melting time of the spheroid $t_{m,E}$ over the aspect ratio. At $E = 1$, the models coincide and no difference emerges. With increasing aspect ratio, the difference between the models increases. A melting process with no warming up of the particle, i.e. $\vartheta_0 = 0$ °C is shown as a solid line while the dashed lines correspond to particle starting temperatures of $\vartheta_0 = -20$ °C, -40 °C and -60 °C. The colder the particle initially is, the larger this difference becomes.

The temporal development of the melt volumetric ratio predicted by the sphere model is linear due to the constant surface area over the entire melting process. In this study the surface area is time dependent, resulting in a non-constant heat flux and, therefore, a non-linear development of the melt ratio in time. This leads to a time dependent deviation in the

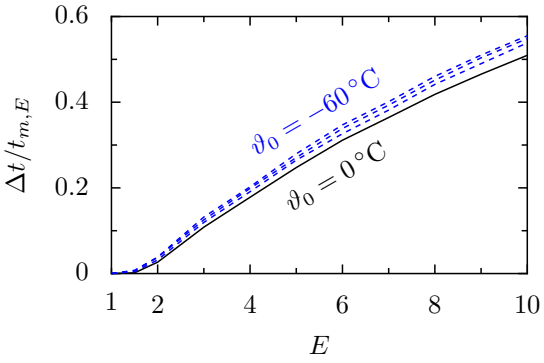

Figure 2.11: Difference of melting time predicted by the sphere model and the spheroidally assumed particle over the aspect ratio E.

melt ratio between the two models, which is zero at the beginning and at the end of the melting process and has a maximum in-between. This maximum deviation of water volume $\Delta V_{l,\max}$ normalized with the entire particle volume V_P, yielding the melt ratio, is shown in Fig. 2.12. The deviation is shown for four different initial particle temperatures from 0 °C to −60 °C in steps of 20 °C. It rises with increasing aspect ratio E and decreasing particle starting temperature ϑ_0. This result demonstrates the importance of accounting for the particle shape in the modeling of its melting, since the approximation of its shape by a sphere is not appropriate for non-spherical particles.

2.5 Conclusions

An experimental investigation of the melting process of non-spherical particles is carried out using an acoustic levitator. Phenomena, typical for process, are observed and explained. It is shown that for melting of ice particles the simplified approach, which neglects the heat conduction in the solid and liquid parts in comparison to the latent heat, is valid.

A simple method is proposed which is able to describe the shape change during melting of a non-spherical particle. Using this model, the main phenomena associated with non-spherical particle melting (collection of the liquid in the mid-region of the particle, appearance of sharp cusps,

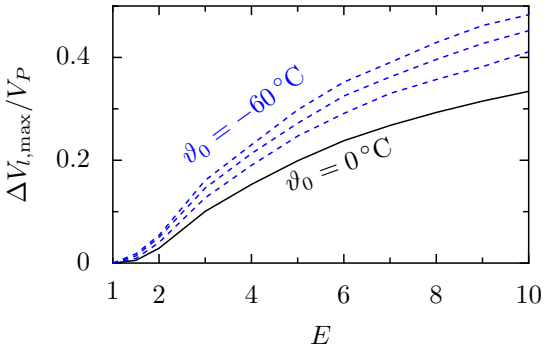

Figure 2.12: Maximum deviation of the particle's water content during melting between the sphere model and the model in the present study.

smoothing of the particle roughness) are reproduced and explained. Theoretically predicted melting times agree well with the experimental data. Moreover, the differences in the obtained results in terms of melting times and water content of the particle are discussed.

With the help of the presented model and the results a better understanding of the melting process of irregular particles is achieved. In particular the deviation in the results of particle melt ratio between data obtained by the spheroid model and by the commonly used 1D sphere model has an enormous effect on the accuracy of the icing prediction. As shown in Fig. 1.3, the icing severity is very sensitive to the melt ratio; already small changes can affect the icing significantly. Thus, taking into account the non-sphericity of the particle as done in the presented model, is essential for an accurate prognosis of icing under glaciated conditions.

3 Impact of small ice particles on a liquid film

ABSTRACT A numerical study of the water entry of non-rotating and rotating rigid spheres under varying impact angles and Weber numbers is presented. The numerical algorithm uses a Finite-Volume discretization and the interface between the liquid and the gaseous phase is described by means of a Volume-of-Fluid method. An appropriate mesh translation allows the boundary condition at the surface of the moving and rotating particle to be accounted for. The simulation results are validated with experiments and found to be in very good agreement both qualitatively (evolution of cavity shape) and quantitatively (motion of particle with respect to time). An investigation of the influence of particle rotation on its water entry behavior is carried out as well as an analysis of the effect of wettability upon cavity formation. Notably, wettability of the sphere plays a role during the penetration of a free liquid surface, even at higher Weber numbers.

During impact of small particles at low Weber numbers, the influence of capillary forces rises and the force emerging at the three phase contact line becomes predominant. This force is taken into account and its influence on the impact behavior is presented. It is shown that the interface penetration behavior, either water entry or escaping from water, mostly depends on the Weber number, the solid to liquid density ratio and the particle's wettability, while the impact angle has nearly no influence.

This chapter is based on the paper *On the influence of surface tension during the impact of particles on a liquid-gaseous interface* by Kintea et al. (2016a), published in Physics of Fluids. Also, it contains content from the conference paper *Oblique water entry of rigid spheres* presented by Kintea et al. (2014a) at the 26th Annual Conference on Liquid Atomization and Spray Systems in Bremen, Germany and the conference contribution *On particle impact on a free liquid surface at low Weber numbers* by Kintea et al. (2015c) presented at the 13th Triennial International Conference on Liquid Atomization and Spray Systems, Tainan, Taiwan.

Contents

3.1 Context

The impact behavior of ice particles determines whether they adhere to the component surface or rebound of it. Therefore, it crucially influences the accretion growth rate and thereby affects the icing severity. To improve the understanding and prediction capability, a numerical method is developed which is capable of predicting the trajectories of rotating spheres penetrating a free liquid surface, taking into consideration the force arising from the surface tension.

An accurate description of a flow induced by particle rotation is a very challenging task, since a proper velocity boundary condition on the surface of the sphere has to be implemented. Also, a model for the dynamic contact angle, depending on the local contact line velocity, is realized in the code to account for the particle's wettability. Furthermore, the surface tension force arising in the three phase contact line is considered. A comparison of the numerical prediction with existing experimental data exhibits very good agreement. Moreover, the influence of the contact angle

and the rotation on the cavity formation and body motion is investigated as well as the influence of the surface tension. One of the surprising results is that the wettability of the sphere plays an important role for the cavity dynamics, even if the Weber numbers are very high.

The impact behavior of small particles such as atmospheric ice crystals, i.e. interface penetration or sticking of the particle to it, is predicted by the code. By means of a dimensional analysis of the results, parameters of influence have been reduced to three dimensionless quantities. If ice crystal accretion is considered, two of the non-dimensional parameter are constant, leaving only the Weber number to determine whether a particle sticks to an interface or penetrates it. This potentially helps modeling the sticking efficiency which affects the growth rate of an ice accretion.

3.2 Theoretical background and numerical method

3.2.1 Governing equations in the liquid and gaseous phase

Since the impact process is mainly governed by the forces arising in the incompressible liquid phase and the particle travels at a velocity significantly lower than the speed of sound, the flow is considered to be incompressible. Therefore, the Navier-Stokes equation and the continuity equation for incompressible flow

$$\frac{\mathrm{D}\vec{u}}{\mathrm{D}t} = -\frac{1}{\rho}\nabla p + \nu\Delta\vec{u} + \vec{g} + \vec{f_\sigma}, \quad \frac{\mathrm{D}\rho}{\mathrm{D}t} = 0, \tag{3.1 a,b}$$

apply for the water and the air. Here the vector $\vec{u}$ represents the fluid's velocity field, ρ its density and p the pressure field. The kinematic viscosity is denoted by ν, t stands for time and $\vec{g}$ represents the gravitational acceleration.

Surface tension is smeared over a thin region near the liquid-gas interface. It is represented by a force per mass $\vec{f_\sigma}$, estimated using the Young-Laplace equation, as it is usually modeled in the framework of the Volume-of-Fluid method.

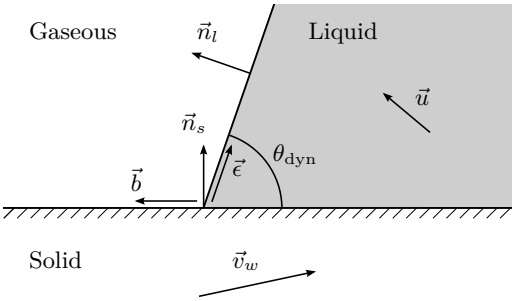

Figure 3.1: Slice normal to the three phase CL: Sketch of the geometry and kinematics near the CL. Definition of relevant velocities and vectors for the computation of the contact angle and the CL force.

3.2.2 Dynamic contact angle

The line, where the three phases (solid (s), liquid (l) and gaseous (g)) meet, is referred to as contact line (CL). Figure 3.1 shows a slice normal through that CL. The velocities $\vec{u}$ and $\vec{v}_w$ are the fluid and the wall velocity, respectively. The orientation is given by the unit normal vectors $\vec{n}_s$ on the wall surface and $\vec{n}_l$ on the interface between the liquid and the gaseous phase. The unit vector $\vec{b}$ is aligned normal to the CL and tangential to the wall, $\vec{\epsilon}$ points in direction of the gas/liquid interface.
The speed of the CL relative to the wall dictates the dynamic contact angle θ_{dyn} as described by Kistler (1993). This model yields a dynamic contact angle depending on the motion of the CL, which is described by the capillary number

$$\mathrm{Ca} = \frac{\nu_l \rho_l v_{\mathrm{CL,rel}}}{\sigma}, \tag{3.2}$$

where σ represents the liquid's surface tension and $v_{\mathrm{CL,rel}}$ is the value of the CL velocity relative to the wall. It is not identical with the material velocity at the contact line (Roisman et al., 2008) and is computed by

$$v_{\mathrm{CL,rel}} = \frac{(\vec{u} - v_{w,s}\vec{n}_l) \cdot \vec{n}_l}{\sqrt{1 - (\vec{n}_l \cdot \vec{n}_s)^2}} - v_{w,b}. \tag{3.3}$$

The velocities $v_{w,s}$ and $v_{w,b}$ are components of the wall velocity $\vec{v}_w$, normal to the wall surface and in the direction of $\vec{b}$, respectively. With the

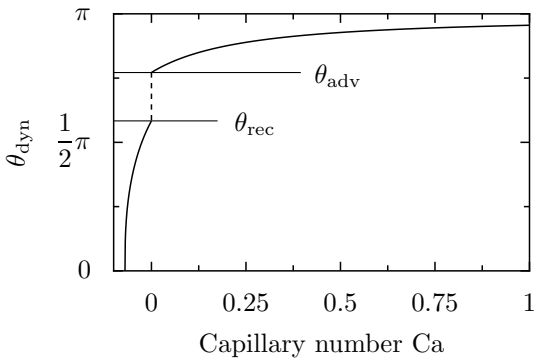

Figure 3.2: Dynamic contact angle in dependence of the Capillary number Ca with contact angle hysteresis, i.e. $\theta_{\mathrm{adv}} \neq \theta_{\mathrm{rec}}$.

knowledge of the capillary number the dynamic contact angle is computed as follows:

$$\theta_{\mathrm{dyn}} = \mathrm{f_H}(\mathrm{Ca} + \mathrm{f_H}^{-1}(\theta_0)), \tag{3.4}$$

where $\mathrm{f_H}(x)$ is the Hoffman function (Hoffman, 1975), which reads

$$\mathrm{f_H}(x) = \arccos\left\{1 - 2\tanh\left[5.16\left(\frac{x}{1+1.31x^{0.99}}\right)^{0.706}\right]\right\}. \tag{3.5}$$

The variable θ_0 in Eq. (3.4) takes different values depending on the direction of the CL motion. For positive values of Ca, i.e. for advancing CLs, it takes the value of θ_{adv}. When the CL recedes, this value becomes θ_{rec}. The result is a contact angle hysteresis between θ_{rec} and θ_{adv}. In this range of contact angles no CL movement is observed, as shown in Fig. (3.2). This plot shows the dynamic contact angle given by the Kistler model over the capillary number with contact angle hysteresis. For very small capillary numbers a cutoff of the angle has been made at 5°.

3.2.3 Motion of the solid particle

The particle motion is assumed as a superposition of translation and rotation of a perfectly rigid sphere. Its dynamics is determined by the axial momentum and the moment-of-momentum equations which take into account the forces and torques acting on the sphere from the two fluids (liquid and gas) and gravity. The forces and torques acting on the sphere from the fluids account for the surface tension, viscous and inertial effects.

From the numerically predicted instantaneous stress distribution on the particle surface of area A_P and the position of the contact line, the force $\vec{F}_P$ and torque $\vec{\tau}_P$ are calculated by numerical integration of following expressions

$$\vec{F}_P = \iint\limits_{A_P} -p\,\vec{n}_s + \nu\rho[(\nabla\vec{u}) + (\nabla\vec{u})^T] \cdot \vec{n}_s \; \mathrm{d}A + \int\limits_{\mathrm{CL}} \sigma\vec{\epsilon}\,\mathrm{d}l, \quad (3.6)$$

$$\vec{\tau}_P = \iint\limits_{A_P} \vec{r} \times \left(-p\,\vec{n}_s + \nu\rho[(\nabla\vec{u}) + (\nabla\vec{u})^T] \cdot \vec{n}_s\right) \mathrm{d}A + \int\limits_{\mathrm{CL}} \vec{r} \times \sigma\vec{\epsilon}\,\mathrm{d}l. \quad (3.7)$$

A unit normal vector $\vec{\epsilon}$ is introduced which points outwards of the solid in direction of the interface and normal to the CL. The first integral of Eqs. (3.6) and (3.7) correspond to viscous and pressure forces while the second integral represents the CL force $\vec{F}_\sigma$ arising at the contact line due to contact at the interface. The particle force and torque are subsequently used to compute the translational and rotary acceleration $\ddot{\vec{x}}_P$ and $\dot{\vec{\omega}}_P$ of the sphere according to

$$\ddot{\vec{x}}_P = \frac{\vec{F}_P}{m_P} + \vec{g}, \quad (3.8)$$

$$\dot{\vec{\omega}}_P = \vec{\tau}_P / \Omega_P, \quad (3.9)$$

where Ω_P is the sphere's mass moment of inertia. An integration of Eq. (3.8) and (3.9) yield the particle's speed and angular velocity. These quantities are used to compute the displacement and the surface velocity of the sphere.

3.2.4 Numerical method

Treatment of phases and interfaces The computational domain consists of three distinct phases: the liquid water, the gaseous air and the solid sphere. It is spatially discretized by means of finite volumes with the open source software OpenFOAM. The interface between liquid and the gaseous phase is accounted for using the Volume-of-Fluid method as described by Hirt and Nichols (1981). This method is characterized by defining a scalar function α for the whole domain, which takes values between zero and one. Its value represents the volume fraction of each cell which is occupied by the liquid phase.

The solid particle is not part of the discretized domain, but it constitutes a boundary on it. It is moved by means of a mesh motion, where the translating mesh follows the particle motion. In the scope of this mesh movement, only the particle and the fine mesh around it is moved. The coarser areas far from the particle are stretched and compressed to allow the particle's motion, while the outer mesh boundaries remain stationary.

Velocity boundary condition on the particle All the equations are solved for in the laboratory system. Consideration of the particle movement is completed by applying a velocity boundary condition on the surface of the sphere. This velocity is composed of two components, the velocity resulting from the translational movement and the velocity due to the rotation. The translational component $\vec{v}_T$ is equal to the particle speed $\vec{U}$ on the entire surface and is therefore known. Superimposed on this velocity, the rotational component reads

$$\vec{v}_R = (\omega\, \vec{a}) \times \vec{r}, \tag{3.10}$$

where the vector $\vec{r}$ is the vector from the sphere center to the considered position on the particle surface and $\vec{a}$ is the unit axis of rotation. The angular velocity is denoted by ω.

Solving Eqs. (3.1 a,b) using the boundary conditions for velocity and contact angle to account for the particle, yields the velocity and pressure in the liquid and the gaseous phase. From those fields viscous and pressure forces and the torques arising from them acting on the particle are computed by means the first integral of Eqs. (3.6) and (3.7).

Estimation of capillary force The last terms in Eqs. (3.6) and (3.7) cannot be directly implemented in a Volume-of-Fluid representation of the interface, since the position of the interface is not known. On the other hand, this method provides a convenient way to smear also the capillary force $\vec{F}_\sigma$ arising at the interface and the torque $\vec{\tau}_\sigma$ it generates. In the presented algorithm, it is evaluated by integrating the magnitude of the surface gradient of the liquid volume fraction $|\nabla_s \alpha|$, multiplied with the surface tension and the unit interface direction vector $\vec{\epsilon}$ over the entire surface area A_P of the particle

$$\vec{F}_\sigma = \int_{\mathrm{CL}} \sigma \vec{\epsilon}\, \mathrm{d}l = \iint_{A_P} |\nabla_s \alpha| \sigma \vec{\epsilon}\, \mathrm{d}A. \tag{3.11}$$

The torque caused by this force (second integral of Eq. (3.7)) is then described by

$$\vec{\tau}_\sigma = \int_{\mathrm{CL}} \vec{r} \times \sigma \vec{\epsilon}\, \mathrm{d}l = \iint_{A_P} \vec{r} \times |\nabla_s \alpha| \sigma \vec{\epsilon}\, \mathrm{d}A. \tag{3.12}$$

These equations describe the smearing of the CL force over the diffuse interface in the same fashion as the interface itself. Using them yields the force vector for the diffused interface correctly in the integral sense.

These quantities are finally used to calculate the particle movement; hence the mesh motion, as well as the boundary conditions on the particle surface.

Computational mesh The choice of the mesh depends on the symmetry of the problem. For the computation of the axisymmetric water entry of a non-rotating sphere a two-dimensional mesh is employed. A three-dimensional grid, which represents half of the sphere and the liquid pool, is used for the simulation of the rotating particles. More details on the mesh can be found in the corresponding sections. Figure 3.3 shows a sketch of a slice of the 3D mesh and its local refinement before (gray lines) and after the movement of the particle (black lines). Locally refined areas are shown as gray surfaces in which no motion of grid points relative to each other occurs, the mesh in these areas remains unchanged. The shading of the surface represents the local mesh refinement: The darker the shading, the finer the mesh in that area. Particle movement is realized by stretching and compressing the mesh in the white region.

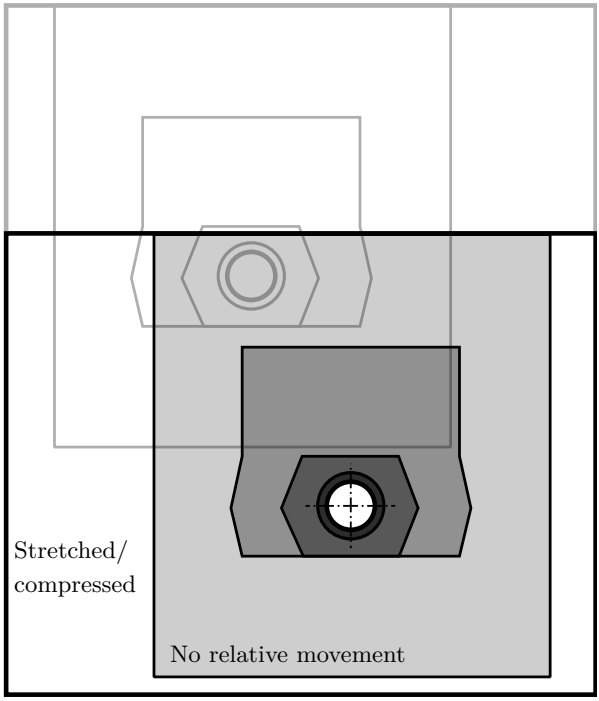

Figure 3.3: Organization of the mesh and its local refinement. Gray lines correspond to the mesh before movement while black lines represent the mesh altered to account for the particle movement. Refined areas, shown as gray surfaces, are moved but not distorted while the white area is compressed and stretched.

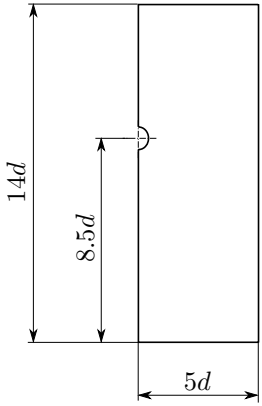

(a) Sketch of the two-dimensional domain used for the computation of axisymmetric impacts without rotation or inclination.

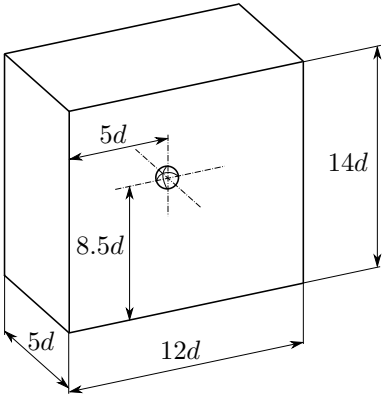

(b) Dimensions of the 3D-mesh which utilizes one symmetry plane which enables accounting for particle revolution with an axis of rotation perpendicular to it and impact inclination in that plane.

Figure 3.4: Computational domains.

3.3 Results and Discussion

Normal impacts of non-rotating and rotating spheres are presented and the results are compared to available experimental data. Note that the focus of this study lies on the behavior of the particle motion and cavity formation, less on the corona formation, which takes place above the initial undisturbed water surface. For this a more refined mesh on the surface of the water pool would be necessary. An investigation of the corona formation and propagation of such a corona is highly complicated. Experimental, analytical and numerical investigations of that corona have already been presented by Thoroddsen (2002), Roisman and Tropea (2002) and Josserand and Zaleski (2003), respectively.

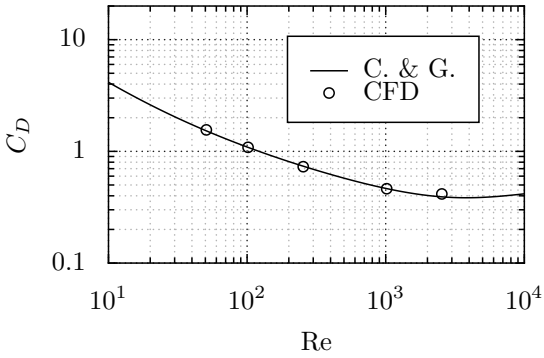

Figure 3.5: Drag of a sphere in steady-state inflow conditions over Re. The circles denote results from this study, the solid line corresponds to the fit of Clift and Gauvin (1970).

3.3.1 Verification for single phase flows

In order to verify the numerical algorithm a computation of the drag of a non-rotating sphere and the lift-force of a rotating sphere in a steady-state single phase incident flow at an incident velocity u_∞ has been performed. Figure 3.5 shows the numerically obtained values of the drag coefficient C_D as circles and compares them to the fit of Clift and Gauvin (1970). They are in very good agreement, especially for $\mathrm{Re} \leq 10^3$. At higher Reynolds numbers the boundary layer becomes increasingly turbulent. This is not covered by the code, which does not include a turbulence model. Figure 3.6 shows the lift coefficient C_L divided by the dimensionless rotational velocity $\omega^* = \omega d/(2u_\infty)$ over the Reynolds number. Numerical results are denoted as filled circles for different angular velocities ω^*. Hollow symbols represent experimental results from Barkla and Auchterlonie (1971) and Tsuji et al. (1985). The numerical values compare well with the experiments. Therefore, the code is considered verified for single phase flow around a sphere, either without or with rotation.

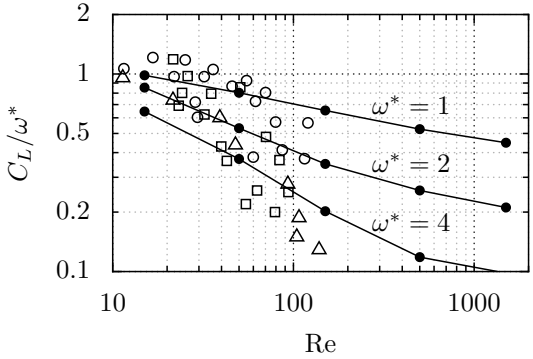

Figure 3.6: Lift of a rotating sphere in a stationary flow in dependence of Re. Results obtained by means of the numerical algorithm are plotted as filled circles, whereas the hollow symbols represent experimental results (Barkla and Auchterlonie, 1971, Tsuji et al., 1985): (◯) $1 < \omega^* < 2$, (□) $2 < \omega^* < 4$, (△) $\omega^* > 4$.

3.3.2 Normal impact of a non-rotating sphere

When a large, rigid body impacts normally onto a liquid pool its motion is governed mainly by the inertial and viscous forces applied to it from the liquid. The liquid flow separates from the body surface at the CL which leads to the formation of a crater. Moreover, when the impact velocity is high the impact leads to the creation of an uprising above the pool surface liquid sheet, which is similar to the corona generated by drop impact. The thickness of the liquid sheet in the corona is much smaller than the sphere diameter. It is comparable with the viscous length scale $\sqrt{\nu t}$. Moreover, the corona is bounded by an unstable rim formed by capillary forces (Taylor, 1959). Computation of the flow in the corona and its breakup, leading to splash is a rather challenging problem requiring an extremely fine mesh. This is out of scope of the present work, since the main interest of the present study is focused on the description of the body penetration and of the details of crater formation. In this section we consider the normal impact of a rigid spherical body into a semi-infinite liquid pool. In order to investigate the effect of the body density, spheres of various materials have been selected as in the experiments of Aristoff et al. (2010). The normal impact of non-rotating spherical bodies of Polypropylene (PP), Nylon (PA) and Teflon (PTFE) of a diameter of

$d = 0.0254$ m is investigated. They hit the free water surface at a velocity of 2.17 m/s; the density ratio for each material is shown in Fig. 3.7. With a surface tension of $\sigma = 0.073$ N/m, this leads to relatively high Weber numbers $\mathrm{We} = \rho_s U_0^2 d/\sigma > 1000$, indicating only little influence of the surface tension. Therefore, the contact angle in the numerical simulation is assumed to be constant and to have a value of 120° as observed in the experiments. By utilizing the rotational symmetry of the problem a two-dimensional mesh is employed. It consists of 200,000 cells with a local mesh refinement in proximity of the particle leading to 720 cells along the circumference. The dimensions of the computational domain for this case are shown in Fig. 3.4 (a). The interface between the water and the air in the numerical results is said to be at $\alpha = 0.5$. The simulation matches the experimental results very well for the cavity below the initial water surface, i.e. $z = 0$.

Figure 3.8 shows the penetration depth of the sphere center over the time in dimensionless form. The dashed line represents the experimental results, whereas the solid lines correspond to results obtained by means of the simulation. Numerical and experimental depth and time of the cavity pinch-off are marked by crosses and circles, respectively. Both, the trajectory and the pinch-off are in very good agreement with the experiments. The maximum relative deviation for each case values 1.6 % (PP), 3.1 % (PA) and 3.8 % (PTFE). Thus, the numerical method is validated for multiphase flows.

Figure 3.9 shows the velocity of the PP sphere over time. The maximum deceleration; hence the largest structural loads, take place during the initial slamming stage as predicted by Shiffman and Spencer (1945). This phase is followed by the motion of the sphere through the fluid with a trailing cavity. During this phase the drag is approximately constant for the cases investigated in this study. Eventually the pinch-off occurs, which completes the second stage and initiates the final stage of the water entry.

3.3.3 Effect of particle rotation on water entry

Rotation of the sphere leads to the generation of a thin viscous boundary layer near the body surface. The velocity gradients corresponding to body rotation lead to the appearance of strong tangential stresses. The transverse force applied to the rotating body leads to the deviation of the trajectory from the initial normal direction. The problem is no longer

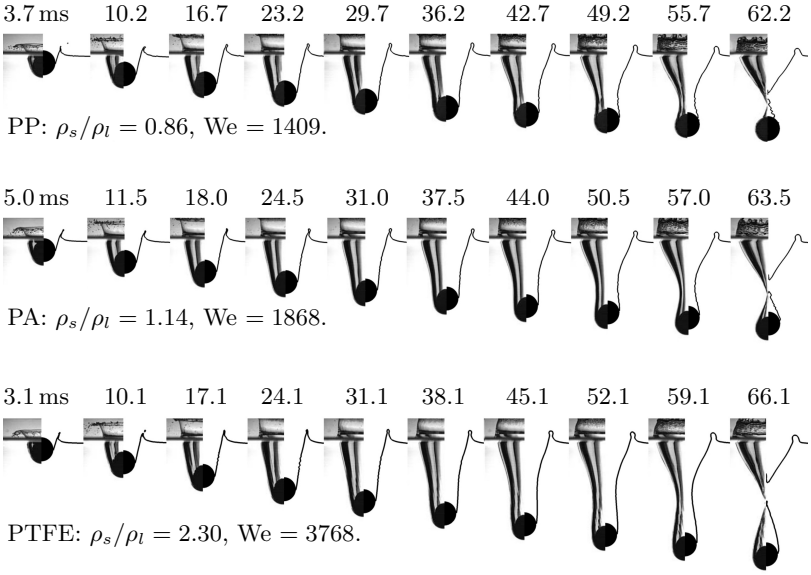

Figure 3.7: Comparison of the evolution of cavity shapes between experimental results (Aristoff et al., 2010) (left) and numerical solution of this study (right) at the same time after sphere center passes the water surface. The spheres impinge on the water surface without rotation at a velocity of $U_0 = 2.17$ m/s. A constant contact angle of 120° is employed in the numerical computation. Adapted with permission from Phys. Fluids 22, Aristoff et al., "The water entry of decelerating spheres", 032102. Copyright 2010, AIP Publishing LLC.

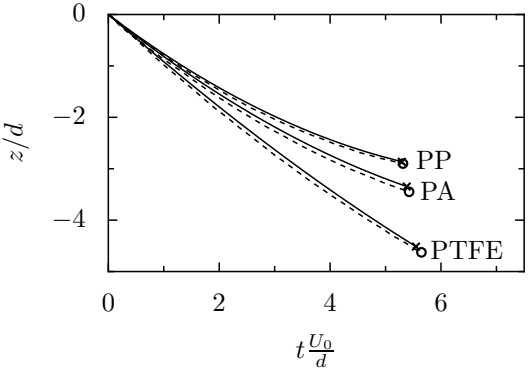

Figure 3.8: Comparison between experiments (Aristoff et al., 2010) and computations: Depth of the sphere center with respect to the free liquid surface. Symbols denote time and position of the cavity pinch-off.

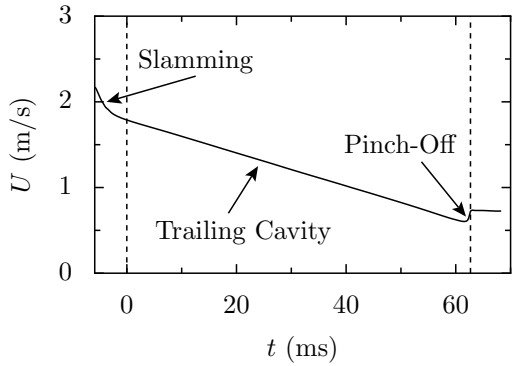

Figure 3.9: Computed velocity of the Polypropylene sphere during water entry. The three stages of water entry are shown.

axisymmetric and thus has to be treated by a 3D code. To accurately describe the body rotation an additional length scale has to be considered in the solution. This scale is based on a typical thickness of the boundary layer associated with rotation $l_{\mathrm{BL}} = 2\nu/(\omega d)$. The required mesh size has to be much smaller than l_{BL}. A three-dimensional mesh is set up with 1.36 million cells and 480 cells along the sphere's circumference. This

mesh utilizes one symmetry plane which is normal to the axis of rotation. Figure 3.4 (b) shows the size of the computational domain. The number of the cells is chosen after several convergence tests and optimized to the used operational conditions.

The spheres of the two computed cases of normal impact with rotation correspond to the experiments by Techet and Truscott (2011) and are of the same density ratio $\rho_s/\rho_l = 1.74$ and diameter $d = 0.0572$ m. Both of them have the same impact velocity as in the experiments, which results from dropping the spheres from a height of 36 cm. Hence, they hit the water surface at a velocity of 2.56 m/s which corresponds to a Weber number of 8935. In one of the cases a cavity is formed (I-r) while no cavity formation is observed in the other case (II-r). The two cases differ from each other in rotational velocity and surface treatment. The sphere in case I-r rotates initially at $\omega_0 = 210$ rad/s and has a static contact angle of $\theta_{\mathrm{st}} = 122°$, whereas the sphere in case II-r has a spin of $\omega_0 = 99$ rad/s and a static contact angle of $\theta_{\mathrm{st}} = 68°$.

A comparison of the numerically obtained cavity shapes and the experimental cavity of case I-r is shown in Fig. 3.10. The images have the same scale. The cavity shapes compare very well with the experimentally observed ones. A slight deviation is observable in the last two pictures. This is because the pinch-off occurs slightly earlier in the simulation, resulting in an already collapsed cavity at the pinch-off time of the experiment, which is shown in the last image. This is presumably due to the fact, that the numerical lattice is coarsened remote from the sphere, where the pinch-off occurs. Interfacial features close to the particle which govern the drag, are recovered very well. Especially the water jet on top of the sphere, which is dragged by the no-slip condition of the rotating sphere and impinges on the other side of the cavity thereby deforming it, emerges in the experiment as well as in the simulation. Figure 3.11 shows the impact of case II-r experimentally and numerically. No cavity emerges in that case. This outcome is in agreement with the findings of Duez et al. (2007), demonstrating the existence of a critical contact angle for cavity formation. Interfacial phenomena close to the sphere, i.e. within the fine area of the grid, are recovered well. The second stage of water entry as described by Shiffman and Spencer (1945) is not present since no cavity develops. Therefore, the initial slamming stage is directly followed by the single phase drag stage.

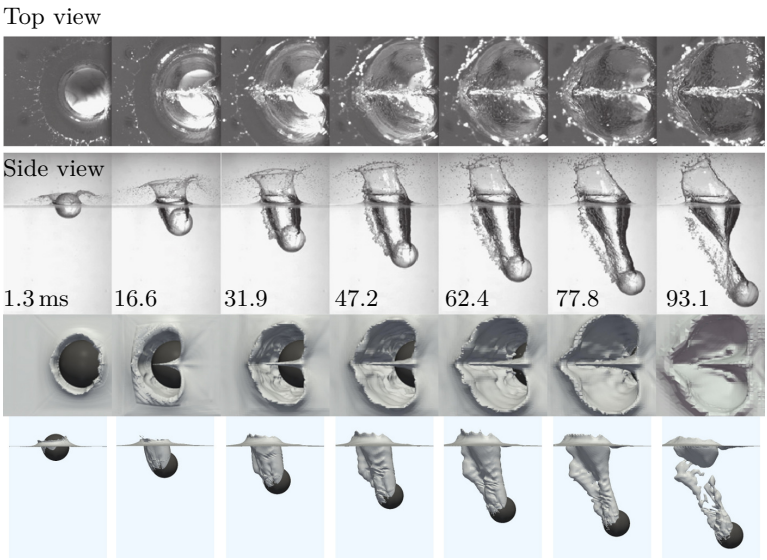

Figure 3.10: Cavity shape comparison between experiment (top) and numerical results (bottom) at different times for case I-r ($\rho_s/\rho_l = 1.74$, $U_0 = 2.56$ m/s, $\omega_0 = 210$ rad/s, We = 8935). A dynamic contact angle is computed at the sphere surface assuming $\theta_{\text{adv}} = \theta_{\text{rec}} = \theta_{\text{st}} = 122°$. Experimental results reprinted from Journal of Fluids and Structures, 27, A.H. Techet, T.T. Truscott, "Water entry of spinning hydrophobic and hydrophilic spheres", 716–726, Copyright (2011), with permission from Elsevier.

Despite the high Weber number of the impacts, the computation of the rotating sphere cases based on a constant contact angle assumption led to a deviation of the trajectories from the experimental ones, which increased with time. Due to the sphere rotation, the relative contact line movement is enhanced and switches from advancing to receding depending on which side of the sphere one looks at. This results in increased capillary numbers with varying signs which influences the contact angle significantly. In our computations, Kistler's dynamic contact angle model has been employed; as described in section 3.2. Figure 3.12 shows the results obtained by means of the numerical algorithm and compares them to the experimental results. The solid lines represent the numerically obtained trajectories of

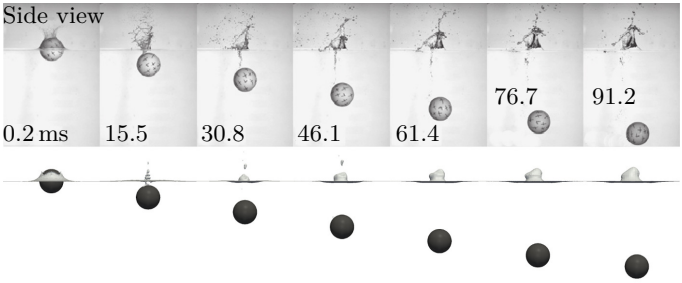

Figure 3.11: Comparison of experimental data with numerical results: Side view of the impact of case II-r ($\rho_s/\rho_l = 1.74$, $U_0 = 2.56$ m/s, $\omega_0 = 99$ rad/s, We = 8935). The dynamic contact angle at the sphere surface is computed assuming $\theta_{\mathrm{adv}} = \theta_{\mathrm{rec}} = \theta_{\mathrm{st}} = 68°$. No cavity emerges. Experimental results reprinted from Journal of Fluids and Structures, 27, A.H. Techet, T.T. Truscott, "Water entry of spinning hydrophobic and hydrophilic spheres", 716–726, Copyright (2011), with permission from Elsevier.

the sphere center assuming $\theta_{\mathrm{adv}} = \theta_{\mathrm{rec}} = \theta_{\mathrm{st}}$; the squares on these lines are 25 ms apart. Experimental results are shown as circles, the initially undisturbed free liquid surface resides at $z = 0$. The agreement between numerical and experimental results is very good for both cases. Note that those cases are also shown and compared to a computation assuming single phase force coefficients in Figs. 1.6 and 1.7.

Figure 3.13 shows the rotational velocity of the spheres. In both cases, it remains nearly constant. An approximately constant deceleration makes them lose less than 5 % of their revolution speed during the water entry. This deceleration is due to viscous forces acting tangential on the sphere surface. These forces scale with the fluid's dynamic viscosity, which is significantly higher in water than in air. Hence, the deceleration is greater for cases in which no cavity emerges and therefore more of the sphere's surface is surrounded by the more viscous water.

Duez et al. (2007) have shown that for a given impact velocity a critical contact angle exists below which no cavity emerges. A variation of the contact angle parameters θ_{rec} and θ_{adv} in a range which does not cross the limit of cavity-formation, neither an influence on the cavity shape nor

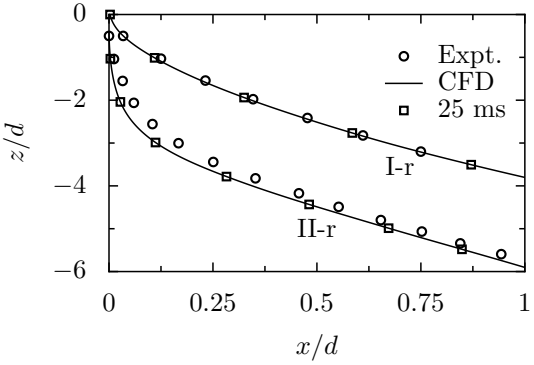

Figure 3.12: Experimental sphere trajectory (circles) by Techet and Truscott (2011) compared to case I-r and II-r of this study (solid line). Squares mark 25 ms intervals on the trajectory.

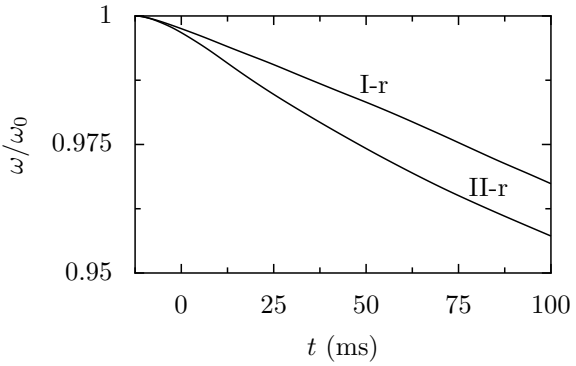

Figure 3.13: Rotational velocity of the spheres during the first 100 ms of the water entry. At $t < 0$, the sphere center is above the liquid surface, but the sphere surface already touches the liquid, which explains the deceleration before $t = 0$.

on the trajectory is observed.

Table 3.1: Impact data for the inclined impact cases I-i, II-i, III-i, IV-i and V-i.

	I-i	II-i	III-i	IV-i	V-i
Ξ (°)	62.4	51.8	35.0	39.4	31.6
U_0 (m/s)	2.1	3.4	2.47	4.39	4.83
ω_0 (rad/s)	174.5	273.2	196.3	0	0
ρ_s (kg/m^3)	860	860	860	860	1140

3.3.4 Inclined particle impact

If a sphere penetrates a liquid water surface under an impact angle Ξ at an initial velocity U_0, it starts to rotate due to the eccentric forces acting on the sphere resulting in an appearance of a torque. Therefore, accounting for the particle rotation is of crucial importance for the accurate computation of the oblique water entry of spherical bodies. Table 3.1 gives an overview over the presented computations and experiments of spheres of a diameter of $d = 20$ mm penetrating a liquid water surface under a certain angle. The experiments were performed by T. Hauk at Airbus Group Innovations. The cases I-i, II-i and III-i correspond to the initial rotation of a sphere before impact. In these experiments a rail has been employed on which the spheres rolled down a slope and thereby accelerated to the desired velocity. For the non-rotating cases a shooting device was used which allowed accelerating the particles without rotation.

Figure 3.14 shows the emerging trailing cavity of case II-i at certain times after the sphere center penetrates the initially undisturbed water surface. The shape of the cavity is in good agreement with the experimental observations, while the corona deviates from experiments which is due to the mesh coarsening far from the sphere. Figure 3.15 shows the trajectories of the sphere centers in comparison with experimentally obtained data. Numerical results are shown as solid lines while the experimental data are plotted as crosses. All of the trajectories are in very good agreement with experimentally obtained results which proves the code's ability to compute the particle's behavior during water entry correctly. The deflection of the particles from a straight line is due to gravity and particle rotation. Even the non-rotating particles start to spin upon impact resulting in a non-symmetrical flow field around the

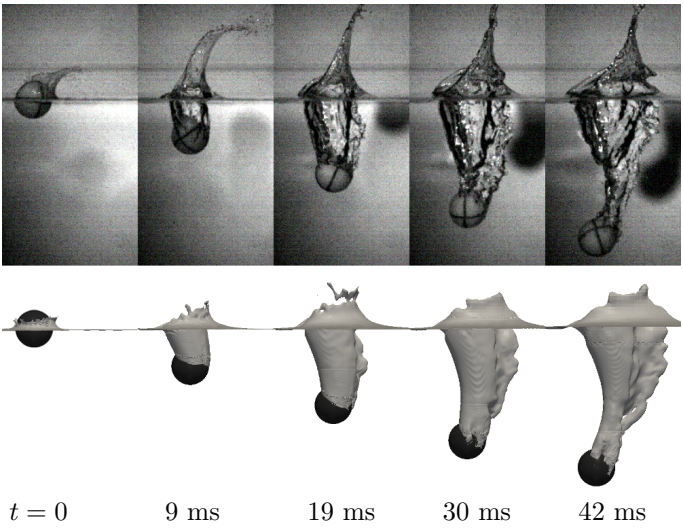

Figure 3.14: Emerging cavity during water entry of case II-i at various time steps. Comparison between experimental results (top) and numerically obtained cavity shape (bottom).

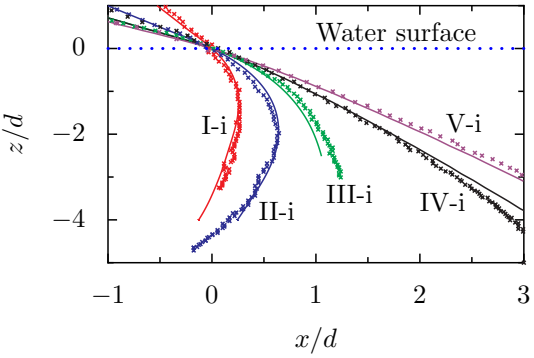

Figure 3.15: Trajectories of spheres impacting a liquid surface at different angles and angular velocities.

sphere causing the deflection.

3.3.5 Influence of the Weber number on the impact behavior of small particles

All of the previously investigated impacts exhibit rather high Weber numbers far beyond 1000. This section focuses on the impact of spherical bodies on a liquid-gaseous interface at low particle Weber numbers of less than 100 and small Bond numbers $\mathrm{Bo} = \rho_l g d^2/(4\sigma)$ (Aristoff and Bush, 2009). Figure 3.16 shows a particle impact at $\mathrm{We} = 27.5$ on the left in comparison with an impact at $\mathrm{We} = 1868$ at the same non-dimensional times $t^* = t\,U_0/d$. It is evident that at low Weber numbers, the influence of the surface tension becomes predominant and strong interface curvatures are quickly smoothed. Also, the particle's deceleration as it hits the water surface is greater at lower We, since the influence of the CL force rises. Since the expected capillary numbers are rather small and no rotation-induced switch between advancing and receding CL movement occurs, a constant contact angle boundary condition is sufficient for the computation of the impact of the small particles.

A validation of the code is performed using the experimental results from Lee and Kim (2008) for the impact at low We numbers. Figures 3.17 and 3.18 show the trajectories of the sphere center with respect to time for two different cases (sinking and bouncing) with (solid line) and without CL force (dashed line) in comparison with experimental data, shown as circles. Both plots are non-dimensionalized with sphere diameter d as length scale and the time scale U_0/d. Without considering the CL force, the trajectory deviates significantly from the experimental data and both spheres penetrate the liquid-gaseous interface, while one of the particles (Fig. 3.18) is captured by the surface tension of the interface. Including the CL force improves the agreement between numerical results and experimental data significantly and the impact behavior, i.e. sticking at the interface or penetration of it, is captured correctly. Thus, the capillary force plays a dominant role for low We number impacts.

From Figure 3.16, 3.17 and 3.18, it is clear that at low We numbers less than approximately 100, the capillary forces dominate the water entry process. When maintaining a low Bond number, which is assumed in this work, gravity only becomes important at cavity pinch-off depths larger than $2l_c^2/d$, where l_c is the capillary length (Aristoff and Bush, 2009). In the scope of the following parameter study, mostly results are considered where no pinch-off occurs and the particle is captured by the interface. In the few considered cases in which the particle penetrates the interface and

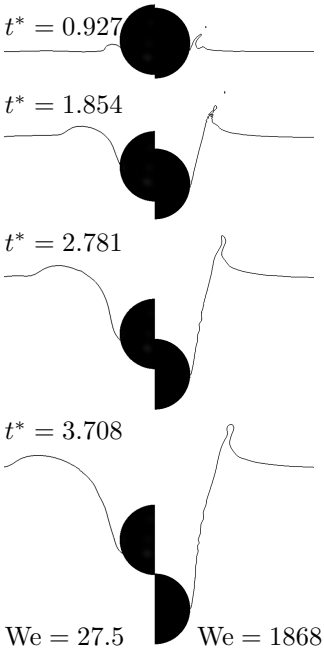

Figure 3.16: Comparison between the cavity shape of an impact at a low Weber number of 27.5 with the water entry at We = 1868 at the same dimensionless times $t^* = tU_0/d$. Both particles have a hydrophobic surface with a constant contact angle of 154°.

a collapse of the cavity emerges, the penetration distance at which this happens is far below the capillary length. Therefore, gravity is neglected for this study.

At first, a hydrophobic sphere is considered. Below a critical We number which depends on density ratio and wettability, the particle is not able to penetrate the liquid-gaseous interface and the particle gets either captured by the interface or rebounds. In such a case, the particle reaches a maximum penetration depth $z_{\max}$, after which the direction of the particle's motion is reversed as shown in the Figure 3.18. The maximum non-dimensional penetration depth $z_{\max}/d$ depends only on

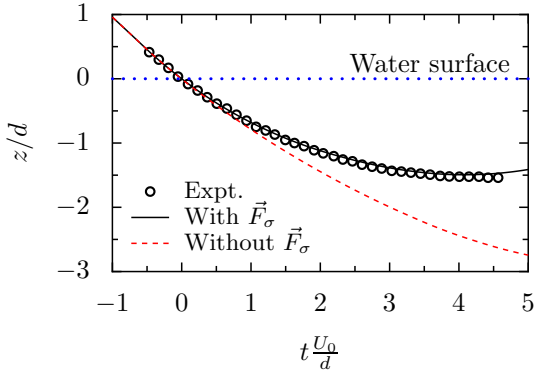

Figure 3.17: Vertical position of the center of a sinking sphere ($\rho_s = 1990$ kg/m^3, $U_0 = 0.73$ m/s, $d = 1.74$ mm). A constant contact angle of 154° is used for the computation. We = 25.3.

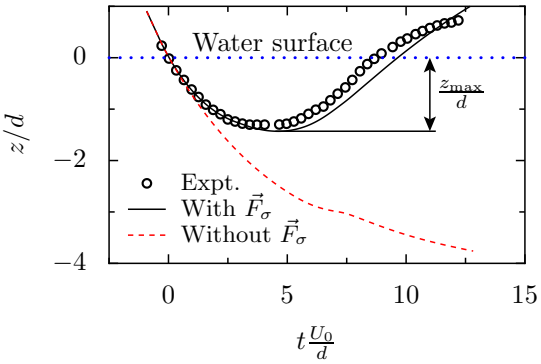

Figure 3.18: Vertical position of the center of a bouncing sphere ($\rho_s = 1320$ kg/m^3, $U_0 = 0.89$ m/s, $d = 1.92$ mm). A constant contact angle of 154° is used for the computation. We = 27.5.

the Weber number, the solid to liquid density ratio ρ_s/ρ_l and the contact angle θ.

Figure 3.19 shows the non-dimensional maximum penetration depth for a density ratio of 0.5, 1 and 2 in a We number range of 0 – 60 for

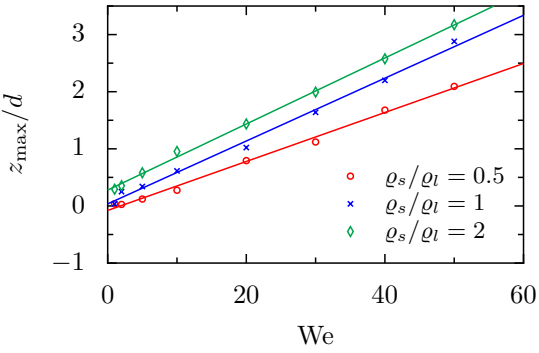

Figure 3.19: Maximum penetration depth over the Weber number at a constant contact angle of $\theta = 154°$ for a normal impact. The different symbols correspond to numerical results of different density ratios and the corresponding solid lines represent a linear fit through these points.

a contact angle of $\theta = 154°$. The symbols denote numerical results of different density ratios while the corresponding solid line is a linear fit through these data points. For a fixed density ratio, these points are aligned on a straight line indicating that $z_{\max}/d \sim \mathrm{We}$ in the investigated range of We. An inclination of the particle impact has nearly no effect on the maximum penetration depth in the considered Weber number range if We is computed with the normal component of the impact velocity.

Penetration of a solid body into a liquid is often described using the Poncelet approximation (Poncelet, 1829). The equation of motion of a solid particle is assumed in the following form

$$-\rho_s d^3 \frac{\mathrm{d}U}{\mathrm{d}t} = \phi_a d^2 \rho_l U^2 + \sigma d \phi_b, \tag{3.13}$$

where ϕ_a and ϕ_b are constants. The first term in the right hand side of (3.13) is associated with the inertial effects of the flow, generated by the particle impact, and the second term in our case is associated with surface tension. The solution of (3.13) yields the well-known expression for the penetration depth

$$\frac{z_{\max}}{d} = \frac{\rho_s}{2\rho_l \phi_a} \ln\left[1 + \frac{\phi_a \rho_l \mathrm{We}}{\phi_b \rho_s}\right]. \tag{3.14}$$

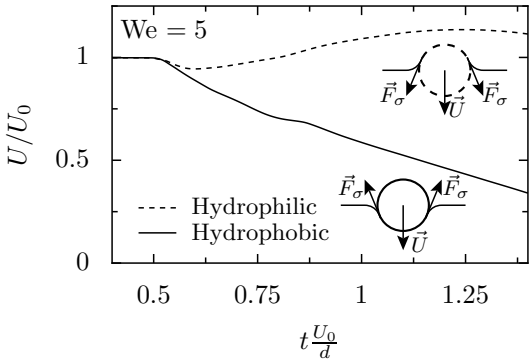

Figure 3.20: Influence of the wettability on velocity during interface penetration. The hydrophilic sphere with a contact angle of $\theta = 26° = \text{const.}$ is accelerated during the impact while a hydrophobic sphere ($\theta = 154°$) is decelerated by the CL force.

For small values of $(\phi_a \rho_l \mathrm{We})/(\phi_b \rho_s)$ the expression for the penetration depth can be simplified

$$\frac{z_{\max}}{d} \sim \frac{\mathrm{We}}{2\phi_b}. \tag{3.15}$$

The linear dependence of the penetration depth on the Weber number, predicted by the Poncelet equation, is confirmed by the results shown in Fig. 3.19.

So far only the low Weber impact of hydrophobic bodies has been considered. For such particles the liquid-gaseous interface is aligned in a way that the CL force acts in the counter-direction of the particle movement, i.e. it decelerates the sphere. A hydrophilic surface leads to a CL force which acts in direction of the velocity during interface penetration. Figure 3.20 shows the non-dimensional velocity over time of a spherical body penetrating a free liquid surface at We = 5. For the hydrophobic sphere ($\theta = 154°$), the CL force decelerates the particle until it eventually reverses its moving direction leading to a maximum penetration depth as explained previously. The hydrophilic sphere surface with a contact angle of 26° results in an acceleration of the particle upon impact.

It is noteworthy that this situation is reversed for a particle leaving

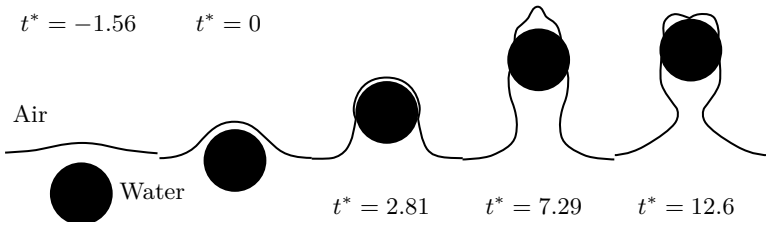

Figure 3.21: Formation of a liquid bridge upon impact of a hydrophilic particle ($\theta = 26° = \text{const.}$) on a liquid gaseous interface coming from the liquid, We = 50.

water and entering air. In this case, the hydrophilic particle is decelerated and therefore hindered from exiting, while the hydrophobic particle is accelerated. When a hydrophilic particle is exiting the water, a liquid bridge forms which connects the water with the particle and behaves similar to an emerging cavity for water entry. Figure 3.21 shows a particle impacting on the liquid-gaseous interface at a Weber number of 50 at which it is not able to penetrate it, but sticks to the interface. After the particle center passes the initial water surface, a liquid bridge forms which connects the exiting particle with the liquid pool and drags the particle towards the water. At $t^* = 12.6$, the particle movement is already reversed, i.e. it moves towards the water.

Above a critical Weber number $\text{We}_{\text{crit}} \approx 60$ (for a density ratio of one and a contact angle of 26°), the liquid bridge collapses and the particle is able to escape from the water without being dragged back to it. This process is analogous to the cavity collapse during water entry. The maximum escaping distance of the particle also depends linearly on the Weber number and is not influenced by the inclination angle. Characteristic for the the water escape process is the interface deformation well before the the particle touches it, in Fig. 3.21 at $t^* = -1.56$, which significantly decelerates the particle already before the impact. To account for this fact in the numerical computations, the particle started its movement towards the interface at $z = -1.5d$. At low Weber numbers, however, the particle center was not able to pass the water line at $z = 0$ owing to the increased drag in the water and the drag caused by the interface deformation which is mainly a result of surface tension.

3.4 Conclusions

In this study the impact of a rigid sphere on a free liquid surface is considered. In all the cases the simulation matches very well with the experiments both qualitatively and quantitatively.

For a non-rotating particle a constant contact angle boundary condition on the particle surface is sufficient. If the sphere rotates, this assumption yields an increasing deviation between experiments and simulations. The application of the dynamic contact angle model leads to significantly better results. Thus, wettability plays a role in the process of cavity formation, even at higher Weber numbers as confirmed by experiments. Hence, the implementation of a dynamic contact angle model in the code is a necessary condition for an accurate prediction. Yet, the choice of θ_{rec} and θ_{adv} has no significant influence on the results as long as the limit of cavity-formation is not crossed and the magnitude of the capillary number is high enough. During the impact process the sphere's rotational velocity remains nearly constant.

It has been shown that the penetration behavior at low Weber numbers of a liquid-gaseous interface mostly depends on the Weber number We, the ratio of particle to liquid density and the contact angle of the liquid on the particle's surface. The same tendencies were observed when considering the escape of a solid particle from a liquid when switching from hydrophobic to hydrophilic surface.

If ice crystal accretion is considered, the penetration of an air/water interface by a solid ice particle is regarded. Therefore, the density ratio and the contact angle become invariant leaving only the Weber number as parameter determining whether the particles breaches the interface or is captured by it. Since ice is hydrophilic, spherical particles will always be able to enter the liquid phase while they are hindered from leaving it. If the Weber number of the escaping particle is below a certain threshold value, it will stick to the interface coming to rest eventually. This escaping Weber number is usually smaller than the impact Weber number as the particle is decelerated by drag forces in the fluid and upon impact on the solid substrate under the liquid film which also can result in particle fragmentation. Both processes decrease the Weber number by reducing the velocity and the particle diameter. Thus, if the impact Weber number is below the threshold value for the escape, the particle is very likely to be captured by the liquid film.

The numerical model is developed for Newtonian fluids and yields insight into physical processes governing the sticking of wet particles. In addition, the approach can be used to compute the particle impact on a wet granular ice accretion, a dense suspension, by modeling it as a rheological complex fluid onto which the particle impinges.

PART TWO:
Accretion and shedding of an ice crystal accumulation

In this part, transport phenomena in ice layers consisting of many ice particles, liquid water and entrapped air are considered. Thermal properties and melting behavior of the layer influences the composition and therefore the hardness of the accretion. Both properties significantly influence the connection strength of the accretion to the surface and the potential damage it may cause to the engine upon shedding and impacting on downstream components.
Two different approaches are used to investigate the transport processes taking place in a melting porous structure. In a first approach, presented in chapter 4, single particles of the accretion are resolved in the numerical mesh. With its help, the behavior of porous ice layers is studied. The obtained knowledge is utilized in the second approach to model the effective thermal properties of the ice accretion and its melting behavior, described in chapter 5. It enables an effective computation of accretion and shedding of ice layers by predicting its composition throughout the accretion.

4 Accretion and shedding of a porous ice/water accumulation: *Detailed numerical model*

ABSTRACT Under certain conditions a porous ice/water layer builds up on hot surfaces in aircraft engines or on heated probes and eventually leads to their malfunction. In this chapter a detailed numerical algorithm for the computation of heat and mass fluxes within and over the system boundaries of such a porous ice/water layer is presented. The code predicts the amount of liquid in the porous layer, which potentially can help to model ice shedding. This solver accounts for phase transitions between the solid, liquid and gaseous state as well as for the heat fluxes in the substrate on which the ice accretes and in the porous ice/water layer. Numerically predicted results show excellent agreement with available data in all the test cases. Existing accretion experiments are reproduced well by means of the code and yield insight into the governing physical processes. Finally, an analysis of parameters of high influence on the accretion reveals limits for icing.

This chapter is based on the conference paper *Numerical investigation of ice particle accretion on heated surfaces with application to aircraft engines* by Kintea et al. (2014b) which has been presented at the 11th AIAA/ASME Joint Thermophysics and Heat Transfer Conference in Atlanta, USA.

Contents

4.1 Context

Growth and shedding of the ice layer are determined by the impact behavior of the crystals and its composition, which strongly depends on heat and mass fluxes taking place within. The composition of the ice layer influences the sticking efficiency of impacting particles, i.e. how much of the impinging mass accretes, and the connection strength of the accretion to the substrate. The main subject of this study is the ice accretion in mixed phase icing conditions. A thermal model is developed which is capable of predicting the temperature within the layer and as a result, its composition. It considers heat fluxes in the substrate and the accretion as well as convective heat and mass fluxes to the airflow. Phase transitions between the solid, liquid and gaseous state are accounted for, while the impact of particles and droplets is neglected. They are assumed to simply appear on the surface of the accretion and are resolved by the numerical mesh. Setting up a thermal model for the porous ice/water layer is the first step towards a better understanding of ice particle accretion and taking shedding of ice layers into account.

4.2 Model of the ice accretion

4.2.1 Physical model

The temperature in the porous ice/water layer and thus its composition depend on several physical mechanisms taking place within the layer, over its system boundaries and within the substrate on which it accretes. Measurements by Struk et al. (2011) have shown that the temperature slightly below the substrate's surface on which an ice layer accumulates is above the melting temperature T_m for steady-state icing conditions and a wet-bulb temperature above 0 °C. Since the temperature of an ice accretion must be at T_m or below, this indicates that a heat flux in the substrate $\dot{q}_{\mathrm{sub}}$ must be present, even when its surface is cooled down to T_m. This heat flux presumably is a result of the non-uniform covering of the substrate with ice. Dry regions tend due to convective heat fluxes towards the static temperature of the flow T_{st} while wetted areas tend towards the wet-bulb temperature T_{wb} (dissipative heating is neglected). If those temperatures are greater than T_m, this leads to a heat flux towards iced regions of the substrate.

Figure 4.1 shows a sketch of the layer's system boundaries and the heat and mass fluxes across them. Thermal fluxes are shown as solid arrows, whereas the dashed arrows denote mass fluxes. Also, the processes taking place within the layer and the substrate are depicted. Convective heat and mass fluxes are due to the forced airflow around the substrate while the impinging crystals constitute a transfer of mass and sensible as well as latent heat. Each of these mechanisms has to be accounted for in the numerical algorithm in order to represent the layer's thermal behavior correctly. Note that the presented algorithm only accounts for thermal effects. Phenomena resulting from the flow, such as particle trajectories and collection efficiencies resulting herefrom are not covered. Also, the influences of the particle impact, e.g. bouncing, sticking or erosion are out of the scope of this study.

The temperature is dominated by unsteady heat fluxes, convection and conduction. Therefore, the basis for the numerical considerations is given by the energy equation, which reads

$$\frac{\partial(\rho c_p T)}{\partial t} + \nabla\cdot(\rho c_p T \vec{u}) = \nabla\cdot(k\nabla T), \tag{4.1}$$

where ρ is the material density, T the temperature and t represents

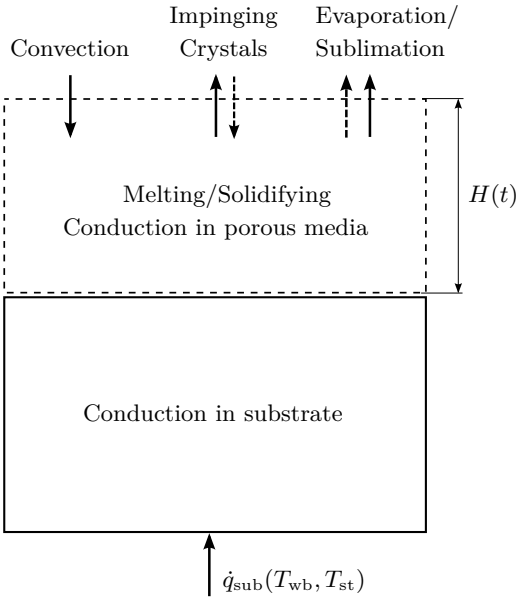

Figure 4.1: Sketch of the modeled system and heat and mass fluxes.

time. The vector field $\vec{u}$ stands for the fluid's velocity, k is the thermal conductivity of the material and c_p its heat capacity at constant pressure. Melting and solidifying of water within the layer is accounted for by imposing Stefan boundary conditions at the concerning interfaces.

The small size of the particles results in cavities of minor dimensions between them. Since the Grashof number is a function of those dimensions raised to the power of three, it becomes very small for the cavities inside of the layer. As the natural convection depends directly on that Grashof number, it is neglected in this work. The forced convective heat transfer from the airflow to the surface of the porous ice/water layer is accounted for by applying a heat transfer coefficient Γ_H on the ice layer's surface. From that heat transfer coefficient a mass transfer coefficient Γ_M is derived

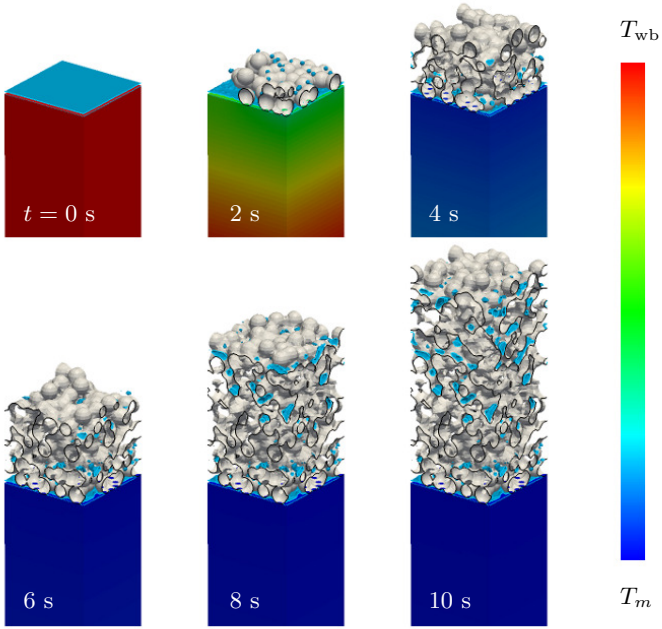

Figure 4.2: Build-up of an ice layer on a warm substrate as modeled in the detailed numerical simulation. White spheres correspond to ice particles and light-blue surfaces are liquid water surfaces. The color of the substrates indicates its temperature.

according to Lienhard IV and Lienhard V (2008):

$$\Gamma_M = \Gamma_H \frac{D}{k} \mathrm{Le}^{1/3}, \tag{4.2}$$

where D is the mass diffusivity of water vapor in air and Le is the Lewis number, defined as the ratio of the Schmidt number to the Prandtl number. The air infinitely close to the water or ice is assumed to be saturated with respect to the surface temperature. Applying the transfer coefficients for a flat surface yields mean heat and mass fluxes for the considered area. The resulting fluxes are spread evenly over the rough

surface of the ice/water layer and are accounted for in the energy equation as source terms.

4.2.2 Numerical approach

A Volume-of-Fluid method is employed to account for the phase distribution. This approach is the basis of the algorithm, which is implemented in the open source software OpenFOAM. A color-function α_i for each phase i (sub: Substrate, s: Solid water/Ice, l: Liquid water, A: Air) is introduced, which takes values between zero and unity. The value gives the volume fraction of the considered phase for each cell of the finite volume discretization. Thus, the sum of the four color-functions is unity at all times. An averaging of the material properties according to these volume fractions α_i is given by

$$\beta = \sum_i \alpha_i \beta_i, \tag{4.3}$$

yielding the averaged field of the arbitrary property β. By means of such averaged property fields it is possible to solve Eq. (4.1) for the entire numerical domain without any prior subdivision. A fixed structured mesh is employed to spatially discretize the numerical domain, which consists of the substrate and the porous ice/water accretion on top of it. In the beginning of the simulation the substrate is initialized with a thin liquid layer on top. The ice particles are assumed to be spherical, are allowed to overlap each other and are randomly distributed, resulting in an accretion as shown in Fig. 4.2. White surfaces denote ice, while blue areas correspond to liquid water. Impinging particles and droplets simply appear on top of the accretion, impact dynamics are not considered.

The heat which is released or is absorbed by the phase change is accounted for in the numerical algorithm as a source term, which is only present at an interface where a phase change occurs. This yields an altered

partial differential equation:

$$\frac{\partial(\rho c_p T)}{\partial t} - \nabla \cdot (k \nabla T) \; = \; \underbrace{\left[\frac{\partial \alpha_l}{\partial t}\right]_{ls} \rho_l L_m}_{\text{Melting/Solidification}} + \underbrace{\left[\frac{\partial \alpha_l}{\partial t}\right]_{lg} \rho_l L_{\text{ev}}}_{\text{Evaporation/Condensation}}$$

$$+ \underbrace{\left[\frac{\partial \alpha_s}{\partial t}\right]_{sg} \rho_s (L_m + L_{\text{ev}})}_{\text{Sublimation/Re-Sublimation}} + \underbrace{\text{sgn}(\mid \nabla \alpha_A \mid) \cdot \dot{q}_C}_{\text{Forced convection}}, \quad (4.4)$$

where $\dot{q}_C$ represents the convective heat flux determined by applying a heat transfer coefficient on the ice layer's surface. A multiplication of that value with the signum function $\text{sgn}(\nabla|\alpha_A|)$ ensures that the convective heat flux is only applied at the interface of the layer to the airflow. The evaporative and sublimative derivatives of the volume fraction with respect to time are obtained from applying the mass transfer coefficient which is derived from the heat transfer coefficient according to Eq. (4.2). L represents the latent heat of the phase change, its index denotes which phase change is considered. The index combination ls denotes a phase change from liquid to solid or vice versa, lg represents evaporation or condensation and sg stands for the solid-gaseous phase transitions. Accounting for the convection this way renders the algorithm highly efficient by avoiding the need for the iterative solution of the velocity and pressure field.

An enthalpy formulation, similar to the ones described by Duan et al. (2002), Tacke (1985), Voller (1985), Voller et al. (1990), is employed to account for the melting and solidifying taking place within the layer. The first step is to compute the temperature field by solving Eq. (4.4). In a subsequent step, the enthalpy which is stored in the solid and the liquid water is calculated according to

$$h_{I+W} = \alpha_s c_{p,s} T + \alpha_l \left[c_{p,s} T_m + c_{p,l}(T - T_m)\right] + \alpha_l L_m. \quad (4.5)$$

The enthalpies at which the onset of melting occurs and at which the melting is complete are called h_{mo} and h_{mc}, respectively. They are defined

for each cell as follows:

$$h_{\mathrm{mo}} = c_{p,s} T_m \Lambda, \quad h_{\mathrm{mc}} = \left(c_{p,s} T_m + L_m\right) \Lambda. \tag{4.6 a,b}$$

The water content Λ of the considered cell is the sum of α_l and α_s. Subsequently, the amount of solid and liquid water in a cell is calculated from the following rule:

$$\alpha_s = \begin{cases} \Lambda & h_{I+W} < h_{\mathrm{mo}} \\ \frac{h_{I+W} - h_{\mathrm{mo}}}{h_{\mathrm{mo}} - h_{\mathrm{mc}}} \Lambda + \Lambda & \text{for} \quad h_{\mathrm{mo}} < h_{I+W} < h_{\mathrm{mc}} \\ 0 & h_{I+W} > h_{\mathrm{mc}} \end{cases}$$

and

$$\alpha_l = \Lambda - \alpha_s. \tag{4.7}$$

This results in an altered α_s and α_l field which in the next time step of the computation releases or absorbs the latent heat of melting according to Eq. (4.4). Another modeled heat and mass transfer are the impinging ice particles. In a first step they are assumed to attach on top of the layer in a random manner at a given impingement rate. This rate depends on the amount of ice contained in the flow and on the behavior of the particles and droplets during impact. The appearance rate of the spheres in the domain is computed by employing an effective collection efficiency γ_{eff} which accounts for collection and sticking of the particles.

4.3 Results and discussion

In order to evaluate the solver's potential of computing mixed phase ice accretion, several experiments presented by Currie et al. (2012) are simulated and used to evaluate the numerical results. Subsequently a study of the influences of the specific mass flux of ice, the wet bulb-temperature and the ratio of liquid to solid water flux density is carried out. Obtained results are compared with the icing limits presented by Currie et al. (2013, 2014).
Table 4.1 gives an overview over physical boundary conditions which are used as input parameters for the numerical algorithm. According to the test article used in the experiments, the substrate has a thickness 3.175 mm, a thermal conductivity of 7 $\mathrm{Wm^{-1}K^{-1}}$ and a density of 4500 $\mathrm{kg/m^3}$. Its specific heat capacity at constant pressure values

523 $\mathrm{J\,kg^{-1}K^{-1}}$. In all considered experiments the ice particle diameter d_s and the liquid droplet diameter d_l values 145 µm and 40 µm, respectively. At wet-bulb temperatures below T_m, impinging droplets are assumed at T_m while particles are at the wet-bulb temperature. If it is above freezing temperature, the solid particles are assumed to be at the melting temperature and the droplets at T_{wb}. The applied heat transfer coefficient is the mean of the measurements valuing 166 $\mathrm{W/(m^2K)}$ and the considered substrate area, i.e. the size of the computational domain, ranges from 0.64 to 1 $\mathrm{mm^2}$. All presented numerical results are based on those values.

Table 4.1: Physical conditions used for the numerical computations.

Run #	Ma	p_t	ϑ_t	ϑ_{wb}	IWC	LWC	γ_{eff}
Unit	(-)	kPa	°C	°C	$\mathrm{g/m^3}$	$\mathrm{g/m^3}$	(-)
543	0.25	44.8	13	-2	7	2.9	0.075
573	0.25	44.8	7	2	17	0	0.126
574	0.25	44.8	7	2	7	0	0.2

4.3.1 Computation of experiments

Numerical simulation of run 573 For the computation of run 573, an effective collection efficiency γ_{eff} of 0.126, which is taken from the experiments, is applied. Since the wet-bulb and the static temperature are above T_m, a substrate heat flux is used which values 42 $\mathrm{W/m^2}$. The composition of the ice/water layer at the substrate determines the connection strength of the layer with the substrate. A freezing initial liquid layer leads to a mechanical interlocking between the ice and the substrate's surface and hence to a strong connection. Contrary to that, liquid water in that region is not capable of transmitting forces and if a closed liquid film emerges, the ice layer is said to shed of the substrate. In order to quantify the conditions at the substrate, a shedding criterion K_T is introduced, which is the ratio of melted liquid water plus water of the film which has not been displaced by ice particles to the available volume in the initial liquid film. This shedding criterion is computed parallel to the calculation of the layer growth and becomes one if a closed liquid layer is present at the substrate. As a result, the ice accretion is removed in the simulation if K_T reaches unity.

Figure 4.3 shows the temporal evolution of the ice layer height H, the surface temperature of the substrate ϑ_{sub} and the shedding criterion K_T during the first 20 s of the run. In this figure dashed lines mark the shedding of the ice layer which is the end of a growth cycle. The first six growth cycles are very short due to the initially high substrate temperature of $\vartheta_{\mathrm{sub}} = \vartheta_{\mathrm{wb}} = 2$ °C which leads to a high heat flux from the substrate which rapidly melts the ice close to its surface. As a result, the mechanical interlocking between ice and substrate is lost. During the first growth cycles no significant icing is observed and the substrate is cooled down almost to 0 °C. In the beginning of each cycle the temperature rises for a short period of time which is due to convective heat inputs in the absence of a melting ice accretion. Subsequent impingement of ice crystals cools the surface again. If the mass flux of ice is high enough to compensate for the convective heat input, the substrate is gradually cooled down eventually to the melting temperature allowing an ice accretion. When the substrate is cooled down and only temperature gradients due to the applied substrate heat flux $\dot{q}_{\mathrm{sub}}$ remain, the growth becomes (quasi-)steady-state resulting in cycles of uniform length.

The lower graph shows the shedding criterion K_T and thereby the evolution of a water film at the substrate over time. At the beginning of each cycle, water is frozen or replaced by impacting cold particles which leads to an icing of the substrate's surface. Subsequently heat fluxes due to convection and a heat flux from the substrate start melting the ice in its proximity resulting in an increase of the shedding criterion K_T.

The layer thickness of the entire run is shown in Fig. 4.4 and compared with the experimental data. Numerically obtained growth and shedding is in very good agreement with the experiments. The first six growth cycles are the ones shown in Fig. 4.3 followed by growth cycles 7-10 with significant accretion.

Figure 4.5 shows the typical development of the shedding criterion for a growth cycle with observable thickness, i.e. cycles 7-10. Initially the melting rate is constant yielding a linear increase of K_T. At some point the slope of the shedding criterion and hence the melting rate at the substrate decreases significantly. This transition of the melting behavior is a result of the insulating effect of the ice layer. Several heat fluxes act on the area close to the substrate in the beginning: the convective heat flux $\dot{q}_{C,\mathrm{ev}}$, which combines the effects of convective heat and mass transfer, the heat flux due to impinging particles and droplets $\dot{q}_W$ and the heat flux from the

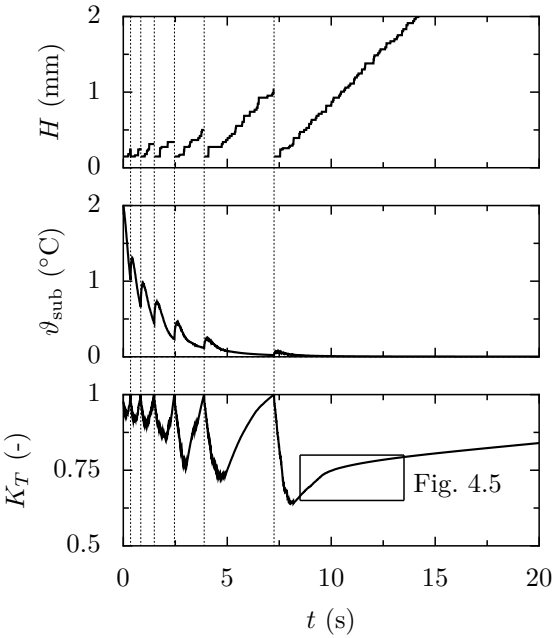

Figure 4.3: Initial stage of the ice accretion. High frequent shedding and cooling of the substrate. Dashed vertical lines denote shedding events. Conditions are for run 573 from table 4.1.

substrate $\dot{q}_{\mathrm{sub}}$. As the thickness of the ice layer increases due to impinging ice crystals and water droplets, the area near the substrate becomes more and more shielded from the heat fluxes which affect the upper surface of the accretion. Therefore, the influence of $\dot{q}_{C,\mathrm{ev}}$ and $\dot{q}_W$ diminishes. At this point only a heat flux coming from the substrate is capable of melting the ice layer connecting the substrate with the accretion resulting in a decreased melting rate. The critical layer height at which no heat is transferred anymore is of the order of magnitude of a few particle radii and depends on the particle shape and the layer's packing density as well as its composition. This transition in the melting behavior is typical for thick ice layers.

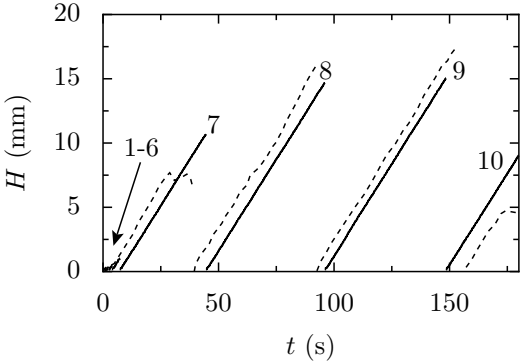

Figure 4.4: Accretion thickness of run 573 over time. Solid lines correspond to numerical results while dashed lines represent experimental data.

Numerical simulation of run 543 The layer height of the well-adhered ice accretion observed in run 543 is depicted in Fig. 4.6, numerical results were obtained assuming an effective collection efficiency of 0.075 and are shown as a solid line. No heat flux in the substrate is applied since this run's wet-bulb temperature lies below T_m. Therefore, shedding occurred only during the cooling of the substrate from initially +2 to 0 °C as shown in Fig. 4.7. Since no heat flux in the substrate is applied as a boundary condition, the shedding criterion tends towards a constant value after the ice layer height passes the critical value of thermal insulation of the substrate's surface. This means that the phase composition at the surface of the substrate remains constant. The result is a non-shedding ice accretion as observed in the experiments.

4.3.2 Influence of IWC, LWC and wet-bulb temperature

Variation of LWC/TWC Former studies have discovered a strong dependency of LWC/TWC on the icing severity. In order to reproduce this behavior, run 574 has been set up and simulated with a varying ratio of liquid to total water content while keeping IWC constant. Figure 4.8 shows the mean ice layer height $\bar{H}$ which represents the icing severity, depending on LWC/TWC. Increasing the liquid fraction significantly reduces the icing severity although the overall incident mass flux increases.

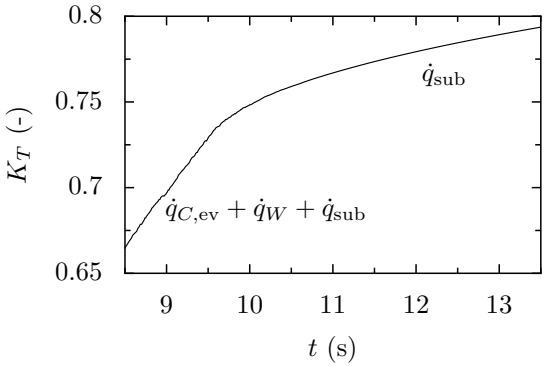

Figure 4.5: Detail of the transition between governing heat fluxes affecting the ice layer at the substrate's surface which typically occurs during growth cycles with significant layer thickness.

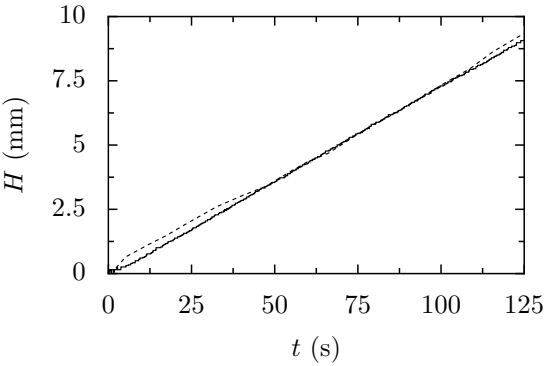

Figure 4.6: Thickness of the well-adhered ice accretion of run 543 over time. Solid lines correspond to numerical results while dashed lines represent experimental data.

The reason for this behavior is that the liquid water carries more enthalpy and has thereby less potential to cool the substrate and the accretion even if it has the same temperature as the impinging ice. As a result, the ice/water layer contains less heat sink potential and therefore its mechanical connection to the substrate is weaker which leads to a higher shedding frequency and hence to a reduced mean ice layer height. The

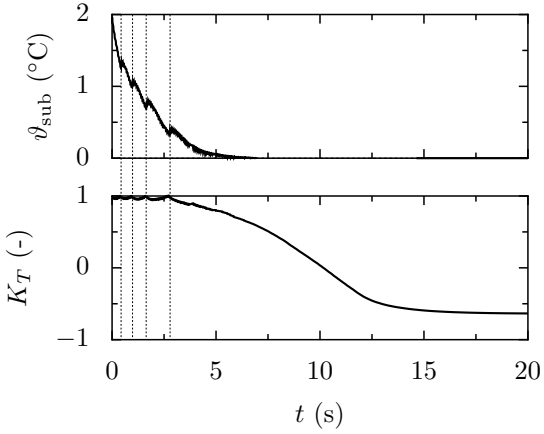

Figure 4.7: Substrate temperature and shedding criterion over time. Dashed vertical lines denote shedding events.

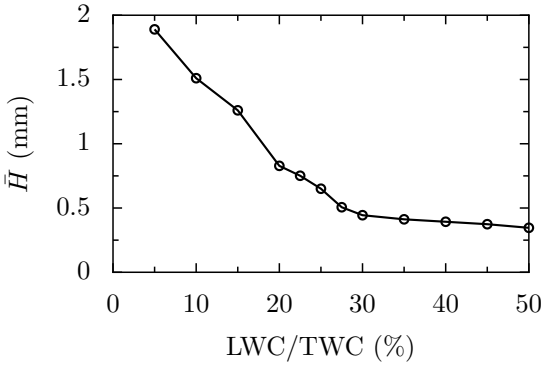

Figure 4.8: Icing severity obtained by means of a thermal consideration.

icing severity is very low and nearly constant for LWC/TWC > 27.5 %. If the liquid water fraction is lower than this value it strongly influences the icing. This numerically obtained icing limit corresponds very well to the upper limit observed by Currie et al. (2013), as shown in Fig. 1.3. Note that the lower limit is not a thermal limit but is governed by the impact process of the particles. That is why this limit is not reproduced by the employed algorithm which only accounts for thermal effects.

In the range of low icing severity the ice layer sheds before it reaches the critical height to insulate the ice at the substrate surface from the heat fluxes acting on top of the accretion. For lower values of LWC/TWC the transition of the slope of the shedding criterion is observed resulting in significantly longer growth cycles. Thus, the severity of the ice accretion is greater.

Computation of limits for the ice accretion In the scope of the following investigation, the transition of the melting behavior at the substrate surface as shown in Fig. 4.5 is employed as a measure for the occurrence of icing. No heat flux from the substrate is applied, so that the transition leads to a constant phase composition at the substrate and therefore to a constant K_T as observed in Fig. 4.7. When this happens, icing with a considerable layer thickness is possible. The initial cooling-down of the substrate is neglected in this analysis and therefore it is initialized to be at the melting temperature. Consequently, only the steady state icing with cycles of uniform length which emerges after the substrate is cooled to the melting temperature is computed. According to the experimental setup, an accretion of particles of a diameter of 145 µm at a flow Mach number of 0.25 is considered. Liquid water is assumed to be dispersed in droplets with $d_l = 40$ µm. Heat and mass fluxes are derived from a heat transfer coefficient of 166 $\mathrm{W/(m^2\,K)}$. This value has been measured Struk et al. (2011) for the corresponding flow around the test article used in the experiments. As all surfaces which are affected by convection are either wetted or covered by ice, the static air temperature and the relative humidity have no individual influence. Their combined effect can be condensed into the wet-bulb temperature. This value represents the flow's convective heating potential. The impact, a possible particle rebound or erosion is not accounted for and only mass fluxes which deposit on the substrate are considered. The amount of the incident mass flux influences the cooling of the substrate and the growth velocity and thereby the time it takes to reach the critical layer thickness. Hence, this parameter has an influence on the icing and is considered in this work. Finally, the ratio of liquid to solid water impinging on the accretion affects the icing limits as presented and explained by Currie et al. (2012, 2013), Struk et al. (2011) and is therefore taken into account as well.

Resulting from these considerations, a critical wet-bulb temperature for a given depositing specific mass flux of ice j_s above which no significant icing is possible has been computed. Figure 4.9 (a) shows the numerically

obtained limit of the wet-bulb temperature for severe icing as a solid line for a ratio of depositing liquid water to accreting ice $j_l/j_s = 0$. Icing is possible at higher wet-bulb temperatures if the specific mass flux of ice is increased. A result of a raised ice flux is a faster growing ice layer reaching the critical height in a shorter period of time. Hence, less time for a convective heat input is available, so that a higher wet-bulb temperature is necessary to melt the ice at the substrate before it is shielded from the airflow. Apart from that influence, a raised ice flux density increases the heat sink potential in the accretion, leading to freezing conditions in the ice/water layer. Symbols denote experiments from Currie et al. (2012, 2013), Struk et al. (2011); the depositing specific mass fluxes were obtained from the injected values of IWC and LWC assuming an effective collection efficiency of $\gamma_{\text{eff}} = 0.1$. Crosses mark experiments, while the corresponding circles indicate the observed icing severity for that run. All experiments in which a medium or severe ice accretion has been observed are within the icing limit predicted by means of the numerical algorithm. Only experiments with no or no significant accretion lie above the limit of ϑ_{wb}.

Figure 4.9 (b) shows the limiting wet-bulb temperature and experimentally observed ice accretion for a ratio of liquid to solid depositing mass flux of 0.2. Again, the experiments which exhibited a severe ice accumulation were performed at a wet-bulb temperature lower than the predicted limit. Above that temperature only a small accretion was observed in the experiments. Results, presented in Fig. 4.9 (a) and 4.9 (b), are in very good agreement with experimental data.

A comparison of several icing limits for the liquid to solid mass flux ratios of $0, 0.1, 0.2, 0.3$ and 0.4 is shown in Fig. 4.9 (c). The kinked course of the icing limit results from connecting discrete outcomes from numerical computations. Increasing the incident mass flux, decreases its influence on the critical wet-bulb temperature. If the incident mass flux is low, it takes some time until the substrate surface is entirely covered with ice. Before that happens, the convective heat input warms the substrate up above 0 °C which effectively reduces the critical wet-bulb temperature. This heating of the substrate above T_m is reduced at higher incident mass fluxes which decreases the influence of the mass flux on the icing limit as more of the heat melting the accretion bottom has to pass through the porous ice layer. Water which additionally deposits on the surface decreases the critical wet-bulb temperature as shown by the lines of constant j_l/j_s. The decrease of the critical wet-bulb temperature is due to the larger

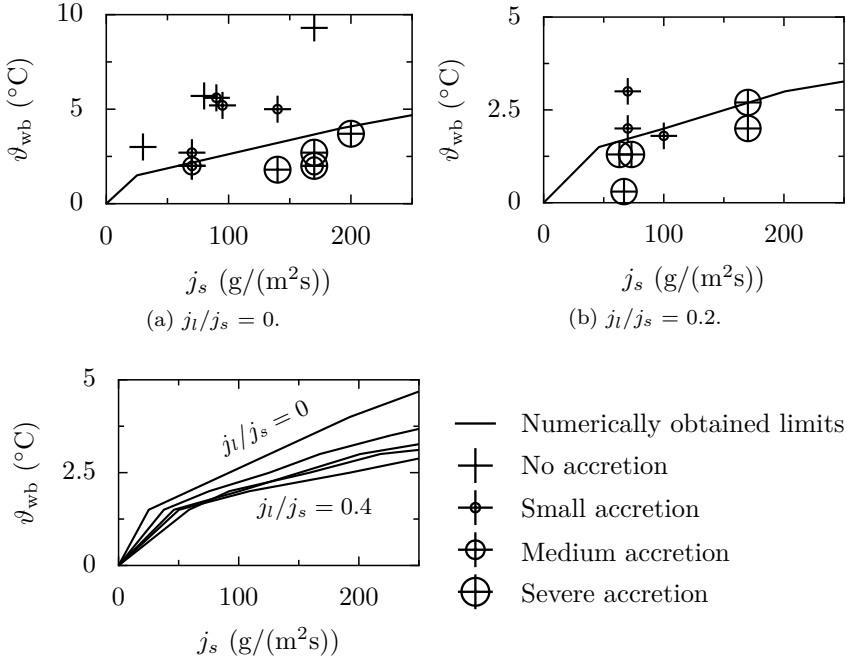

(a) $j_l/j_s = 0$.

(b) $j_l/j_s = 0.2$.

(c) Icing limits for $j_l/j_s = 0$, 0.1, 0.2, 0.3 and 0.4.

Figure 4.9: Numerically obtained icing limits for different ratios of j_l/j_s compared with experimental ice accretion. Experimental specific mass fluxes were obtained assuming $\gamma_{\mathrm{eff}} = 0.1$ for every run.

heat amount of the liquid water resulting in icing which is only possible at colder wet-bulb conditions. Therefore, this chart shows the thermal icing limit for different incident mass fluxes, and melt ratios. This result corresponds to the upper icing limit shown in Fig. 1.3.

4.4 Conclusions

A detailed numerical algorithm for the computation of ice crystal accretion has been developed and presented. In this approach, the individual ice crystals and liquid droplets are resolved which necessitates the usage of a very fine mesh. The very good agreement of the simple test cases which encompass all implemented physical mechanisms verifies the code. A subsequent computation of icing experiments presented by Currie et al. (2012) exhibited good compliance and validated the algorithm. For those computations it is assumed that the ice sheds if a closed liquid layer emerges at the substrate, which loosens the mechanical connection between the accretion and the substrate. By means of the numerical algorithm it has been shown that the melting rate in this region can be subdivided into two stages. Initially, heat fluxes which affect the upper surface of the ice layer play a significant role. After some time, the area close to the substrate is shielded from the heat fluxes due to convection and the impinging water phase. At this point only a heat flux from the substrate can melt the connecting ice between layer and substrate. Such a change of the melting stage is accompanied by a transition in the temporal gradient of the phase composition at the substrate surface. This transition is also observed when varying LWC/TWC and constitutes the upper limit of the range of severe icing. Subsequently, this transition has been employed as an indicator for severe ice accretion in an investigation of the influence of the wet-bulb temperature and the mass fluxes of solid and liquid water. This yielded the thermal limits for which an ice accretion is expected. These limits are in good agreement with existing data of ice accretion experiments in mixed phase icing conditions.

Anyhow, the required fine mesh renders the computations rather computation costly. As a result only a small part (approx. 1 mm^2) of an airfoil is considered. A simulation of the icing of an entire airfoil is currently not feasible at reasonable computing effort using the presented approach.

5 Accretion and shedding of a porous ice/water accumulation: *Theoretical model development*

ABSTRACT Aircraft icing due to ice crystal impact occurs in the relatively hot areas near the engines, where the ice particles partially melt. Ice crystal accretion in the presence of a liquid water fraction leads to the creation of a wet granular ice layer. The present study addresses the transport processes in this granular ice layer in order to describe theoretically the ice accretion phenomenon and to predict the instant of ice layer shedding. Among these transport phenomena are heat transport in the granular solid ice region, water region and gas area, ice granule melting and solidification, and liquid water imbibition. Within the scope of this work, a theoretical model describing these transport phenomena in a granular media is developed. The equations for the effective transport are formulated and solved numerically using a computational code based on a Finite-Volume method. The model is applied to the description of ice crystal accretion on warm aircraft components and the results are compared with available experimental data. The theoretical predictions agree well with the experimentally observed icing and shedding behavior by describing the composition and heat and mass transport within the ice layer.

This chapter is based on the journal article *Transport processes in a wet granular ice layer: model for ice accretion and shedding* by Kintea et al. (2016b), published in the International Journal of Heat and Mass Transfer.

Contents

5.1 Context

In this chapter the transport phenomena in granular, multiphase materials are modeled theoretically. The phenomena encompass heat transfer, melting and liquid phase imbibition. When heat is applied to a porous structure in which one of the phases melts, the heat flux decays over a certain distance due to the energy expended on melting at the grains' boundaries. Information about thermodynamic conditions at the wall does not propagate beyond this thermal boundary layer.

The heat transfer equations are coupled with generation and imbibition equations for the liquid phase. The model is implemented in the framework of a Finite-Volume code and applied to compute the composition of the ice accumulation on airfoils observed in wind tunnel experiments. The composition of the ice layer at the wall provides an estimate of how well the ice is connected to it, thus, modeling the shedding. Finally, the predicted evolution of the thickness of the ice layer and of the instant of the ice shedding are compared with the accretion behavior observed in available experiments. The agreement is rather good.

The detailed model presented in chapter 4 also aims at the prediction of the composition of the accretion and thereby anticipating the adhesion strength and shedding of the layer. This approach yields very good results but is rather computation costly. The current chapter aims at a theoretical modeling of the phenomena occurring in the ice accretion without the need for resolving particles and droplets which allows using a significantly coarser computational grid leading to more efficient icing simulations. As a result, an accurate computation of ice accretion on an entire airfoil is possible at modest computing effort.

5.2 Model development

By means of 3D numerical simulations of the melting of porous materials, it is shown that it can be described by an extinction function, presented in section 5.2.1. A theoretical model for this function is derived in section 5.2.2 and a heat transport equation taking it into account as a source term is presented in section 5.2.3. Imbibition of the liquid water into the porous material is modeled in section 5.2.4 and a final combination of the modeled phenomena yields the melting model, described in section 5.2.5.

5.2.1 3D direct numerical simulations of heat conduction and melting of the porous media

The heat conduction equation

$$\frac{\partial}{\partial t}(\rho c_p T) = \nabla\cdot(k\nabla T), \tag{5.1}$$

in an artificial porous layer is integrated numerically in three dimensions using the Finite-Volume approach presented in chapter 4. Here ρ, c_p and k are the density, specific heat at constant pressure and thermal conductivity of the material which does not change its phase. Its temperature is denoted by T and t corresponds to time.

In the scope of this work, the melting solid phase is assumed to consist of monodisperse spherical particles of radius r_P, which are distributed randomly in the computational domain starting at $x = 0$. Initially, the layer is at thermodynamical equilibrium, i.e. T_m prevails in the entire domain.

The heat transfer in such a layer is determined by conduction in the liquid phase and melting of the grains, which occurs in a thermal boundary layer of certain thickness. In order to investigate the dimension of this layer, the latent heat of fusion is set to infinity to maintain the layer composition and particle size during each computation. By this measure, a steady-state temperature field is derived which is the result of an heat flux $\dot{q}_{\mathrm{in}}$ applied at $x = 0$, which propagates into the porous structure over a certain range. The heat energy is then absorbed by the constant melting temperature which prevails at the stationary surface of the particles at $T = T_m$ representing the melting. None of the heat flux entering the domain is applied in regions covered by ice which would directly absorb it at the boundaries, i.e. $\dot{q}_{\mathrm{in}}$ is only applied at the liquid regions of the boundary at $x = 0$.

Figure 5.1 shows a typical domain used for this analysis. The propagation of the heat flux $\dot{q}(x)$ has been investigated under variation of the relevant material properties, the particle radius r_P, the domain size and the porosity ε of the layer. It has been found that the average heat flux $\dot{q}(x)$ decays exponentially with respect to x. This decay significantly depends on the porosity and on the particle radius while material properties or domain size only play a minor role and are therefore neglected in this work. A dimensional analysis yields the following correlation

$$\dot{q}(x) = \dot{q}_{\mathrm{in}} \exp\left[-\eta(\varepsilon)\frac{x}{r_P}\right], \tag{5.2}$$

for the heat flux and thus

$$T(x) = \frac{\dot{q}(x) r_P}{k\eta(\varepsilon)} + T_m, \tag{5.3}$$

for the temperature. In these equations, η is an extinction function depending only on ε. It determines how fast the heat is absorbed, i.e. it governs the thickness of the thermal boundary layer, over which melting occurs. A measure of this thickness is the decay length, analogous to the time constant of a time-dependent process, which is defined as $l_\lambda = r_P/\eta$.

The exponential behavior of the heat flux in Eq. (5.2) is not surprising. It corresponds to the fact that the effective heat source is proportional to the local temperature difference $(T - T_m)$, which is consistent with the Stefan condition.

The circles in Fig. 5.2 show the extinction function η over the porosity of the layer for all numerically investigated cases. Parameters which did not show any influence on the outcome are applied heat flux $\dot{q}_{\mathrm{in}}$, varied from $10^3 - 10^5$ W/m^2, the thermal conductivity of the liquid and the solid, varied from 0.1 to 10 times the values of water and ice, respectively, and the size of the domain which was investigated in the range from 1.5 to 6 mm edge length. Influencing parameters are the particle radius, altered from 150 to 600 µm and the layer porosity which is analyzed in the range $0.1 - 1.0$.

At low porosity, η tends towards infinity because no heat is able to penetrate a solid ice block which is at the fusion temperature with no pores; all heat applied is directly absorbed by the melting. As the porosity increases, the value of the extinction function is reduced until it becomes zero for a porosity of unity, meaning that no heat is absorbed because no ice is available to be melted.

It is noteworthy that neither the material properties of the melting material nor of the non-melting material have a significant influence on the thermal boundary layer thickness. Even introducing a second non-melting phase occupying the pores did not show any effect. Therefore, the problem is solely governed by geometrical parameters.

5.2.2 Theoretical model for the extinction function

Assume a random distribution of the sphere center positions. Denote a cumulative volume of all the spheres in a unit volume as λ. The probability that a given point belongs exactly to n spheres follows a Poisson distribution (Feller, 2008)

$$P(n;\lambda) = \exp(-\lambda)\frac{\lambda^n}{n!}. \tag{5.4}$$

Parameter λ can now be related to the porosity, which is a probability that a given arbitrary point does not belong to any sphere

$$\lambda = -\ln \varepsilon. \tag{5.5}$$

Depending on porosity, different models have to be used to describe the heat transfer phenomena. For relatively high porosity the spheres intersect and form clusters of different sizes. As soon as the porosity decreases

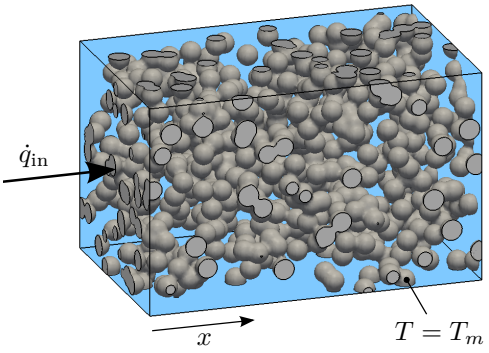

Figure 5.1: Typical computational domain used for the computation of the thickness of the thermal boundary layer. Gray spheres correspond to areas occupied by the melting material where $T = T_m$, while the rest of the domain is filled with the non-melting material which conducts the heat into the porous structure.

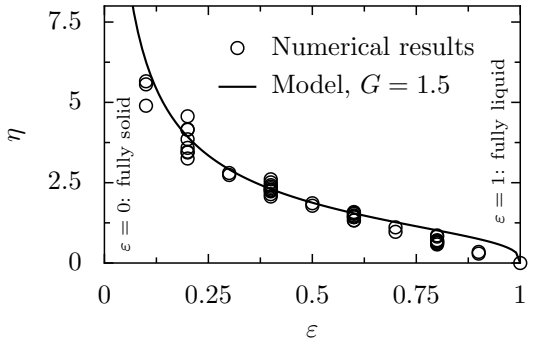

Figure 5.2: Dependency of the extinction function η on the layer porosity ε. Comparison of the results of the 3D direct numerical simulations with the theory (Eq. (5.10)) at $G = 1.5$.

(below a percolation threshold) an infinite cluster size appears. In this case the media can be better represented as clusters of finite lacunae. The percolation threshold for the system of random spheres corresponds to $\varepsilon^\star = 0.71$ (Lorenz and Ziff, 2001, Rintoul and Torquato, 1997). On the other hand the critical porosity corresponding to the void percolation is $\varepsilon^\diamond = 0.032$ (Priour Jr, 2014). The case $\varepsilon > \varepsilon^\star$ corresponds to the discrete solid phase, associated with a suspension. In a static ice accretion a lower porosity is expected, hence this limitation does not apply for the computation of ice crystal accretion. For $\varepsilon < \varepsilon^\diamond$, finite isolated lacunae are distributed in the solid porous media. In that case, no imbibition is possible as the lacunae are not interconnected and the thermal boundary layer is very thin, hence as the porosity tends to zero, the classical Stefan problem is recovered.

The typical average volume of space corresponding to a single sphere is $-4/3\pi r_P^3/\ln\varepsilon$. The characteristic length associated with this volume is therefore

$$r_s = \frac{r_P}{(-\ln\varepsilon)^{1/3}}. \tag{5.6}$$

To estimate the extinction function $\eta(\varepsilon)$, defined in Eq. (5.2) a typical, effective element of the porous media is approximated by a solid ice cylinder of the radius r_s and a cylindrical pore of the radius r_l filled with liquid water. In the porosity range $\varepsilon^\diamond < \varepsilon < \varepsilon^\star$ the typical pore size r_l associated with a void is therefore

$$r_l = r_s\varepsilon^{1/2} = \frac{r_P\varepsilon^{1/2}}{(-\ln\varepsilon)^{1/3}}. \tag{5.7}$$

The temperature distribution in the cylindrical pore, $T(r,x)$, which in the steady state has to satisfy the Laplace equation $\Delta T = 0$, is assumed to take the form

$$T = T_m + \mathrm{R}(r)\exp(-\eta x/r_P), \tag{5.8}$$

where $\mathrm{R}(r)$ is a cylindrical harmonic function satisfying the boundary condition at the melting pore wall, leading to

$$\mathrm{R}(r_l) = 0. \tag{5.9}$$

Figure 5.3 shows the model domain. It comprises a semi-infinite ice cylinder containing a cylindrical pore filled with liquid water. At the inner surface of the ice the fusion temperature is present, i.e. $T(r = r_l) = T_m$,

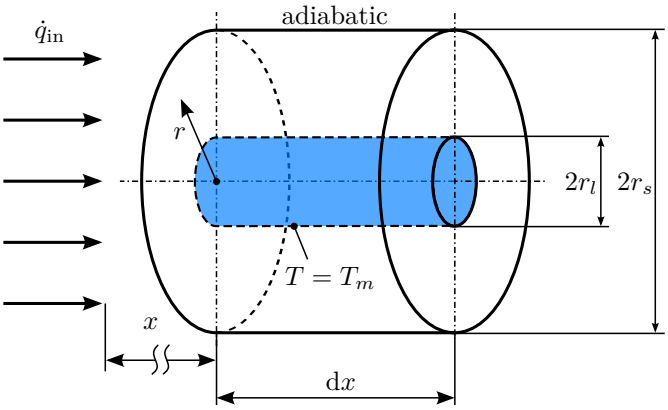

Figure 5.3: Infinitesimal part of the semi-infinite cylindrical domain. The outer radius of the surrounding ice is denoted by r_s, the radius of the pore which is occupied by liquid water is r_l. At $x = 0$ the heat flux $\dot{q}_{\text{in}}$ is applied.

while at the pore center the temperature gradient is zero $(\partial T/\partial r)_{r=0} = 0$. The outer surface of the ice cylinder is adiabatic and at $x = 0$ the heat flux $\dot{q}_{\text{in}}$ is applied.

The boundary condition (5.9) yields the extinction function in the form

$$\eta = \frac{G\,(-\ln \varepsilon)^{1/3}}{\varepsilon^{1/2}}, \quad 0.032 < \varepsilon < 0.71. \tag{5.10}$$

The theoretically predicted root for the constant G is $G \approx 2.405$. However, it is not exact because of the non-precise model geometry which is applied for the more complex porous structure as shown in Fig. 5.1. The value of $G = 1.5$ is obtained from the best fit to the data obtained by the full numerical computation. The comparison of the theoretical predictions with the numerical results for η are shown in Fig. 5.2. The agreement is rather good even for the porosity ε larger than $\varepsilon^\star = 0.71$.

5.2.3 Effective heat transfer equation for granular media with melting

Using the expression for the extinction function $\eta(\varepsilon)$ in combination with Eq. (5.2) or (5.3) enables the computation of the one-dimensional heat transfer problem in melting porous bodies. A more general expression is found when a source term for the heat transfer equation is derived. Consider the one-dimensional, steady-state heat conduction with a source term $S(x)$ describing the melting

$$0 = k\frac{\mathrm{d}^2T}{\mathrm{d}x^2} + S(x). \tag{5.11}$$

The solution of this equation is described by Eq. (5.3). Hence, the source term can be written as

$$S(x) = -k\frac{\eta^2}{r_P^2}\underbrace{\frac{\dot{q}_{\mathrm{in}}}{k}\frac{r_P}{\eta}\exp[-\eta\, x/r_P]}_{T-T_m}. \tag{5.12}$$

Thus, the transient heat conduction equation which takes heat absorption/release due to melting at the grains' boundaries into account reads

$$\frac{\partial(\alpha_l \rho c_p T)}{\partial t} = \nabla\cdot(k\nabla T) - \frac{k\eta^2(T-T_m)}{r_P^2}, \tag{5.13}$$

where α_l corresponds to the volume fraction of the liquid, which equals ε if no third phase is present. The conductivity of the material which occupies the pores is denoted by k, its value does not affect the extinction function. Therefore, this equation is valid for pores which are filled with air as well as with liquid water or a mixture of both. In that case, the thermal conductivity is averaged according to the volume fractions. The second term of the right-hand side is the source term modeling the heat transfer and absorption in the porous structure. Note that this equation only describes the mean temperature within the liquid as the temperature of the melting phase equals T_m.

The change in the liquid volume fraction due to melting/solidification is also described by the source term presented in Eq. (5.12). This term corresponds to the energy absorbed/released due to the phase change;

dividing it by the density and the latent heat of fusion L_m yields the change in volume of the liquid phase due to fusion processes

$$\left[\frac{\partial \alpha_l}{\partial t}\right]_m = \frac{k\eta^2(T - T_m)}{r_P^2\, \rho L_m}. \tag{5.14}$$

5.2.4 Imbibition of liquid water

Liquid water, in particular the arising liquid water which is in direct contact with the porous structure, is imbibed into its pores by capillary suction. This mass transfer leads to a change in water content of the layer and is also accompanied by a convective transport of heat. The transport of liquid water can be described by a diffusion-like equation presented by Luikov (1966). For isothermal conditions, it reads

$$\frac{\partial \zeta}{\partial t} = \nabla\cdot(a\nabla\zeta), \tag{5.15}$$

where a is the moisture transfer coefficient, analogous to the diffusion coefficient, and ζ is the dimensionless moisture content, defined as the ratio of the liquid substance which is interstitially bound, m_l, to the mass of the dry solid substance, m_s. Assuming $\rho_l = \rho_s = \rho$, it can also be expressed in terms of volume fractions

$$\zeta = \frac{m_l}{m_s} = \frac{\alpha_l}{\alpha_s}. \tag{5.16}$$

Moreover, a spatially uniform distribution of the solid volume fraction α_s is assumed, which is valid for most applications. Also, the melting usually is significantly slower than the imbibition, which justifies the neglect of the derivative of α_s with respect to time when evaluating Eq. (5.15) in combination with (5.16). Thus, it can be written in terms of the liquid volume fraction instead of the dimensionless moisture content

$$\frac{\partial \alpha_l}{\partial t} = \nabla\cdot(a\nabla\alpha_l). \tag{5.17}$$

The imbibition model presented by Luikov is well validated and yields very good results for low moisture content, i.e. when there is always enough free space left in the pores to accommodate the water. At higher moisture content, which is encountered when considering melting

processes, it can give erroneous results by predicting imbibition into regions which are already fully occupied by solid and/or liquid material under certain circumstances. This is avoided by weighting α_l with a function which is unity in regions where the volume fraction which is occupied by liquid or solid α_{oc} is less than one, i.e. free space is available, and becomes large when α_{oc} tends towards unity. Thereby, it prohibits water migration into regions which are almost occupied, by artificially increasing the water content for the calculation of the gradient in Eq. (5.17). The weighting function used in this work, reads

$$\mathrm{J}(\alpha_{\mathrm{oc}}) = \frac{1}{400(\alpha_{\mathrm{oc}} - 1.02)^2} + 1. \tag{5.18}$$

Thus, Eq. (5.17) becomes

$$\left[\frac{\partial \alpha_l}{\partial t}\right]_i = \nabla\cdot(a\nabla[\alpha_l \mathrm{J}(\alpha_{\mathrm{oc}})]). \tag{5.19}$$

This treatment avoids filling regions over the limit of $\alpha_{\mathrm{oc}} = 1$ while still maintaining mass conservation. The term $-a\nabla[\alpha_l \mathrm{J}(\alpha_{\mathrm{oc}})]$ represents the velocity $\vec{u}_i$ at which the water is imbibed into the porous structure.

5.2.5 Coupling of the heat transfer, melting and liquid water imbibition

A combination of the previously derived models for the heat transfer and the imbibition of liquid into the porous structure yields a model for the melting of porous materials.

Combining Eqs. (5.19) and (5.14) leads to the equation for the liquid volume fraction

$$\frac{\partial \alpha_l}{\partial t} = \left[\frac{\partial \alpha_l}{\partial t}\right]_m + \left[\frac{\partial \alpha_l}{\partial t}\right]_i = \frac{k\eta^2(T - T_m)}{r_P^2\, \rho L_m} + \nabla\cdot\left(a\nabla[\alpha_l \mathrm{J}(\alpha_{\mathrm{oc}})]\right), \tag{5.20}$$

which comprises a contribution from the melting of solid ice and one due to the capillary migration of the water. The energy which is stored in the liquid water is described by means of Eq. (5.13), with an additional convective term taking into account the imbibition of water described in

Eq. (5.19). The governing transport equation for the energy stored in the liquid therefore reads

$$\frac{\partial(\alpha_l \rho c_p T)}{\partial t} + \nabla\cdot(\vec{u}_i \rho c_p T) = \nabla\cdot(k\nabla T) - \frac{k\eta^2(T - T_m)}{r_P^2}. \tag{5.21}$$

The particle radius, which diminishes as the ice melts, is correlated to the layer porosity

$$r_P = r_0\sqrt{\frac{1-\varepsilon}{1-\varepsilon_0}}, \tag{5.22}$$

where the index 0 denotes initial values, i.e. r_0 and ε_0 are the initial values of the particle radius and layer porosity.

Equations (5.20) – (5.22) describe energy stored in the liquid and its movement due to capillary suction, while the ice is assumed to be at T_m. When freezing should also be taken into account, a second set of equations is needed, analogous to the ones for the melting, but without the imbibition terms, e.g. by setting $a = 0$.

The key assumptions which were made leading to the model either can be categorized into assumptions for the conductive heat transport and for the convective transport of heat and mass. For the conduction model described in section 5.2.1 – 5.2.3 it is assumed that the porous material consists of monodisperse spherical particles which are randomly distributed and can overlap each other. Their temperature equals the melting temperature T_m, which is assumed to be constant as well as the material properties of each phase. The model for the convective heat and mass transfer described in section 5.2.4 is based on the assumption of isothermal conditions, a spatially uniform distribution of the solid phase and assuming that the melting is slower than the imbibition of liquid water. Moreover, the density of the liquid is assumed to be equal to the solid density.

5.3 Results and discussion

5.3.1 One-dimensional consideration

A discussion of the influence of the heat transfer and the imbibition of liquid water leading to a heat affected zone in which material melts is conducted in this section. A subsequent comparison of the results obtained with the presented porous layer model with the solution of the Stefan problem shows the impact the porosity has on the melting.

A semi-infinite, one-dimensional slab is considered in this section. At its end, a constant temperature $T(x = 0) > T_m$ is prescribed and the slab is occupied by porous ice with an initial porosity of $\varepsilon_0 = 0.5$. Half of the pores are filled with liquid water ($\alpha_{l,0} = 0.25$) while the other half is filled with air ($\alpha_{A,0} = 0.25$). The initial temperature is 0 °C in the whole slab, therefore, melting starts instantaneously at $t = 0$.

5.3.1.1 Influence of the particle radius

To demonstrate the influence of the particle radius on the thickness of the thermal boundary layer, three different initial particle radii $r_{P,0} = \{r_f,\ r_f/10,\ 2r_f\}$ are considered, where r_f is the reference radius which equals 20 µm. No imbibition of water is taken into account. As shown in chapter 5.2.1, if the particle radius remains constant, i.e. the steady-state temperature field is considered, the decay length l_λ linearly depends on r_P. Here we consider the melting of the ice spheres which therefore decrease in size according to Eq. (5.22). Figure 5.4 shows the volume fraction of the solid ice, α_s, normalized with its initial value $\alpha_{s,0}$ over non-dimensional position. Even though the exact definition of the decay length is not valid for a non-constant particle radius, the thickness of the thermal boundary layer is proportional to the particle radius. This is true despite a non-constant coefficient in the exponent in Eq. (5.2), because their development only depends on the volume fraction of the solid ice. Therefore, the shape of the decay is time independent and the same for all initial particle radii.

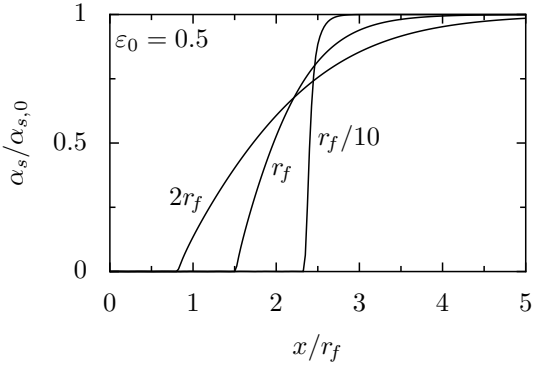

Figure 5.4: Dependency of the thickness of the thermal boundary layer on the initial particle radius $r_{P,0}$ for an initial porosity of 0.5.

5.3.1.2 Influence of the imbibition

The effect of the imbibition on the melting behavior is discussed considering a layer consisting of particles of the reference radius r_f at four different moisture transfer coefficients $a = \{0,\ a_f/2,\ a_f,\ 2a_f\}$, where $a_f = 1.35 \cdot 10^{-9}$ m^2/s. Figure 5.5 shows the volume fraction of the ice normalized with its initial value with respect to the non-dimensional position at $t = 6.75 r_f^2/a_f$. No imbibition occurs for $a = 0$; increasing the moisture transfer coefficient reduces the velocity at which the smeared interface moves nearly linearly. As a result, the distance between interfaces of melting processes with different moisture transfer coefficients varies with time. As the melted water is sucked into the pores of the solid material, less water remains in the melted region. The lower melting pace is a result of the decreased water content in this region reducing heat conduction to the melting site.

5.3.1.3 Comparison with the one-dimensional Stefan problem

A solid ice slab is considered in the Stefan problem. To account for the fact that less material needs to be melted when considering a porous layer, the density of the melting material is multiplied with $\alpha_{s,0}$ of the porous material. The initial particle radius for the porous layer model equals r_f and the reference moisture transfer coefficient is a_f. Figure 5.6

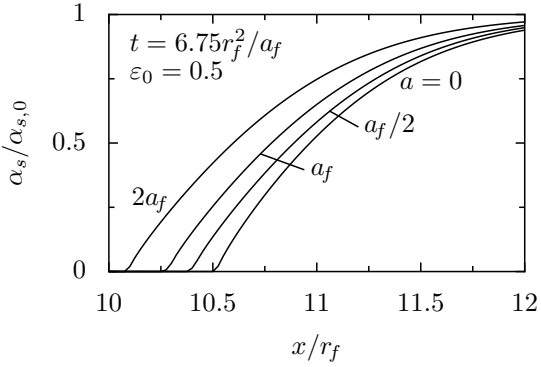

Figure 5.5: Position and shape of the heat affected zone depending on the value of the moisture transfer coefficient at $t = 6.75r_f^2/a_f$.

compares the non-dimensional temperature $T/T(x = 0)$, the liquid and solid volume fraction of the solution of the Stefan problem (dashed lines) with the results obtained with the porous layer model (solid lines). It corresponds to an instant shortly after the onset of the melting process, $t = \rho c_p r_f^2/(150k_l)$, where the infinitesimally thin melting front of the Stefan problem moved approximately $0.75r_f$. At the same time, the melting is smeared over approximately $2r_f$ and ice is still present at $x = 0$ in the prediction of the porous layer model. In this heat affected zone the volume fraction of liquid and solid varies smoothly, while it changes abruptly in the solution of the Stefan problem.

5.3.2 Application to aircraft engine icing

Ice layers observed in aeronautical engines usually consists of a mixture of ice, water and entrapped air. Such ice layers were successfully reproduced in different wind tunnel experiments, where accretion and shedding behavior is observed or the required heater power for anti-icing is measured. The porous layer model, derived in chapter 5.2.2, is applied to predict the outcome of different icing experiments.

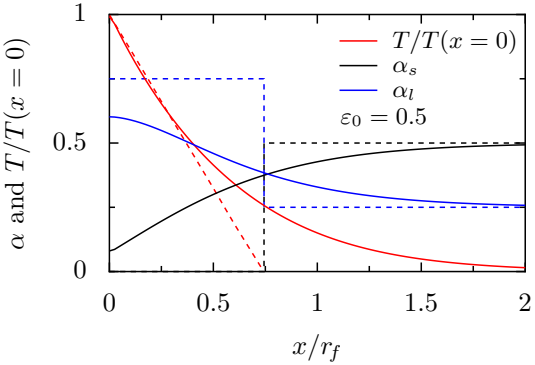

Figure 5.6: Comparison between the melting as predicted by the porous layer model (solid lines) with the solution of the Stefan problem (dashed lines).

5.3.2.1 Description of experiments

In the experiments presented by Struk et al. (2011) and Currie et al. (2012), a wedge-type airfoil is placed in an icing wind tunnel and exposed to a warm flow ($\vartheta_\infty > 0$ °C, ϑ being the temperature in Celsius scale) laden with solid ice particles and liquid droplets. Depending on the boundary conditions, the three different icing behaviors "well-adhered accretion", "regularly shedding ice" and "no accretion" are observed and the leading edge ice thickness H is measured. According to the 9-bin representation given by Currie et al. (2015), the mean ice particle radius equals 35 µm. The airfoil comprises two parts, a body out of PTFE and an insert made of Ti6Al-4V. The exact shape and composition can be found in Currie et al. (2012), Struk et al. (2011).

A NACA0012 airfoil is equipped with heaters in the experiments performed by Al-Khalil et al. (2003). These heaters are operated separately to ensure anti-icing conditions with a surface temperature between 4.4 and 10 °C. While liquid droplets and ice crystals are injected into the flow, the necessary power for anti-icing is measured. Different ice particle radii are used in these experiments ranging from 75 up to 92.5 µm. The airfoil consists of different layers as explained in Al-Khalil et al. (2003). In the scope of the numerical simulation only the ones between the heating elements and the outer surface of the airfoil are considered. These

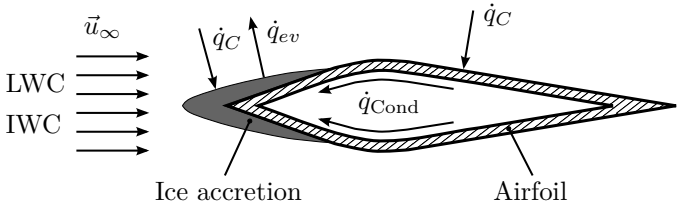

Figure 5.7: Sketch of the computational domain and boundary conditions for the computation of the icing of the wedge-type airfoil. The airfoil has the same geometry, dimensions and composition as the one used in Currie et al. (2012), Struk et al. (2011).

are the erosion shield out of SS 301 HH and one layer of the elastomer COX 4300.

5.3.2.2 Numerical approach

When computing the icing of an airfoil, the computational domain is subdivided into two parts, the airfoil and the porous ice/water accretion. While the airfoil is a solid part and only heat conduction is considered in this domain, the accretion consists of a porous ice structure in which the presented porous layer model is applied. The boundary conditions of this domain are given by convective heat and mass fluxes to the surrounding airflow on the outside while the inside of the airfoil is assumed to be adiabatic. Figure 5.7 shows a sketch of the two-dimensional computational domain and its boundary conditions. The freestream airflow traveling at velocity $\vec{u}_\infty$ carries mixed-phase particles with liquid and ice water contents LWC and IWC, respectively, which impinge and accrete on the airfoil. While evaporative heat fluxes $\dot{q}_{ev}$ are only present on the surface of the wet accretion, convective heat fluxes $\dot{q}_C$ heat up the airfoil and the accretion. As dissipative heating is neglected, the non-wetted airfoil tends towards the static air temperature while the accretion would tend to the wet-bulb temperature if melting/solidifying of water would not take place keeping the temperature at the melting temperature. As a result, conduction in the airfoil transports the heat $\dot{q}_{\mathrm{Cond}}$ from the rear of the airfoil towards the iced leading edge and thereby melts the ice from the surface on which it accumulates.

Computation of local heat and mass transfer coefficients For the computation of the local heat transfer coefficients the open source software OpenFOAM and the turbulence model by Spalart and Allmaras (1992) is employed. Figure 5.8 shows the two-dimensional domain used for the computation of the heat transfer on the surface of the wedge airfoil with a chord length of $l_{\mathrm{ch}} = 221$ mm. The length of the diverging part of the airfoil, i.e. from the leading edge to the thickest section is denoted by l_{div}, the converging part is $l_{\mathrm{conv}} = l_{\mathrm{ch}} - l_{\mathrm{div}}$. Along the symmetry axis, the distance between leading edge of the airfoil and the inlet boundary of the domain equals l_{ch} while it is $3/4 l_{\mathrm{ch}}$ between trailing edge and outlet. The height of the domain corresponds to the vertical dimension of the wind tunnel $l_{\mathrm{WT}} = 254$ mm. It is meshed using a structural grid with 327000 cells with a local refinement at the airfoil resulting in a cell thickness of 1 µm at its surface. With this grid refinement, the dimensionless wall distance y^+ was well below one for all computations.

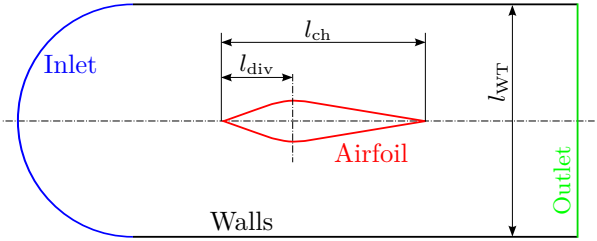

Figure 5.8: Sketch of the domain used for the computation of the local heat transfer coefficient at the surface of the wedge airfoil without angle of attack.

Figure 5.9 shows the numerically computed distribution of the heat transfer coefficient Γ_H along the chord length (the origin of the abscissa corresponds to the thickest section of the airfoil; the position x is non-dimensionalized with l_{div} and l_{conv} for the diverging and the converging part of the airfoil, respectively) in comparison with measurements performed by Struk et al. (2011) at a total pressure of $p_t = 44.8$ kPa and no angle of attack at different Mach numbers. Depending on the flow velocity, different values of $\tilde{\nu}$ have to be prescribed as inflow conditions at the inlet. With rising Ma number, the used inlet value $\tilde{\nu}_{\mathrm{inl}}$ increases valuing 40ν, 50ν and 55ν, where ν is the molecular viscosity corresponding to the considered experimental run.

The agreement between numerically obtained results and experimental data is rather good which verifies the computation.

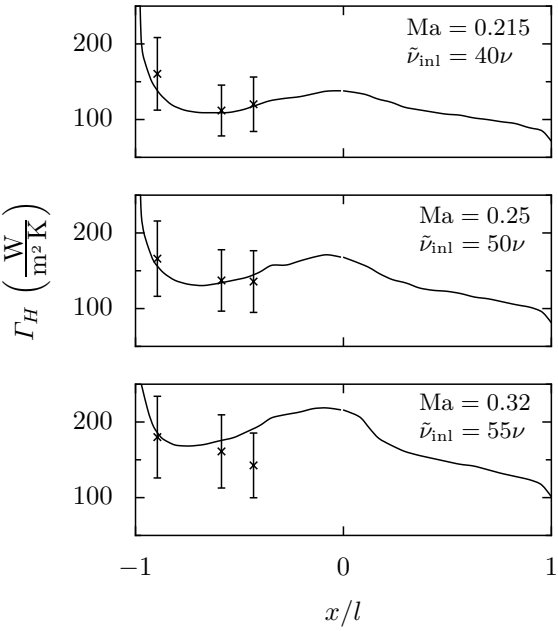

Figure 5.9: Comparison between computed heat transfer (solid lines) and measured data (crosses) at different Mach numbers.

Figure 5.10 shows the distributions of the heat transfer coefficient for the three configurations necessary to compute cases 1–7. The solid lines correspond to the suction side of the airfoil while dashed lines represent the heat transfer coefficient of the pressure side, which is its upper side due to the negative angle of attack; the lines coincide if no angle of attack is present. For Ma = 0.2 the ratio of $\tilde{\nu}_{\mathrm{inl}}/\nu$ equals 40 while it is 50 for a Mach number of 0.25.

Additionally, such simulations were performed for various ice thicknesses up to 30 mm leading edge thickness. However, the effect on the heat and mass transfer coefficient was less than 10 % and therefore neglected in this work.

Figure 5.11 shows the heat transfer coefficient for cases 8 and 9 which

correspond to a NACA0012 airfoil ($l_{\mathrm{ch}} = 0.9144$ m) without angle of attack at a Mach number of 0.167. The computation has been performed analogously to the ones for the wedge airfoil, while the inlet value $\tilde{\nu}_{\mathrm{inl}}$ equals 25ν in this case.

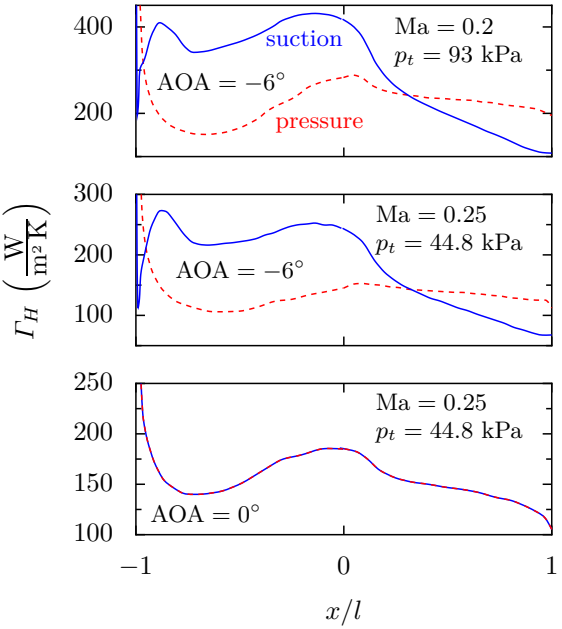

Figure 5.10: Local heat transfer coefficients for the three configurations used in cases 1–7 which correspond to the wedge airfoil.

Utilizing the analogy between heat and mass transport, the local mass transfer coefficients are derived from the results for the heat transfer coefficients (Lienhard IV and Lienhard V, 2008). It reads

$$\Gamma_M = \mathrm{Le}^{1/3} D_{\mathrm{H2O},A} \Gamma_H / k_A, \tag{5.23}$$

where the Lewis number is denoted by Le, $D_{\mathrm{H2O},A}$ is the diffusivity of water vapor in air and k_A corresponds to the thermal conductivity of air.

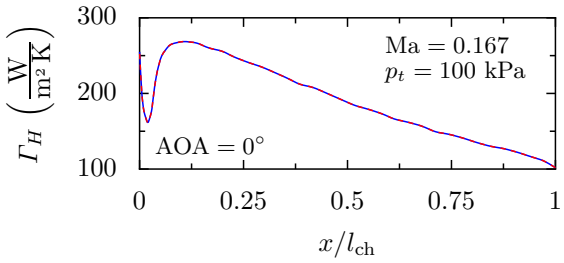

Figure 5.11: Heat transfer coefficient on the NACA0012 airfoil for cases 8 and 9.

Accretion growth model Size and shape of the accretion depends on many factors and vary with time. In the scope of this work, the growth model presented by Currie et al. (2014) is employed to predict the shape of the accretion with respect to time, while its composition is computed by means of Eqs. (5.10) and (5.20) – (5.22).

Ballistic particle trajectories are assumed for the growth model which yields a certain local ice accretion growth rate, which is assumed only to take place in the leading edge region of the test articles. This region was determined from a comparison with the experimental accretion. Ice only accretes on the first 25 mm on the wedge airfoil (Currie et al., 2012) which corresponds to half the diverging part while it accretes on the first 19 mm of the NACA0012 airfoil (Al-Khalil et al., 2003). Local growth rates are predicted by the model and matched with experimental data. This growth is also applied during time periods, in which no icing occurs, e.g. during the cooling of the airfoil. In that case, the ice melts so rapidly that sheds off the surface without forming a macroscopic accretion.

The mechanical connection of the accretion to the airfoil is principally a result of the mechanical interlocking of solid ice with the surface roughness of the airfoil. Therefore, shedding of the ice accretion is assumed to occur, when a certain amount of the ice at the airfoil is melted, leading to a loss of the interlocking. By comparing calculations with available experiments, a critical value at which shedding occurs is found. If K_A, defined as the ratio of iced area to the area which is covered by the ice/water accretion, drops below 20 %, shedding of the ice is assumed, i.e. the accretion is removed from the airfoil starting a new growth cycle. This value is found by comparing simulation results of case 4 of table 5.4.

Table 5.1: Material properties of liquid and solid water and air used in the numerical simulations.

	Unit	Liquid	Solid	Air
k	W/(mK)	0.564	2.24	see App. A
ρ	kg/m^3	1000	1000	$p/(RT)$
c_p	J/(kgK)	4180	2060	1006

Assumptions for ice crystal accretion Experimentally observed ice layers exhibited an opaque, whitish appearance, indicating entrapped air in the accretion. Lacking an exact value of the gaseous volume fraction, an initial value of $\alpha_{A,0} = 10$ % is assumed, while the initial values of α_s and α_l are set according to the ratio of liquid to solid water content of the airflow. The initial radius r_0 of the accumulating ice particles is set to the mean particle radius in the flow.

Moisture transfer coefficients for gypsum, gas concrete or foam concrete range from $3.06 \cdot 10^{-10}$ to $1.81 \cdot 10^{-9}$ m^2/s (Luikov, 1966), while no value is known to the authors for wet ice crystal accretion. Following the value range of gypsum and concrete, a moisture transfer coefficient of $a = 1.35 \cdot 10^{-9}$ m^2/s is assumed, which is exactly 1 % of the thermal diffusivity of water. The latent heat of fusion and evaporation value 333 and 2500 kJ/kg, respectively. Other material properties required for the computation of the experiments are given in Tables 5.1, 5.2 and 5.3.

Solidification of liquid water is taken into account by also solving for the temperature in the solid using the same equations used for the temperature in the liquid with some modifications. A temperature below freezing is not transported by the pore material, but by the solid one. Therefore, for the computation of the temperature in the solid ice the porosity has to be replaced by $1 - \varepsilon$ yielding the ice volume fraction. Moreover, no imbibition of the solid takes place, which is achieved by setting $a = 0$ for the solid phase.

No variations in spanwise direction are assumed allowing a two-dimensional consideration of the icing process.

Table 5.2: Material properties of the components of the wedge airfoil.

	Unit	Ti6Al-4V	PTFE
k	W/(mK)	7	0.24
ρ	kg/m^3	4500	2150
c_p	J/(kgK)	523	1090

Table 5.3: Material properties of the NACA0012 airfoil layers.

	Unit	SS 301 HH	COX 4300
k	W/(mK)	16.27	0.2561
ρ	kg/m^3	8025	1384
c_p	J/(kgK)	502	1256

5.3.2.3 Results of computations

The outcome of simulations of ten different icing experiments are presented in this section and compared with results obtained in the wind tunnel experiments. Different icing behavior such as “no icing”, “regularly shedding” accretion and “well-adhered” accretion were observed in the experiments. In the “no icing”-cases either no or only little ice, i.e. few millimeters, accumulated on the leading edge of the airfoil while ice thickness of several up to > 20 mm were observed for “regularly shedding” and “well-adhered” accretion.

No icing Cases 1–3 of Table 5.4 correspond to wind tunnel experiments where “no” or only a “small amount” of ice (Currie et al., 2012, Struk et al., 2011) has been observed accreting on the leading edge of the airfoil. The numerically predicted ice accretion melted rather quickly leading to a high frequency shedding with a maximum layer thickness at the leading edge of 0.25–1.0 mm. Before the ice thickness can grow to a thickness which would shield the area in the vicinity of the airfoil determining the connection strength, it is melted, resulting in very little ice accretion. This result corresponds rather well with the experimentally observed small ice accretion and the findings presented in chapter 4.

Table 5.4: Operational conditions for the numerical computations of ice accretion on the wedge-type airfoil, based on experimental cases presented in Currie et al. (2012), Struk et al. (2011).

	ϑ_t	ϑ_{wb}	p_t	Ma	AOA	TWC	LWC
Unit	°C	°C	kPa	-	°	g/m^3	g/m^3
Case 1	13	2	44.8	0.25	0	9.9	2.2
Case 2	22	3	44.8	0.25	0	9.1	1.53
Case 3	14.6	4.4	93	0.2	−6	10	2
Case 4	7	2	44.8	0.25	−6	17	2.5
Case 5a	20	2	44.8	0.25	−6	17	1.25
Case 5b	20	2	44.8	0.25	−6	17	2.5
Case 6	6	−2	44.8	0.25	0	9.9	1.8
Case 7	13	−2	44.8	0.25	0	9.9	1.2

Table 5.5: Operational conditions for the numerical computations of the anti-icing experiments using a NACA0012 without angle of attack (Al-Khalil et al., 2003, Miller et al., 1997).

	ϑ_t	p_t	Ma	TWC	LWC	r_0
Unit	°C	kPa	-	g/m^3	g/m^3	µm
Case 8	−11.1	100	0.165	0.7	0.35	92.5
Case 9	−17.8	100	0.167	0.7	0.35	75

Regularly shedding accretion In the experimental runs of case 4, 5a and 5b significant ice layer growth on the airfoil has been observed, which shed cyclically after a certain period of time. Typically, the experiments start with short growth cycles as the airfoil is at the static air temperature at the beginning which was above freezing in all of the considered cases. The resulting heat flux from the airfoil quickly melts the ice in the vicinity of the airfoil detaching the accretion from the surface resulting in rather short accretion cycles. After the leading edge region on which the ice accretes, is cooled down to 0 °C, accretion cycles of uniform length occur.

Figure 5.12 shows the ice thickness H of case 4 on the leading edge over time, including results obtained by means of the porous layer model (solid line) and data from the corresponding experiment (dashed line). During approximately the first ten seconds of the simulation only very short and high-frequently shedding accretion occurred, which cools down the airfoil. After it reaches nearly the melting point of ice, significant ice layer growth

is observed. The first cycle with a macroscopic ice layer thickness is shorter than the following cycles in both the experiment and the simulation. These cycles exhibit uniform growth rate and cycle length as the leading edge of the airfoil is entirely cooled to ϑ_m and only conductive heat fluxes, originated in the convective heat input in the non-iced regions, melt the ice. In the experiment, the injection of water and ice particles is switched off at 180 s (dotted line), which is not taken into account in the simulation. Cycle length, emergence of uniform cycles and the cooling of the airfoil is well reproduced and explained by the model.

Figure 5.13 shows the composition of the ice accretion on the leading edge of the airfoil (shown in dark gray) throughout the first uniform length accretion cycle which starts at $t \approx 22$ s. The color of the accretion indicates its volumetric water content and therefore its composition. If ϑ_{wb} is greater than 0 °C, two distinguishable heat fluxes melt the ice. One is the heat flux $\dot{q}_{\mathrm{Cond}}$ conducted through the airfoil and has its origin in the convective heat input in the non-wetted region of the airfoil. It melts the ice from the airfoil, starting from the rear of the accretion. The other heat flux is the one directly acting at the surface of the accretion, comprising convective heating and evaporative cooling with a positive sum if $\vartheta_{\mathrm{wb}} > \vartheta_m$. This heat flux melts the ice from the outside and has, together with the local growth rate and the ratio of impinging mass fluxes, a significant influence on the initial composition of the ice. In this experiment, the airfoil was inclined, therefore the heat transfer coefficient on the suction side is larger, resulting in faster melting of the ice in this region. At wet-bulb temperatures above freezing, significant ice accretion only occurs if the accretion grows fast enough to shield the ice at the airfoil from the convective heat flux acting on the surface of the accretion. If the accretion is able to reach the critical thickness, only the heat flux from non-covered regions is able to melt the connecting layer, unless the entire accretion melts. On the pressure side of the airfoil shown in Fig. 5.13, the melting by $\dot{q}_{\mathrm{Cond}}$ dominates while on the suction side the convective heat flux at the accretion prevails melting the entire ice of the accretion.

Figure 5.14 shows the accretion thickness of case 5 over time. In the first 116 s (case 5a), 1.25 g/m^3 liquid water content is injected while it is doubled afterwards (case 5b). As already observed in case 4, the first cycles are shorter due to the initially warm airfoil. By increasing the water mass flux, the accretion thickness rises approximately by a factor of 2 in the experimental data as well as in the numerical simulation. This is the result of an increased growth rate predicted by the employed

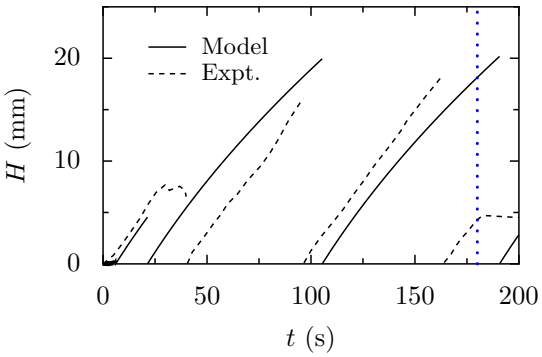

Figure 5.12: Ice layer thickness at the leading edge for case 4.

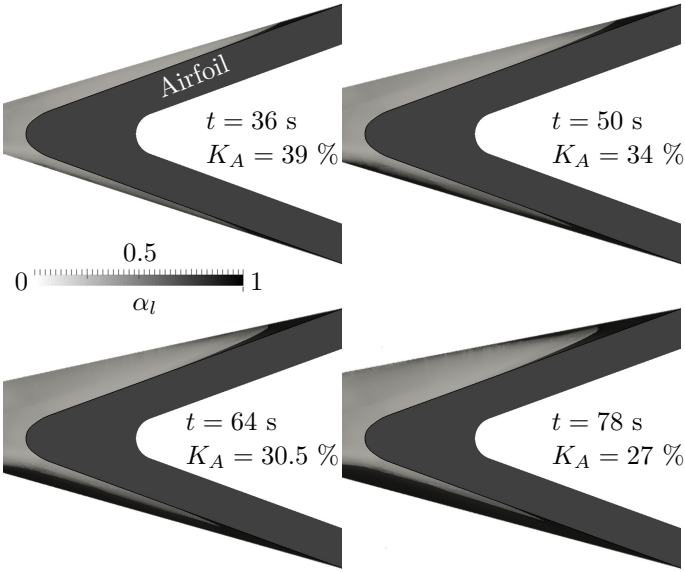

Figure 5.13: Composition of the ice accretion on the leading edge of the airfoil of case 4 during the first accretion cycle with uniform length starting at $t \approx 22$ s. The airfoil is colored dark gray while the color of the accretion indicates its volumetric water content α_l.

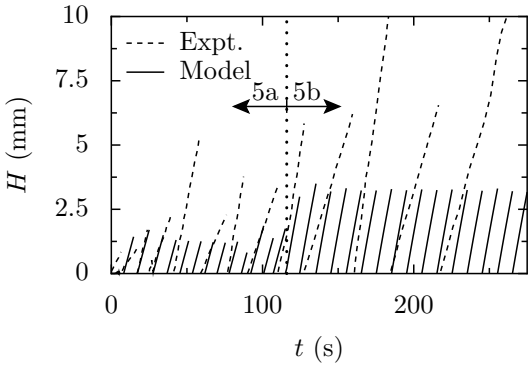

Figure 5.14: Thickness of the accretion at the leading edge for case 5a and 5b.

growth model. While the length of the predicted accretion cycles is in fair agreement with experimental data, the icing behavior and the influence of the additional water injection is correctly reproduced.

Well-adhered ice accretion In the experiments corresponding to case 6 and 7 of Table 5.4, the ice accretion was well-adhered to the airfoil and did not shed during the observation time. These two experiments were performed at a wet-bulb temperature below freezing, as a result, only the heat conduction of the airfoil is able to melt and loosen the accretion. Figure 5.15 shows a comparison of the accretion composition between case 4 and 6, 42 s after the start of a uniform length accretion cycle. The accretion of case 6 contains significantly less liquid water and is therefore better adhered to the surface than the one of case 4. No melting from the outside of the accretion takes place in case 6 and 7 as $\vartheta_{\mathrm{wb}} < 0\,^{\circ}\mathrm{C}$. However, the conductive heat flux in the airfoil is still present and will lead to shedding eventually. In the numerical simulation, shedding of the uniform length accretion occurred after 183 and 103 s in case 6 and 7, respectively. The rather long time it takes the accretion to shed indicates that it is well-adhered, which is in good agreement with experimental data.

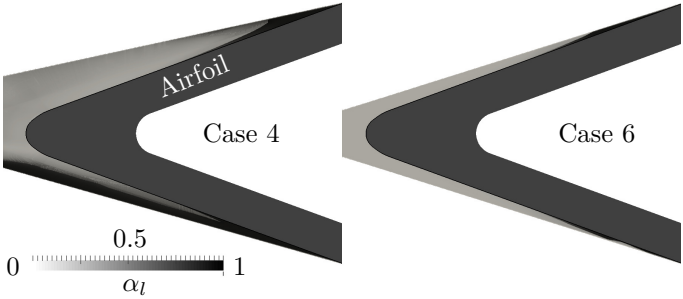

Figure 5.15: Comparison of the composition of the leading edge ice accretion between case 4 and 6, 42 s after the start of the accretion cycle.

Anti-icing In experiments performed at the Cox Icing wind tunnel (Al-Khalil et al., 2003, Miller et al., 1997), the leading edge of a NACA0012 airfoil has been equipped with seven heaters which are operated separately. In the considered experiments, they are switched on if the temperature on the corresponding surface drops below 4.4 and switched off above 10 °C. Maintaining this surface temperature ensures running-wet conditions, i.e. impinging ice is melted before accretion can occur. Neither in the experiments nor in the numerical simulations ice accretion of significant thickness were observed with this heater configuration. Yet, a thin layer of ice accretes and quickly melts and therefore sheds at a high frequency. Its melting behavior, which deviates from the melting of solid ice, determines how much heat is needed to maintain the surface temperature interval associated with running-wet anti-icing conditions. The experimental airfoil consists of five different layers, in the simulation only the ones between the heating element and the surface are considered. Thickness and material properties are given by Miller et al. (1997). As the ambient temperature is very low, the difference between temperature and wet-bulb temperature is rather low. For this reason, these temperatures are equalized for the computation of cases 8 and 9 of Table 5.5.

Figures 5.16 and 5.17 show the required mean heater power of each heater for case 8 and 9. Circles correspond to wind tunnel measurements while crosses denote numerically calculated values. Heater 4 is located at the leading edge of the airfoil while heaters 1–3 and 5–7 are placed

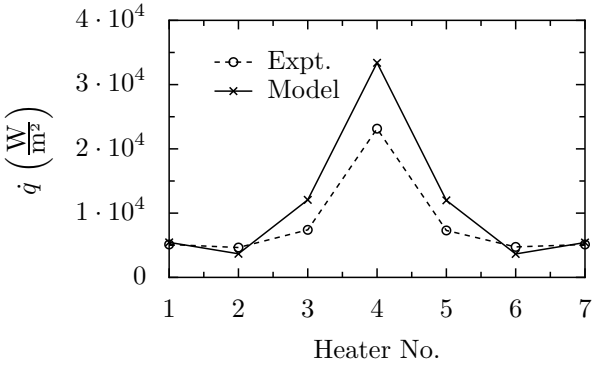

Figure 5.16: Required heater power for case 8 at the seven individual heater zones to maintain the specified temperature on the leading edge of the NACA0012.

next to it on each side of the airfoil. Most heater power is required at the leading edge as the accretion growth rate is the largest in this region. Nearly no ice accreted at the rear most heaters (heater 1 and 7), where mostly convective cooling is compensated by the heaters. The agreement between numerical predictions and experimental data is rather good.

5.3.3 Parametric study on the influence of model parameters

A parametric study is carried out to quantify the effect different model parameters have on the icing severity. Investigated are the initial particle size, the moisture transfer coefficient and the heat transfer on the accretion surface. Based on case 5b of table 5.4, their influence on the maximum accretion thickness $\hat{H}$, which occurs before the shedding and is a measure for the icing severity, is investigated by multiplying it by an enhancement factor ξ.

Any influence varying these values might have on the growth rate, e.g. by an improvement of the sticking behavior on a wetter accretion or impact dynamics of particles of varying size, are neglected in the scope of this parameter study.

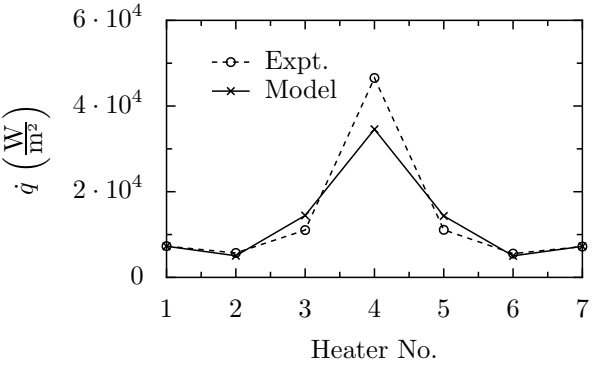

Figure 5.17: Heater power for case 9.

Influence of initial particle size As described in section 5.3.1.1, the thickness of the thermal boundary layer depends linearly on the initial radius of the particles. Thus, a larger amount of ice has to be melted to clear the airfoil's surface from ice to reach the shedding criterion if the initial particle radius is increased. Figure 5.18 shows the maximum ice thickness $\hat{H}$ (crosses) over the enhancement factor ξ which is used to modify the value used as initial particle radius, i.e. $\xi = 1$ corresponds to the reference case 5b. As the initial particle radius is increased, the shedding thickness increases linearly. This is due to the fact that while keeping all other parameters and thus the heat fluxes constant, more ice needs to be melted in order to clear the airfoil surface. Therefore, it takes longer to reach the shedding criterion which enables longer accretion growth resulting in thicker ice layers. The dashed line corresponds to an extrapolation using the mean slope to an initial particle radius of zero. In this case, the thermal boundary thickness is zero resulting in a sharp interface as assumed in the classical Stefan problem. As a result, the maximum layer thickness is decreased to 44 % of the reference value. This proves the significance of accounting for the heat conduction in the pores and the importance of the particle size.

Effect of surface roughness enhanced heat transfer The heat transfer coefficients computed in section 5.3.2.2 correspond to the heat transfer of a smooth wall to a surrounding flow. Surface roughness increases the convective heat and mass fluxes by inducing higher levels of turbulence

(Walker et al., 2014) and increasing the surface area available for the heat transfer. In order to quantify the effect the surface roughness increased heat and mass transfer has on the icing severity, a parameter study is carried out. In this investigation, the heat and mass transfer at the surface of the ice accretion is multiplied by the enhancement factor ξ while the heat transfer at the non-wetted parts remains as computed for a smooth surface. Figure 5.18 shows the maximum ice thickness $\hat{H}$ over the heat transfer enhancement factor (circles). A variation of the heat and mass transfer affects the initial composition of the accretion layer. At increasing ξ, less ice needs to be melted to loosen the accretion and therefore the ice sheds earlier at lower thickness reducing the icing severity. An increasing heat transfer has a significant influence on the icing behavior and severity.

Influence of moisture transfer coefficient The influence of imbibition is analyzed by varying the moisture transfer coefficient by multiplying it by ξ for the computation of reference case 5b. Figure 5.18 shows the shedding ice layer thickness over the enhancement factor for the moisture transfer coefficient. For $a = 0$, i.e. no water imbibition, the maximum ice thickness is 7 % higher than for the reference case ($\xi = 1$). Increasing the moisture transfer coefficient further decreases $\hat{H}$ slightly while the greatest influence occurs at $\xi < 0.25$. This means that switching the imbibtion on has an effect on the icing severity while the value of the moisture transfer coefficient only has little influence if it is above a certain value. Even though the imbibition has only little influence on the melting of the ice at the surface of the airfoil, it significantly influences the composition of the accretion, i.e. its wetness. This parameter has a crucial impact on the sticking efficiency and therefore on the growth rate of the accretion. Since the altered sticking behavior of the impacting particles is not accounted for in the present study, the influence of the imbibition is expected to be more significant than indicated in Fig. 5.18.

5.4 Conclusions

A theoretical model for the prediction of the melting of wet granular materials is presented. It takes into account the heat conduction in the phase which does not change its phase. From a dimensional analysis in combination with numerical investigations it has been found that it only depends on the particle size and composition of the layer. A theoretical

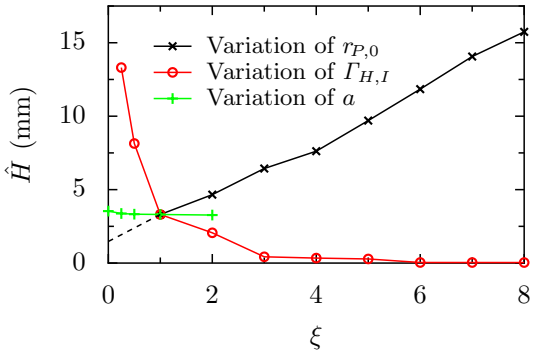

Figure 5.18: Ice layer thickness at shedding instant $\hat{H}$ over enhancement factor for the initial particle radius (crosses), for the heat and mass transfer coefficients at the accretion surface (circles) and for the moisture transfer coefficient (plusses).

model describing this correlation is derived. Also, the imbibition of the liquid into the solid granular structure and the accompanying convective heat transfer are modeled as proposed by Luikov (1966) and advanced for high moisture contents, which is necessary for this application.

A combination of the derived equations with an existing ice growth model is implemented in the framework of a Finite-Volume code. It allows the computation of available ice accretion experiments. The code is able to predict whether the accretion regularly sheds from the surface, is well-adhered, or no icing occurs. Computed shedding events are in good agreement with experimental observations. Moreover, the required power for anti-icing has been predicted with rather good accuracy.

The presented results are based on many simplifying assumptions and neglects. Taking into account the particle trajectories before accreting, considering the dissipative heating and accounting for various ice particle sizes and shapes are just some possibilities to improve the performance of the model. Moreover, the layer's composition influences its "hardness" and hence the particle sticking behavior. Therefore, predictions of the layer composition made by this model potentially improve the anticipation whether particles stick to the surface or ricochet and hence the sticking efficiency which is a very important parameter for accretion growth models. Only shedding of the accretion as a whole, based on the

connection strength, has been looked at in this work. More precise results could be obtained by consideration of the forces acting on the accretion, associated with adhesive, cohesive and aerodynamic stresses. Accounting for partial shedding, as occurred in some of the experiments, and breakup of the accretion depending on its composition could help further improve the prediction of the icing severity.

6 Conclusions and outlook

Three major aspects of ice particle accretion in warm environments were investigated: Melting of particles on their way through the engine, impingement on a liquid surface and accretion and shedding of porous ice layers. Each subprocess has been investigated by means of experiments at hand, theoretical modeling and numerical computations and is presented in the framework of this thesis. Significant insights into physical mechanisms are revealed and improvements over currently employed models and methods are presented.

Melting of non-spherical ice particles Typical phenomena, associated with the melting of non-spherical particles, are observed in experiments. These are the capillary driven collection of the meltwater in the particle mid-section, where the solid surface curvature is the lowest, the formation of sharp cusps and the smoothing of surface irregularities. A model which accounts for these effects and assumes the particle to be spheroidal before the onset of melting is developed and numerically realized using a Level-Set method. In this model, the heat transfer coefficient of a volume equivalent sphere is used to calculate the heat flux which is assumed to be evenly distributed over the surface of the non-spherical particle. With increasing particle aspect ratio, the deviation in terms of melting times and melt ratio between the prediction of the simple 1D sphere model and the spheroid model rises. A comparison between experimental data of the melting experiments and results obtained with the novel model exhibits very good agreement and an improvement of the prediction of the melting time over the 1D sphere model of over 50 %; the mean maximum deviation between the models in terms of melt ratio was > 20 %. Since the icing severity is highly sensitive to the particle melt ratio, this has a crucial effect on the accuracy of the prediction of ice accretion.
Even more precise results could be achieved by using a more appropriate Nusselt correlation to obtain a heat transfer coefficient which better accounts for the particle shape. Either by using a Nusselt correlation which is capable of describing the local heat transfer coefficient or coupling

the model with a flow solver in the gaseous phase could yield more precise, local heat and mass transfers. From the obtained local heat inputs local melting velocities could be obtained which would describe the particle shape evolution more precisely. Moreover, the approach could be advanced for the computation of initial particle shapes other than the spheroidal one, e.g. cylinders, prisms or irregular particles.

Particle impingement In the scope of this investigation, an algorithm for the impact of a spherical particle on a free liquid surface is developed. It is able to compute inclined impact processes with particle rotation and takes into account the wettability of the particle surface by means of a constant or dynamic contact angle model. A mesh motion is introduced to move the particle which constitutes a boundary on the domain while the interface between liquid and gaseous phase is taken into account by means of a VOF approach. The capillary force arising at the three phase CL is modeled in the VOF framework and has a vital effect on the outcome of the computation of the particle impact at low Weber numbers which are commonly encountered in ice crystal accretion. It is shown that the wettability affects the water entry of the impacting bodies either at low Weber numbers or if the particle rotates at high angular velocities. The impact process is mostly influenced by the Weber number, the wettability and the ratio of solid to liquid density, if the Weber number is small. Since the wettability and density ratio is constant when looking at a fixed material pairing which is considered in ice crystal accretion, only the Weber number determines whether particles stick to the interface or rebound. A simple correlation for the penetration depth and the limit for interface breaching is found. By means of this equation, the outcome of the impact process can be efficiently predicted which governs the growth rate of an ice accretion. Therefore, it constitutes a first step away from currently employed empirical equations towards a more precise physics-based description.
Only the impact of spherical bodies has been investigated in this work. As the particle shape and its orientation upon impact probably have a considerable influence on the impact process, this should be addressed in future studies as well as enabling the motion in more than three degrees of freedom. In addition to that, accounting for secondary processes, e.g. particle shattering or the impact and rebound of the particle from the solid wall underneath the liquid film, could further improve the precision of the forecast of the impact outcome.

Accretion and shedding of porous ice/water layers As the connection strength and the sticking of incoming particles principally depend on the accretion composition, it plays a central role in the growth of the ice/water layer and the accretion behavior, i.e. whether the accretion is rather loosely attached, well-adhered or no ice accretes at all. The computation of the composition is approached in two steps: A detailed numerical investigation, in which individual ice crystals and liquid droplets are resolved is used in the first approach while the behavior of a melting porous ice accretion is modeled in the second approach.
At first, a detailed numerical model is developed taking into account melting/solidifying within the layer, convective heat and mass transfer to the surrounding airflow and heat conduction in the substrate on which the layer accumulates. Shedding of the accretion is assumed if a liquid film separating the accretion from the wall is present. Available icing experiments are well reproduced and explained by means of this model and thermal icing limits for severe icing are found and in very good agreement with experimental data. Anyhow, the need for resolving the particles and droplets in the numerical grid renders this method rather computation costly. As a result, only a small part of the airfoil is considered in this approach as a simulation of the icing of an entire airfoil would not be economically feasible.
To make such a computation possible, the effective thermal properties of a porous ice/water layer are analyzed and theoretically modeled in the second approach. This model accounts for the heat conduction in the liquid phase which effectively smears the interface region. Also, the imbibition of liquid water into the pores of the accretion by capillary suction and convective heat transport associated with it are considered. The model is implemented in a Finite-Volume code and combined with an available growth model to compute ice accretion on an airfoil. Local heat transfer coefficients are computed in advance, their application yields a heat flux which constitutes the boundary condition on the surface of the accretion and the clean airfoil. Heat conduction is accounted for as well as evaporative mass transfer to the surrounding airflow. Obtained results agree very well with available icing experiments in terms of icing behavior and shedding of the accretion. The model is the first of its kind to compute the accretion composition and thereby deduce shedding.
Despite the good results, this approach is still based on many simplifying assumption which limits its accuracy and exhibits space for further improvements. The fidelity of current growth models is rather limited

as it is a field of ongoing research. Its improvement, e.g. by taking into account the layer composition at the impact site provided by the presented model, could help to improve the quality of the results significantly. For the smearing of the interface, the particles are assumed to be spherical. Accounting for the particle non-sphericity could positively affect the outcome of the computations. Only water transport, which is due to capillary suction, has been accounted in this work. Considering pressure gradient induced or shear driven water motion could help modeling the runback of water along the surface of the airfoil which influences the convective heat input. Furthermore, the value of the moisture transfer coefficient which governs the imbibition velocity is oriented on values for similar materials like gypsum or gas concrete. Lacking an exact value, this is nothing more than an educated guess, hence, an investigation of capillary suction in porous ice layers to define a more precise moisture transfer coefficient could improve the results. Accounting for the imbibition is based on the assumptions that the volume of the mass fraction is evenly distributed and the capillary water migration is slower than the melting. Although these assumptions are valid for most icing cases, advancing the model for the general case might have a positive influence on the results. Only shedding of the accretion as a whole, based on the connection strength, has been looked at in this thesis. More precise results could be obtained by considering the forces acting on the accretion associated wit adhesive, cohesive and aerodynamic stresses. Accounting for partial shedding, as occurred in some of the experiments, and breakup of the accretion depending on its composition could help improve the prediction of the icing severity and the effect shedding has on the downstream components of the engine.

Significant progress has been made within the scope of this work in all of the three subprocesses. Developed models and algorithms presented in this work are a significant step towards a new generation of predictive tools for ice crystal accretion. The development of such tools is a crucial milestone on the way towards safer and more economic air traffic.

A Material properties

This chapter describes the treatment of non-constant material properties in this work. Equations and formulas describing these are presented and assumptions made by the author are explained.

A.1 Properties of air

Saturation pressure The saturation vapor pressure depends strongly on the Temperature. Above an ice surface, i.e. for $T < T_m$, it is well described by the equation by Wagner et al. (1994)

$$p_{\mathrm{sat}}(T) = \exp[A(1-(T/T_f)^{-1.5}) + B(1-(T/T_f)^{-1.25})] \cdot C, \qquad \text{(A.1)}$$

which is valid for 233.15 K $< T <$ T_m. It yields the saturation pressure p_{sat} for $A = -13.9281690$, $B = 34.7078238$, $C = 611.657$ Pa, $T_f = 273.16$ K. At temperatures above the melting temperature, the formula given in Yaws (2008) is used

$$\log 10\left(\frac{p_{\mathrm{sat}}(T)}{A}\right) = B - \frac{C}{T - T_m + T_f}, \qquad \text{(A.2)}$$

where $A = 133.332$ Pa, $B = 8.05573$, $C = 1723.6425$ K and $T_f = 233.08$ K. It is valid for 273.16K $< T <$ 647.13K.

Figure A.1 shows the saturation pressure over the temperature given by Eqs. (A.1) and (A.2) as solid lines, each for its applicable temperature range. Circles correspond to tabulated data presented by Feistel and Wagner (2007), for temperatures below T_m, and provided by Koch et al. (2013) for temperatures above the melting point.

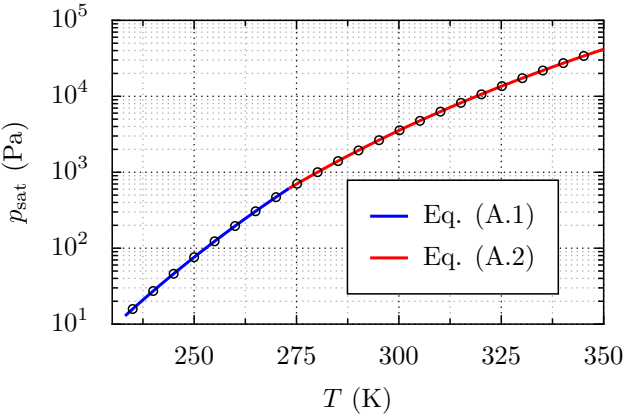

Figure A.1: Saturation pressure over temperature as given by Eq. (A.1) shown as blue line and by Eq. (A.2) as red line.

Thermal conductivity of air The thermal conductivity of air is approximated (Yaws, 2008) by

$$k_A(T) = A + BT + CT^2 + DT^3, \tag{A.3}$$

in the range 100 K $< T <$ 1500 K. In this equation, the constants are $A = -3.8603 \cdot 10^{-4}$, $B = 1.0311 \cdot 10^{-4}$, $C = -5.4199 \cdot 10^{-8}$ and $D = 1.7429 \cdot 10^{-11}$. It yields the thermal conductivity in W/(m K).

Viscosity A formula for the dynamic viscosity, valid for $233.15 < T < 373.15$, is presented in VDI-Gesellschaft Verfahrenstechnik und Chemieingenierwesen (GVC) (2005). Combining it with the ideal gas equation yields a formula for the kinematic viscosity as a function of temperature and pressure

$$\nu(T, p) = (A + BT + CT^2)\frac{RT}{p}, \tag{A.4}$$

where $A = -0.03287 \cdot 10^{-5}$, $B = 0.77996 \cdot 10^{-7}$ and $C = 0.48801 \cdot 10^{-10}$.

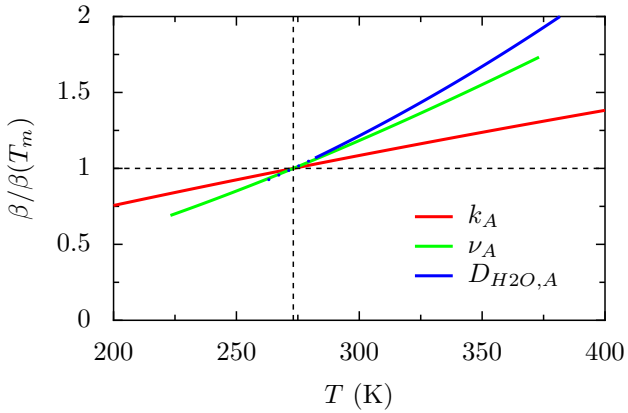

Figure A.2: Thermal conductivity, kinematic viscosity of air and diffusivity of water vapor in air at an ambient pressure of 1 bar.

Diffusivity Lienhard IV and Lienhard V (2008) present an equation for the diffusivity of water vapor in air. It reads

$$D(T,p) = 1.87 \cdot 10^{-5} \frac{T^{2.072}}{p}. \tag{A.5}$$

It is valid from 282 – 450 K and yields the diffusivity in m^2/s. In this work, the equation has been extrapolated slightly if the relevant temperatures were below the given range, depicted in Fig. A.2 as dotted line.

Figure A.2 shows the thermal conductivity, kinematic viscosity of air and the diffusivity of water vapor in air over the temperature at a pressure of $p = 1$ bar. Each graph is non-dimensionalized with the property value at T_m, the dashed black line corresponds to the reference point at $T = T_m$.

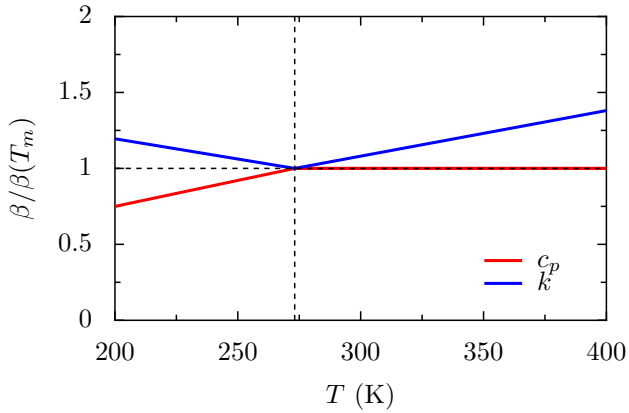

Figure A.3: Heat capacity and thermal conductivity of ice and liquid water over the temperature.

A.2 Material properties of water

Thermal conductivity The thermal conductivity is well described (Alexiades, 1992) by

$$k_I(T) = 2.24 + 5.975 \cdot 10^{-3}(T_m - T)^{1.156} \quad \text{and} \tag{A.6}$$

$$k_W(T) = 0.1017 + 1.695 \cdot 10^{-3}T, \tag{A.7}$$

for ice and water, respectively. Their heat capacities is given by

$$c_{p,I}(T) = 7.16T + 138 \quad \text{and} \tag{A.8}$$

$$c_{p,W}(T) = 4186. \tag{A.9}$$

Figure A.3 shows the thermal conductivity and heat capacity of ice and water over the temperature non-dimensionalized with the value at T_m, dashed black lines correspond to the point of reference.

Since mostly mixed phase conditions and temperatures close to the melting point are considered in this work, the temperature-dependency of

the heat capacity and thermal conductivity of the liquid and solid water are neglected; constant values are used for the computations.

Bibliography

M. Ahmadzadeh, B. Saranjam, A. Hoseini Fard, and A. R. Binesh. Numerical simulation of sphere water entry problem using Eulerian-Lagrangian method. *Appl. Math. Model.*, 38:1673–1684, 2014.

K. Al-Khalil, E. Irani, and D. Miller. Mixed Phase Icing Simulation and Testing at the Cox Icing Wind Tunnel. In *41st AIAA Aerospace Sciences Meeting And Exhibit*, number AIAA-2003-0903, 2003.

V. Alexiades. *Mathematical modeling of melting and freezing processes*. Hemisphere Publishing Corporation, Washington, D.C., 1992.

K. Aoki, M. Hattori, and T. Ujiie. Snow melting by heating from the bottom surface. *JSME Int. J.*, 31(2):269–275, 1988.

J. M. Aristoff and J. W. M. Bush. Water entry of small hydrophobic spheres. *J. Fluid Mech.*, 619:45–78, 2009.

J. M. Aristoff, T. T. Truscott, A. H. Techet, and J. W. M. Bush. The water entry of decelerating spheres. *Phys. Fluids*, 22(032102), 2010.

H. Attar, M. Bönisch, M. Calin, L.-C. Zhang, S. Scudino, and J. Eckert. Selective laser melting of in situ titanium–titanium boride composites: Processing, microstructure and mechanical properties. *Acta Mater.*, 76: 13–22, 2014.

V. Ayel, O. Lottin, and H. Peerhossaini. Rheology, flow behaviour and heat transfer of ice slurries: a review of the state of the art. *Int. J. Refrig.*, 26(1):95–107, 2003.

J. M. Back, S. W. McCue, and T. J. Moroney. Including nonequilibrium interface kinetics in a continuum model for melting nanoscaled particles. *Sci. rep.*, 4, 2014.

I. H. Bailey and W. C. Macklin. The surface configuration and internal structure of artificial hailstones. *Q. J. Roy. Meteor. Soc.*, 94(399):1–11, 1968.

H. M. Barkla and L. J. Auchterlonie. The Magnus or Robins effect on rotating spheres. *J. Fluid Mech.*, 47:437–447, 1971.

R. S. Berry, J. Jellinek, and G. Natanson. Melting of clusters and melting. *Phys. Rev. A*, 30(2):919, 1984.

P. A. Berthelsen. A short introduction to the level set method and incompressible Two-Phase Flow: A Computational Approach. *NTNU Report, Norway*, 2002.

Y. Bourgault, H. Beaugendre, and W. G. Habashi. Development of a shallow-water icing model in FENSAP-ICE. *J. Aircraft*, 37(4):640–646, 2000.

J. U. Brackbill, D. B. Kothe, and C. Zemach. A continuum method for modeling surface tension. *J. Comput. Phys.*, 100(2):335–354, 1992.

T. W. Brakel, J. P. F. Charpin, and T. G. Myers. One-dimensional ice growth due to incoming supercooled droplets impacting on a thin conducting substrate. *Int. J. Heat Mass Tran.*, 50(9):1694–1705, 2007.

R. A. Brewster, S. Frik, and F. Werner. Computational analysis of automotive windshield de-icing with comparison to test data. Technical Report 971833, 1997.

J. T. Cansdale and R. W. Gent. Ice Accretion on Aerofoils in Two-Dimensional Compressible Flow-A Theoretical Model. Technical Report 82128, Royal Aircraft Establishment, 1983.

H. S. Carslaw, J. C. Jaeger, et al. *Conduction of Heat in Solids*. Oxford University Press, Oxford, U.K., 1959.

R. Chandramouli, T. K. Kandavel, and P. Karthikeyan. Experimental investigations on welding behaviour of sintered and forged Fe–0.3% C–3% Mo low alloy steel. *Mater. Design*, 53:645–650, 2014.

Y.-C. Chang, T. Y. Hou, B. Merriman, and S. Osher. A level set formulation of Eulerian interface capturing methods for incompressible fluid flows. *J. Comput. Phys.*, 124(2):449–464, 1996.

C. I. Christov and P. K. Volkov. Numerical investigation of the steady viscous flow past a stationary deformable bubble. *J. Fluid Mech.*, 158: 341–364, 1985.

R. Clift and W. H. Gauvin. In *Proc. CHEMECA '70*, volume 1, pages 14–28. Butterworth, Melbourne, 1970.

E. O. Correa, S. C. Costa, and J. N. Santos. Weldability of iron-based powder metal materials using pulsed plasma arc welding process. *J. Mater. Process. Tech.*, 198(1):323–329, 2008.

T. C. Currie and D. Fuleki. Development and Application of an Impedance-Based Instrument for Measuring the Liquid Fraction and Thickness of Ice Crystal Accretions. Number 2015-01-2134. SAE Technical Paper, 2015.

T. C. Currie, P. M. Struk, J.-C. Tsao, D. Fuleki, and D. C. Knezevici. Fundamental Study of Mixed-Phase Icing with Application to Ice Crystal Accretion in Aircraft Jet Engines. In *4th AIAA Atmospheric and Space Environments Conference*, number AIAA 2012-3035, 2012.

T. C. Currie, D. Fuleki, D. C. Knezevici, and J. D. MacLeod. Altitude Scaling of Ice Crystal Accretion. In *5th AIAA Atmospheric and Space Environments Conference*, number AIAA 2013-2677, 2013.

T. C. Currie, D. M. Fuleki, and A. Mahallati. Experimental Studies of Mixed-Phase Sticking Efficiency for Ice Crystal Accretion in Jet Engines. In *6th AIAA Atmospheric and Space Environments Conference, American Institute of Aeronautics and Astronautics, Reston, VA*, number AIAA 2014-3049, 2014.

T. C. Currie, D. Fuleki, and C. Davison. Simulation of Ice Particle Melting in the NRCC RATFac Mixed-Phase Icing Tunnel. Number 2015-01-2107. SAE Technical Paper, 2015.

G. B. Davis and J. M. Hill. A moving boundary problem for the sphere. *IMA J. Appl. Math.*, 29(1):99–111, 1982.

S. S. Deshpande, L. Anumolu, and M. F. Trujillo. Evaluating the performance of the two-phase flow solver interFoam. *Comput. Sci. Discov.*, 5(1):014016, 2012.

M. Do-Quang and G. Amberg. The splash of a solid sphere impacting on a liquid surface: Numerical simulation of the influence of wetting. *Phys. Fluids*, 21(2):022102, 2009.

S. S. Dosanjh. Melting and refreezing of porous media. *Int. J. Heat Fluid Fl.*, 10(4):301–310, 1989.

Q. Duan, F. L. Tan, and K. C. Leong. A numerical study of solidification of n-hexadecane based on the enthalpy formulation. *J. Mater. Process. Tech.*, 120(1):249–258, 2002.

C. Duez, C. Ybert, C. Clanet, and L. Bocquet. Making a splash with water repellency. *Nature Phys.*, 3:180–183, 2007.

G. Dupeux, A. Le Goff, D. Quéré, and C. Clanet. The spinning ball spiral. *N. J. Phys.*, 12(093004), 2010.

Y. Dutil, D. R. Rousse, N. B. Salah, S. Lassue, and L. Zalewski. A review on phase-change materials: mathematical modeling and simulations. *Renew. Sust. Energ. Rev.*, 15(1):112–130, 2011.

P. W. Egolf, A. Kitanovski, D. Ata-Caesar, E. Stamatiou, M. Kawaji, J.-P. Bedecarrats, and F. Strub. Thermodynamics and heat transfer of ice slurries. *Int. J. Refrig.*, 28(1):51–59, 2005.

R. Feistel and W. Wagner. Sublimation pressure and sublimation enthalpy of H2O ice Ih between 0 and 273.16 K. *Geochim. Cosmochim. Ac.*, 71 (1):36–45, 2007.

W. Feller. *An introduction to probability theory and its applications*, volume 1. John Wiley & Sons, 2008.

A. A. Ferrara and G. Yenetchi. Prevention of Preferential Bridge Icing Using Heat Pipes. Technical Report FHWA-RA-75-111, Washington, D.C. Federal Highway Administration, 1975.

J. H. Ferziger and M. Peric. *Computational methods for fluid dynamics*. Springer Science & Business Media, 2012.

R. M. Fillion, A. R. Riahi, and A. Edrisy. A review of icing prevention in photovoltaic devices by surface engineering. *Renew. Sust. Energ. Rev.*, 32:797–809, 2014.

N. Fukuta, R. C. Savage, G. J. Donovan, and C. M. Liu. The microphysics of snow crystal and snow flake melting. Technical Report AFGL-TR-83-0066, University of Utah, 1982.

Y. Furukawa and J. S. Wettlaufer. Snow and ice crystals. *Phys. Today*, 60(12):70–71, 2007.

D. E. Fyfe, E. S. Oran, and M. J. Fritts. Surface tension and viscosity with Lagrangian hydrodynamics on a triangular mesh. *J. Comput. Phys.*, 76 (2):349–384, 1988.

H. Gan, J. J. Feng, and H. H. Hu. Simulation of the sedimentation of melting solid particles. *Int. J. Multiphas. Flow*, 29(5):751–769, 2003.

R. W. Gent, N. P. Dart, and J. T. Cansdale. Aircraft icing. *Proc. R. Soc. Lond. A*, 358(1776):2873–2911, 2000.

T. A. Griffin, D. J. Dicki, and P. J. Lizanich. PSL Icing Facility Upgrade Overview. In *6th Atmospheric and Space Environments Conference, American Institute of Aeronautics and Astronautics, Reston, VA*, number AIAA 2014-2896, 2014.

S. Gu and S. Kamnis. Numerical modelling of in-flight particle dynamics of non-spherical powder. *Surf. Coat. Technol.*, 203(22):3485–3490, 2009.

K. L. S. Gunn and J. S. Marshall. The distribution with size of aggregate snowflakes. *J. Meteor.*, 15(5):452–461, 1958.

W. Habashi and S. Nilamdeen. Multiphase Approach Toward Simulating Ice Crystal Ingestion in Jet Engines. *J. Propul. Power*, 27(5):959–969, 2011.

J. He, M. Ice, and E. Lavernia. Particle melting behavior during high-velocity oxygen fuel thermal spraying. *J. Therm. Spray Techn.*, 10(1):83–93, 2001.

M. A. Herrero and J. J. L. Velázquez. On the melting of ice balls. *SIAM J. Math. Anal.*, 28(1):1–32, 1997.

A. J. Heymsfield, A. Bansemer, P. R. Field, S. L. Durden, J. L. Stith, J. E. Dye, W. Hall, and C. A. Grainger. Observations and parameterizations of particle size distributions in deep tropical cirrus and stratiform precipitating clouds: Results from in situ observations in TRMM field campaigns. *J. Atmos. Sci.*, 59(24):3457–3491, 2002.

J. M. Hill and A. Kucera. The time to complete reaction or solidification of a sphere. *Chem. Eng. Sci.*, 38(8):1360–1362, 1983.

C. W. Hirt and B. D. Nichols. Volume of fluid (VOF) method for the dynamics of free boundaries. *J. Comput. Phys.*, 39(1):201–225, 1981.

C. W. Hirt, A. A. Amsden, and J. L. Cook. An arbitrary Lagrangian-Eulerian computing method for all flow speeds. *J. Comput. Phys.*, 14(3):227–253, 1974.

R. L. Hoffman. A study of the advancing interface. I. Interface shape in liquid-gas systems. *J. Colloid Interf. Sci.*, 50:228–241, 1975.

S. D. Howison, J. R. Ockendon, and A. A. Lacey. Singularity development in moving-boundary problems. *Quart. J. Mech. Appl. Math.*, 38(3): 343–360, 1985.

H. Iwamori. A model for disequilibrium mantle melting incorporating melt transport by porous and channel flows. *Nature*, pages 734–737, 1993.

A. Jafari and N. Ashgriz. *Numerical Techniques for Free Surface Flows: Interface Capturing and InterfaceTracking*, pages 1494–1513. Springer, 2008.

W. J. Jasinski, S. C. Noe, M. S. Selig, and M. B. Bragg. Wind turbine performance under icing conditions. *J. Sol. Energ.*, 120(1):60–65, 1998.

V. Jomelli and P. Bertran. Wet snow avalanche deposits in the French Alps: structure and sedimentology. *Geogr. Ann. A.*, 83(1-2):15–28, 2001.

C. Josserand and S. Zaleski. Droplet splashing on a thin liquid film. *Phys. Fluids*, 15:1650–1657, 2003.

D. M. Kintea, T. Hauk, J. Breitenbach, I. V. Roisman, and C. Tropea. Oblique water entry of rigid spheres. In *ILASS – Europe 2014, 26th Annual Conference on Liquid Atomization and Spray Systems*, Bremen, Germany, 8 - 10 September 2014a.

D. M. Kintea, M. Schremb, I. V. Roisman, and C. Tropea. Numerical investigation of ice particle accretion on heated surfaces with application to aircraft engines. In *11th AIAA/ASME Joint Thermophysics and Heat Transfer Conference, American Institute of Aeronautics and Astronautics, Reston, VA*, number AIAA 2014-2820, 2014b.

D. M. Kintea, T. Hauk, I. V. Roisman, and C. Tropea. Melting of non-spherical particles. In *ICLASS – 2015, 13th Triennial International*

Conference on Liquid Atomization and Spray Systems, Tainan, Taiwan, 23 - 27 August 2015a.

D. M. Kintea, T. Hauk, I. V. Roisman, and C. Tropea. Shape evolution of a melting nonspherical particle. *Phys. Rev. E*, 92(3):033012, 2015b.

D. M. Kintea, V. Thammanna Gurumurthy, I. V. Roisman, and C. Tropea. On particle impact on a free liquid surface at low Weber numbers. In *ICLASS – 2015, 13th Triennial International Conference on Liquid Atomization and Spray Systems*, Tainan, Taiwan, 23 - 27 August 2015c.

D. M. Kintea, J. Breitenbach, V. Thammanna Gurumurthy, I. V. Roisman, and C. Tropea. On the influence of surface tension during the impact of particles on a liquid-gaseous interface. *Phys. Fluids*, 28 (012108), 2016a.

D. M. Kintea, I. V. Roisman, and C. Tropea. Transport processes in a wet granular ice layer: model for ice accretion and shedding. *Int. J. Heat Mass Tran.*, 97:461–472, 2016b.

S. F. Kistler. Hydrodynamics of wetting. In J. C. Berg, editor, *Wettability*. Marcel Dekker, New York, 1993.

A. Kitanovski, D. Vuarnoz, D. Ata-Caesar, P. W. Egolf, T. M. Hansen, and C. Doetsch. The fluid dynamics of ice slurry. *Int. J. Refrig.*, 28(1): 37–50, 2005.

C. A. Knight. The contact angle of water on ice. *J. Colloid Interf. Sci.*, 25(2):280–284, 1967.

C. A. Knight. Observations of the morphology of melting snow. *J. Atmos. Sci.*, 36(6):1123–1130, 1979.

W. Koch et al. *VDI-Wasserdampftafeln*. Springer-Verlag, 2013.

C. Konrad, Y. Zhang, and Y. Shi. Melting and resolidification of a subcooled metal powder particle subjected to nanosecond laser heating. *Int. J. Heat. Mass Tran.*, 50(11):2236–2245, 2007.

T. Kray, J. Franke, and W. Frank. Magnus effect on a rotating sphere at high Reynolds numbers. *J. Wind Eng. Ind. Aerod.*, 110:1–9, 2012.

F. Kreith and F. E. Romie. A study of the thermal diffusion equation with boundary conditions corresponding to solidification or melting of materials initially at the fusion temperature. *Proc. R. Soc. B*, 68(5): 277, 1955.

J.-P. Kruth, L. Froyen, J. Van Vaerenbergh, P. Mercelis, M. Rombouts, and B. Lauwers. Selective laser melting of iron-based powder. *J. Mater. Process. Tech.*, 149(1):616–622, 2004.

J. L. Laforte, M. A. Allaire, and J. Laflamme. State-of-the-art on power line de-icing. *Atmos. Res.*, 46(1):143–158, 1998.

A. E. Larsen and D. G. Grier. Melting of metastable crystallites in charge-stabilized colloidal suspensions. *Phys. Rev. Lett.*, 76(20):3862, 1996.

D.-G. Lee and H.-Y. Kim. Impact of a Superhydrophobic Sphere onto Water. *Langmuir*, 24:142–145, 2008.

J. H. Lienhard IV and J. H. Lienhard V. *A heat transfer textbook*. Phlogiston Press, Cambridge, Massachusetts, USA, 2008.

F. Ling and T. Zhang. Numerical simulation of permafrost thermal regime and talik development under shallow thaw lakes on the Alaskan Arctic Coastal Plain. *J. Geophys. Res.*, 108(D16):4511, 2003.

X. Liu, S. J. Rees, and J. D. Spitler. Modeling snow melting on heated pavement surfaces. Part I: Model development. *Appl. Therm. Eng.*, 27 (5):1115–1124, 2007.

A. L. London and R. A. Seban. Rate of ice formation. *Trans. ASME*, 65 (7):771–779, 1943.

C. D. Lorenz and R. M. Ziff. Precise determination of the critical percolation threshold for the three-dimensional "Swiss cheese" model using a growth algorithm. *J. Chem. Phys.*, 114(8):3659–3661, 2001.

A. V. Luikov. *Heat and Mass Transfer in Capillary-porous Bodies*. Pergamon Press, Oxford, 1966.

J. D. MacLeod. Development of Ice Crystal Facilities for Engine Testing. Number 2007-01-3290. SAE Technical Paper, 2007.

B. J. Mason. On the melting of hailstones. *Q. J. Roy. Meteor. Soc.*, 82 (352):209–216, 1956.

J. G. Mason, J. W. Strapp, and P. Chow. The ice particle threat to engines in flight. In *44th AIAA Aerospace Sciences Meeting*, volume 4, pages 2445–2465, 2006.

J. G. Mason, P. Chow, and D. M. Fuleki. Understanding Ice Crystal Accretion and Shedding Phenomenon in Jet Engines Using a Rig Test. *J. Eng. Gas Turb. Power*, 133(4):041201, 2011.

S. W. McCue, J. R. King, and D. S. Riley. The extinction problem for three-dimensional inward solidification. *J. Eng. Math.*, 52(4):389–409, 2005.

S. W. McCue, B. Wu, and J. M. Hill. Classical two-phase Stefan problem for spheres. *Proc. R. Soc. A*, 464(2096):2055–2076, 2008.

D. McKenzie. The Generation and Compaction of Partially Molten Rock. *J. Petrol.*, 25(3):713–765, 1984.

J. C. Melrose. Model calculations for capillary condensation. *AIChE J.*, 12(5):986–994, 1966.

B. Messinger. Equilibrium Temperature of an Unheated Icing Surface as a Function of Air Speed. *J. Aeronaut. Sci.*, 20(1), 1953.

D. Miller, T. Bond, D. Sheldon, W. Wright, T. Langhals, K. Al-Khalil, and H. Broughton. Validation of NASA Thermal Ice Protection Computer Codes. Part 1–Program Overview. In *35th Aerospace Sciences Meeting & Exhibit, American Institute of Aeronautics and Astronautics, Reston, VA*, number AIAA 97-0049, 1997.

I. Mirzaii and M. Passandideh-Fard. Modeling free surface flows in presence of an arbitrary moving object. *Int. J. Multiphas. Flow*, 39: 216–226, 2012.

S. K. Mitra, O. Vohl, M. Ahr, and H. R. Pruppacher. A wind tunnel and theoretical study of the melting behavior of atmospheric ice particles. IV: Experiment and theory for snow flakes. *J. Atmos. Sci.*, 47(5): 584–591, 1990.

E. Molz, A. P. Y. Wong, M. H. W. Chan, and J. R. Beamish. Freezing and melting of fluids in porous glasses. *Phys. Rev. B*, 48(9):5741, 1993.

N. R. Morgenstern and J. F. Nixon. One-dimensional Consolidation of Thawing Soils. *Can. Geotech. J.*, 8(4):558–565, 1971.

M. Muto, M. Tsubokura, and N. Oshima. Negative Magnus lift on a rotating sphere at around the critical Reynolds number. *Phys. Fluids*, 24(014102), 2012.

T. G. Myers. Extension to the Messinger model for aircraft icing. *AIAA J.*, 39(2):211–218, 2001.

T. G. Myers and J. P. F. Charpin. A mathematical model for atmospheric ice accretion and water flow on a cold surface. *Int. J. Heat Mass Tran.*, 47(25):5483–5500, 2004.

T. G. Myers, J. P. F. Charpin, and S. J. Chapman. The flow and solidification of a thin fluid film on an arbitrary three-dimensional surface. *Phys. Fluids*, 14(8):2788–2803, 2002a.

T. G. Myers, J. P. F. Charpin, and C. P. Thompson. Slowly accreting ice due to supercooled water impacting on a cold surface. *Phys. Fluids*, 14 (1):240–256, 2002b.

T. Nomura, N. Okinaka, and T. Akiyama. Impregnation of porous material with phase change material for thermal energy storage. *Mater. Chem. Phys.*, 115(2):846–850, 2009.

J. S. Olafsen and J. S. Urbach. Two-dimensional melting far from equilibrium in a granular monolayer. *Phys. Rev. Lett.*, 95(9):098002, 2005.

M. J. Oliver. *A STUDY ON THE PHYSICS OF ICE ACCRETION IN A TURBOFAN ENGINE ENVIRONMENT*. PhD thesis, Case Western Reserve University, 2013.

M. J. Oliver. Validation Ice Crystal Icing Engine Test in the Propulsion Systems Laboratory at NASA Glenn Research Center. In *6th AIAA Atmospheric and Space Environments Conference*, number AIAA 2014-2898, 2014.

R. G. Oraltay and J. Hallett. Evaporation and melting of ice crystals: A laboratory study. *Atmos. Res.*, 24(1):169–189, 1989.

F. M. Orr, L. E. Scriven, and A. P. Rivas. Pendular rings between solids: meniscus properties and capillary force. *J. Fluid Mech.*, 67(04):723–742, 1975.

S. Osher and R. Fedkiw. *Level set methods and dynamic implicit surfaces*, volume 153. Springer Science & Business Media, 2006.

F. Pacheco-Vázquez, G. A. Caballero-Robledo, and J. C. Ruiz-Suárez. Superheating in granular matter. *Phys. Rev. Lett.*, 102(17):170601, 2009.

O. Parent and A. Ilinca. Anti-icing and de-icing techniques for wind turbines: Critical review. *Cold Reg. Sci. Technol.*, 65(1):88–96, 2011.

P. Pawlow. The dependency of the melting point on the surface energy of a solid body. *Z. Phys. Chem.*, 65:545–548, 1909.

L. Pawlowski. *The Science and Engineering of Thermal Spray Coatings.* John Wiley & Sons, Chichester, 2008.

R. I. Pedroso and G. A. Domoto. Perturbation solutions for spherical solidification of saturated liquids. *J. Heat Tran.*, 95(1):42–46, 1973.

P. O. Persson and G. Löndahl. *Freezing technology in C. P. Mallett (Ed.), Frozen Food Technology*, chapter Freezing technology, pages 20–58. Springer Science & Business Media, 1993.

J. V. Poncelet. *Cours de Mécanique Industrielle.* 1829.

D. J. Priour Jr. Percolation through voids around overlapping spheres: A dynamically based finite-size scaling analysis. *Phys. Rev. E*, 89(1): 012148, 2014.

X. Py, R. Olives, and S. Mauran. Paraffin/porous-graphite-matrix composite as a high and constant power thermal storage material. *Int. J. Heat Mass Tran.*, 44(14):2727–2737, 2001.

R. Rasmussen and H. R. Pruppacher. A wind tunnel and theoretical study of the melting behavior of atmospheric ice particles. I: A wind tunnel study of frozen drops of radius$<$ 500 µm. *J. Atmos. Sci.*, 39(1):152–158, 1982.

R. M. Rasmussen, V. Levizzani, and H. R. Pruppacher. A Wind Tunnel and Theoretical Study of the Melting Behavior of Atmospheric Ice Particles. II: A Theoretical Study for Frozen Drops of Radius< 500 μm. *J. Atmos. Sci.*, 41(3):374–380, 1984a.

R. M. Rasmussen, V. Levizzani, and H. R. Pruppacher. A wind tunnel and theoretical study on the melting behavior of atmospheric ice particles: III. Experiment and theory for spherical ice particles of radius> 500 μm. *J. Atmos. Sci.*, 41(3):381–388, 1984b.

A. Richter and P. A. Nikrityuk. New correlations for heat and fluid flow past ellipsoidal and cubic particles at different angles of attack. *Powder Technol.*, 249:463–474, 2013.

D. S. Riley, F. T. Smith, and G. Poots. The inward solidification of spheres and circular cylinders. *Int. J. Heat Mass Tran.*, 17(12):1507–1516, 1974.

M. D. Rintoul and S. Torquato. Precise determination of the critical threshold and exponents in a three-dimensional continuum percolation model. *J. Phys. A-Math. Gen.*, 30(16):L585, 1997.

M. A. Ríos Pabón. *Ice crystal ingestion by turbofans.* PhD thesis, Drexel University, 2012.

I. V. Roisman and C. Tropea. Impact of a drop onto a wetted wall: description of crown formation and propagation. *J. Fluid Mech.*, 472: 373–397, 2002.

I. V. Roisman, L. Opfer, C. Tropea, M. Raessi, J. Mostaghimi, and S. Chandra. Drop impact onto a dry surface: role of the dynamic contact angle. *Colloid. Surface. A*, 322(1):183–191, 2008.

G. A. Ruff and B. M. Berkowitz. Users manual for the NASA Lewis ice accretion prediction code (LEWICE). Technical Report NASA CR-185129.

G. Ryskin and L. G. Leal. Numerical solution of free-boundary problems in fluid mechanics. Part 1. The finite-difference technique. *J. Fluid Mech.*, 148:1–17, 1984.

M. Schäfer. *Numerik im Maschinenbau.* Springer-Verlag, 2013.

C. M. Seddon and M. Moatamedi. Review of water entry with application to aerospace structures. *Int. J. Impact Eng.*, 32:1045–1067, 2006.

C. Selcuk, S. Bond, and P. Woollin. Joining processes for powder metallurgy parts: a review. *Powder Metall.*, 53(1):7–11, 2010.

J. A. Sethian. *Level Set Methods and Fast Marching Methods*. Cambridge University Press, Cambridge, 1999.

M. Shiffman and D. C. Spencer. The force of impact on a sphere striking a water surface (approximation by the flow about a lens). *AMP Report 42.1R AMG-NYU no.15, Applied Mathematics Panel*, 1945.

A. M. Soward. A unified approach to Stefan's problem for spheres and cylinders. *Proc. R. Soc. A*, 373(1752):131–147, 1980.

P. R. Spalart and S. R. Allmaras. A one-equation turbulence model for aerodynamic flows. *Rech. Aerospatiale*, 1:5–21, 1992.

K. Stewartson and R. T. Waechter. On Stefan's problem for spheres. *Proc. R. Soc. A*, 348(1655):415–426, 1976.

P. Struk, T.C. Currie, W.B. Wright, D.C. Knezevici, D. Fuleki, A. Broeren, M. Vargas, and J.-C. Tsao. Fundamental Ice Crystal Accretion Physics Studies. Number 2011-38-0018. SAE Technical Paper, 2011.

P. Struk, T. Bartkus, J.-C. Tsao, T. C. Currie, and D. Fuleki. Ice Accretion Measurements on an Airfoil and Wedge in Mixed-Phase Conditions. Number 2015-01-2116. SAE Technical Paper, 2015.

S. Tabakova, F. Feuillebois, and S. Radev. Freezing of a supercooled spherical droplet with mixed boundary conditions. *Proc. R. Soc. Lond. A*, 466(2116):1117–1134, 2010.

K.-H. Tacke. Discretization of the expliclt enthalpy method for planar phase change. *Int. J. Numer. Meth. Eng.*, 21(3):543–554, 1985.

G. I. Taylor. The dynamics of thin sheets of fluid. II. Waves on fluid sheets. *Proc. R. Soc. Lond. A*, 263:296–312, 1959.

A. H. Techet and T. T. Truscott. Water entry of spinning hydrophobic and hydrophilic spheres. *J. Fluid. Struct.*, 27:716–726, 2011.

S. K. Thomas, R. P. Cassoni, and C. D. MacArthur. Aircraft anti-icing and de-icing techniques and modeling. *J. Aircraft*, 33(5):841–854, 1996.

S. T. Thoroddsen. The ejecta sheet generated by the impact of a drop. *J. Fluid Mech.*, 451:373–381, 2002.

A.-K. Tornberg and B. Engquist. A finite element based level-set method for multiphase flow applications. *Comput. Vis. Sci.*, 3(1-2):93–101, 2000.

J. P. Trelles and J. J. Dufly. Numerical simulation of porous latent heat thermal energy storage for thermoelectric cooling. *Appl. Therm. Eng.*, 23(13):1647–1664, 2003.

T. T. Truscott and A. H. Techet. A spin on cavity formation during water entry of hydrophobic and hydrophilic spheres. *Phys. Fluids*, 21 (121703), 2009a.

T. T. Truscott and A. H. Techet. Water entry of spinning spheres. *J. Fluid Mech.*, 625:135–165, 2009b.

T. T. Truscott, B. P. Epps, and A. H. Techet. Unsteady forces on spheres during free-surface water entry. *J. Fluid Mech.*, 704:173–210, 2012.

T. T. Truscott, B. P. Epps, and J. Belden. Water entry of projectiles. *Annu. Rev. Fluid Mech.*, 46:355–378, 2014.

C. C. Tseng and R. Viskanta. Heating/melting of a fused silica particle by convection and radiation. *Int. J. Heat. Mass Tran.*, 49(17):2995–3003, 2006.

Y. Tsuji, Y. Morikawa, and O. Mizuno. Experimental measurement of the Magnus force on a rotating sphere at low Reynolds numbers. *J. Fluid. Eng.*, 107:484–488, 1985.

B. Turnbull. Scaling laws for melting ice avalanches. *Phys. Rev. Lett.*, 107 (25):258001, 2011.

VDI-Gesellschaft Verfahrenstechnik und Chemieingenierwesen (GVC), editor. *VDI-Wärmeatlas: Berechnungsblätter für den Wärmeübergang (German Edition)*. Springer Vieweg, 10th edition, 2005.

D. Vella and P. D. Metcalfe. Surface tension dominated impact. *Phys. Fluids*, 19(072108), 2007.

D. Vella, D.-G. Lee, and H.-Y. Kim. Sinking of a Horizontal Cylinder. *Langmuir*, 22:2972–2974, 2006.

P. Villedieu, P. Trontin, and R. Chauvin. Glaciated and mixed-phase ice accretion modeling using ONERA 2D icing suite. In *6th AIAA Atmospheric and Space Environments Conference, AIAA, Atlanta, USA*, number AIAA 2014-2199.

V. R. Voller. Implicit finite-difference solutions of the enthalpy formulation of Stefan problems. *IMA J. Numer. Anal.*, 5(2):201–214, 1985.

V. R. Voller, C. R. Swaminathan, and B. G. Thomas. Fixed grid techniques for phase change problems: a review. *Int. J. Numer. Meth. Eng.*, 30(4):875–898, 1990.

T. von Kármán. The impact on seaplane floats during landing. Technical Report 321, NACA Technical Notes.

W. Wagner, A. Saul, and A. Pruss. International equations for the pressure along the melting and along the sublimation curve of ordinary water substance. *J. Phys. Chem. Ref. Data*, 23(3):515–527, 1994.

C. W. Walker, S. T. McClain, and T. A. Shannon. Convection from Ice Roughness with Varying Flux Boundary Conditions. In *6th AIAA Atmospheric and Space Environments Conference, AIAA, Atlanta, USA*, number AIAA 2014-2463, 2014.

A. Wang, Q. Song, and Q. Yao. Behavior of hydrophobic micron particles impacting on droplet surface. *Atmos. Environ.*, 115:1–8, 2015a.

J. Wang, M. Yang, and Y. Zhang. A multiscale nonequilibrium model for melting of metal powder bed subjected to constant heat flux. *Int. J. Heat. Mass Tran.*, 80:309–318, 2015b.

Y. Q. Wang, W. S. Liang, and C. Y. Geng. Shape evolution of gold nanoparticles. *J. Nanopart. Res.*, 12(2):655–661, 2010.

H. Watanabe, S. Yukawa, and N. Ito. Size-dispersity effects in two-dimensional melting. *Phys. Rev. E*, 71(1):016702, 2005.

K. M. Watts, I. J. Campbell, and A. Lips. The Stability of Aerated Milk Protein Emulsions in the Presence of Small Molecule Surfactants. *J. Dairy Sci.*, 80(10):2631–2638, 1997.

H. G. Weller. A new approach to VOF-based interface capturing methods for incompressible and compressible flow. *OpenCFD Ltd., Report TR/HGW/04*, 2008.

G. B. Whitham. *Linear and nonlinear waves.* John Wiley & Sons, New York, 1999.

J. M. Williams, A. Adewunmi, R. M. Schek, C. L. Flanagan, P. H. Krebsbach, S. E. Feinberg, S. J. Hollister, and S. Das. Bone tissue engineering using polycaprolactone scaffolds fabricated via selective laser sintering. *Biomaterials*, 26(23):4817–4827, 2005.

A. M. Worthington. *A Study of Splashes.* Longmans Green and Co., Plymouth. Printed by William Brendon and Son, Ltd.; reprinted in 2012 by HardPress Publishing, 1908. ISBN 9781290265812.

W. B. Wright, P. C. E. Jorgenson, and J. P. Veres. Mixed phase modeling in GlennICE with application to engine icing. In *AIAA Atmospheric and Space Environments Conference, American Institute of Aeronautics and Astronautics, Reston, VA*, number AIAA-2010-7674, 2010.

W. B. Wright, P. Struk, T. Bartkus, and G. Addy. Recent Advances in the LEWICE Icing Model. Number 2015-01-2094. SAE Technical Paper, 2015.

W.-M. Yan, H.-Y. Li, Y.-J. Wu, J.-Y. Lin, and W.-R. Chang. Performance of finned tube heat exchangers operating under frosting conditions. *Int. J. Heat Mass Tran.*, 46(5):871–877, 2003.

Y. Yao, Y. Jiang, S. Deng, and Z. Ma. A study on the performance of the airside heat exchanger under frosting in an air source heat pump water heater/chiller unit. *Int. J. Heat Mass Tran.*, 47(17):3745–3756, 2004.

A. L. Yarin and D. A. Weiss. Impact of drops on solid surfaces: self-similar capillary waves, and splashing as a new type of kinematic discontinuity. *J. Fluid Mech.*, 283:141–173, 1995.

A. L. Yarin, G. Brenn, J. Keller, M. Pfaffenlehner, E. Ryssel, and C. Tropea. Flowfield characteristics of an aerodynamic acoustic levitator. *Phys. Fluids*, 9(11):3300–3314, 1997.

A. L. Yarin, M. Pfaffenlehner, and C. Tropea. On the acoustic levitation of droplets. *J. Fluid Mech.*, 356:65–91, 1998.

C. L. Yaws. *Thermophysical properties of chemicals and hydrocarbons*. William Andrew, 2008.

W. P. Zakrzewski. Splashing a ship with collision-generated spray. *Cold Reg. Sci. Technol.*, 14(1):65–83, 1987.

M.-Y. Zhou and P. Sheng. Lattice softening and melting characteristics of granular particles. *Phys. Rev. B*, 43(4):3460, 1991.

List of Figures

List of Tables